

國立臺灣大學理學院海洋研究所

博士論文

Institute of Oceanography

College of Science

National Taiwan University

Doctoral Dissertation



次表層溫度異常在熱帶太平洋年代際變率中的作用

The Role of Subsurface Temperature Anomalies in
Tropical Pacific Decadal Variability

陳紹強

Sieu-Cuong San

指導教授：曾于恒博士

Advisor: Yu-heng Tseng, Ph.D.

中華民國 113 年 1 月

January 2024

Acknowledgments


First and foremost, I would like to express my sincere appreciation to my supervisor, Prof. Yu-Heng Tseng, for his patient guidance throughout my PhD journey. I am extremely grateful for his willingness to engage in constructive discussions, share his knowledge, and provide valuable insights. Without Prof. Tseng's support and mentorship, this research could not have been accomplished.

I would like to express my gratitude to Prof. Chung-Hsiung Sui for his valuable comments and suggestions during the Independent Study. Prof. Sui's insights and advice have been immensely helpful in shaping my research related to Tropical Pacific Decadal Variability. Moreover, I am grateful to my former master's supervisor Prof. Chia-Cheng Tsai, and Prof. Kuo-Tung Chang for taking me to the world of fluid mechanics without which I would not have been able to obtain a PhD degree in Physical Oceanography.

I am also grateful to my PhD committee members: Prof. Chung-Hsiung Sui, Prof. Sen Jan, Dr. Huang-Hsiung Hsu, Prof. Yen-Ting Hwang, and Prof. Yu-Heng Tseng. Without their encouragement and scientific comments, I could not have completed my PhD thesis.

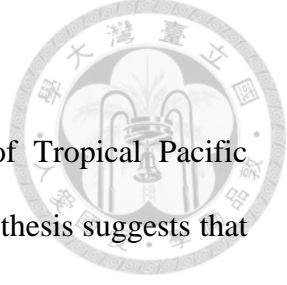
Finally, I would like to express my deepest appreciation to my family for their unwavering patience and encouragement during my stay in Taiwan. Their love and support have been my constant source of strength, and I cannot thank them enough. I hope to make them proud of my achievements.

摘要

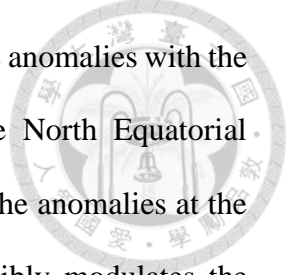


有關引起熱帶太平洋年代際變化機制及相位轉換的過程，至今仍存在爭議。其中有一種觀點認為，中緯度大氣強迫海洋次表層後的溫度異常及其後續傳至赤道的現象可能是主導機制之一。我們首先使用觀測和再分析數據，證明了北太平洋海洋-大氣耦合所引起的年代際次表層鮮度異常確實能夠傳至赤道太平洋區域。具體而言，由大氣阿留申低壓驅動的太平洋年代際振盪在中緯度和副熱帶東部太平洋次表層分別形成正、負異常的鮮度分佈。這些鮮度異常分佈透過平均加速勢定義的北太平洋路徑向赤道傳播，其中源自中緯度東太平洋的正異常七年後可到達 14°N ，而源自副熱帶東太平洋的負異常三年後可到達 10°N 。我們的結果證實，北太平洋藉由大氣橋驅動的熱帶-溫帶交互作用和海洋通道確實能夠產生潛在的年代際振盪。其次，我們使用觀測、再分析數據和模式敏感度實驗，確認赤道外次表層溫度異常對熱帶太平洋年代際變化的相位轉換起著關鍵作用。在熱帶太平洋年代際變化的正位相期間，赤道變暖導致了赤道西北太平洋的異常大氣響應，導致次表層存在負異常的海溫。這些溫度異常從西北太平洋開始，沿著北赤道反流路徑向赤道中太平洋方向移動，約三年後開始反轉赤道海溫的相位。同時，在熱帶太平洋年代際變化正位相時，也能透過熱帶-溫帶交互作用調節數年後黑潮延伸流的變化，藉由北太平洋經向模態的海氣交互作用，強化赤道次表層海溫的反應。最終，五年後完全轉為冷相位。這個過程能夠完整解釋赤道太平洋年代際振盪的機制和相位轉換的過程。

Abstract



The mechanisms and processes underlying the phase transition of Tropical Pacific Decadal Variability (TPDV) remain incompletely understood. One hypothesis suggests that the equatorward propagation of remotely generated subsurface temperature anomalies and their subsequent equatorial emergence may play a dominant role. In the first part of the thesis, we utilize observation and reanalysis data to demonstrate the existence of a decadal subsurface spiciness (density-compensated temperature and salinity anomalies) mode that is intrinsic to the ocean-atmosphere coupling in the North Pacific. Specifically, the strengthening of the Aleutian Low, which is the dominant atmospheric forcing of the Pacific Decadal Oscillation, drives a dipole pattern of positive and negative spiciness anomalies in the eastern midlatitude and subtropics, respectively. These anomalies then propagate equatorward along the North Pacific pathway defined by the mean acceleration potential. The positive anomaly of midlatitude origin can reach 14°N after seven years of propagation while the negative anomaly of subtropical origin can arrive at 10°N after three years. In addition, a negative anomaly emerges in the midlatitude after the occurrence of the positive signal two years later, then follows the pathway that the positive takes to reach the tropics. Furthermore, we find that equatorial sea surface temperature variability can also contribute to the generation of the subsurface spiciness mode. Our results thus suggest a potential decadal oscillation in the North Pacific involving extratropical-tropical interaction via oceanic tunnel and atmospheric bridge. In the second part of the thesis, we use observation, reanalysis data, and model experiments to identify the key role of off-equatorial subsurface temperature anomalies in the phase reversal of TPDV. During the positive phase of TPDV, equatorial warming induces anomalous atmospheric responses in the off-equatorial western Pacific,



leading to negative subsurface temperature anomalies. These temperature anomalies with the center of action residing in the northwestern region then follow the North Equatorial Countercurrent pathway toward the central basin to reverse the sign of the anomalies at the equator around three years later. The TPDV positive phase also possibly modulates the change of the Kuroshio Extension state a few years later through the tropical-extratropical interaction, which subsequently projects on the footprinting of Pacific Meridional Mode to strengthen the abovementioned negative subsurface disturbance 0-12 months before the peak cold phase. Eventually, the cold phase is completely established after five years. The same dynamic is also held with an opposite sign for the reversed phase, leading to a preferred decadal oscillation via off-equatorial subsurface temperature anomalies and extratropical-tropical ocean-atmosphere interaction.

Keywords: Aleutian Low, Pacific Decadal Oscillation, subsurface spiciness propagating mode, Tropical Pacific Decadal Variability, extratropical-tropical interaction

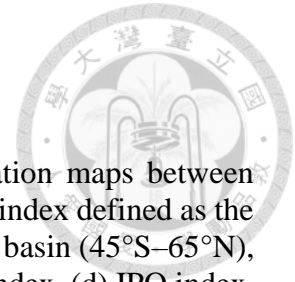


Contents

Acknowledgments	i
摘要.....	ii
Abstract	iii
List of Figures	vii
Chapter 1 Introduction	1
1.1 Pacific interannual to decadal climate variability.....	1
1.2 Tropical Pacific Decadal Variability (TPDV).....	5
1.3 Potential mechanisms of TPDV.....	9
1.4 Thesis objectives and structures.....	18
Chapter 2 Aleutian Low/PDO forces a decadal subsurface spiciness propagating mode in the North Pacific	21
Preface.....	21
2.1 Introduction.....	22
2.2 Data and methodology.....	28
2.3 Results.....	31
2.3.1 Characteristics of low-frequency spiciness variability.....	31
2.3.2 Forcing mechanism.....	37
2.3.3 Formation of isopycnal spiciness anomalies.....	42
2.4 Discussion.....	51
2.5 Conclusions.....	55
2.6 Supporting information.....	57
Chapter 3 The role of off-equatorial subsurface temperature anomalies in the phase reversal of Tropical Pacific Decadal Variability	64
Preface.....	64
3.1 Introduction.....	65
3.2 Data and methodology.....	68
3.3 Results.....	72
3.3.1 Observed Pacific decadal climate variability.....	72
3.3.2 Origin and preferred time scale of TPDV.....	80
3.3.3 Overall TPDV framework.....	86
3.4 Summary and discussion.....	88
3.5 Supporting information.....	89

Chapter 4 Discussion and conclusions	97
4.1 Summary	97
4.2 Discussion	97
4.3 Future work	98
References	100





List of Figures

- Figure 1.1 Patterns of Pacific low-frequency SST variability. Correlation maps between monthly NOAA ERSST.v3 SSTA and (a) Pacific Decadal Variability index defined as the first principal component (PC1) of 8-year low-pass SSTA over Pacific basin (45°S – 65°N), (b) 8-year low-pass PDO index, (c) 8-year low-pass negative NPGO index, (d) IPO index, and (e) 8-year low-pass SPDO index. Black contours are regression coefficients ($^{\circ}\text{C}$). The time series of the indices are shown in (f) and compared against a TPDV index defined as PC1 of 8 year low-pass SST over the equatorial Pacific (12°S – 12°N). (source: Liu and Di Lorenzo 2018). 3
- Figure 1.2 Dynamical modes of Pacific SSTA, derived from the ensemble average eigenmodes of the dynamical operator of linear inverse models. (a) warming trend, (b) KOE mode, (c) NP-CP mode, (d) eastern Pacific-ENSO mode, (e) central Pacific-ENSO mode and (f) ENSO decay mode. (g) The respective normalized time series (real) derived from HadISST. The units are nondimensional (-1, 1) and each pattern was normalized using the standard deviation of their correspondent real-part time series prior to taking the ensemble average. (source: Di Lorenzo et al. 2023) 5
- Figure 1.3 Observed basinwide changes associated with TPDV transitions. Differences of (a, d) SST, (b, e) sea level pressure (SLP) and 10-m wind, and (c, f) SSH between (top) 2013-2018 and 2007-2012 and (bottom) 2007-2012 and 2002-2007. The trend is linearly removed and anomalies are calculated by removing monthly averages over 1980-2020. SST data are from HadISST (Rayner et al., 2003), SSH is from GODAS (Behringer and Xue, 2004), SLP and winds are from NCEP-NCAR reanalysis (Kalnay et al., 1996). 6
- Figure 1.4 Same as Figure 1.3 but for temperature anomalies averaged over the (left) western (120°E - 180°) and (right) eastern (180° - 60°W) Pacific. Contours indicate climatological values of potential density. Temperature data are from EN.4.2.2 (Good et al., 2013). 7
- Figure 1.5 Latitude-time plot of SSH anomalies averaged (a) west and (b) east of the dateline. (c) Latitude-time plot of SSTA averaged over 5°S - 5°N . (d) TPDV index defined as 8-20 year bandpass filtered SSTA over 5°S - 5°N , 160°E - 150°W . In a-c, SSTA and SSH anomalies are obtained by removing the linear trend and the climatological monthly mean over 1950-2020. The horizontal solid (dashed) green lines indicate strong and very strong El Niño (La Niña) events that peak in December based on the Oceanic Niño Index (ONI). SST data are from HadISST (Rayner et al., 2003) and SSH is from GECCO3 (Köhl, 2020). 10
- Figure 1.6 The advection of spiciness anomalies (pink shading) by the mean circulation (black arrows) on the 25.0 kg m^{-3} isopycnal surface. Shading indicates isopycnal depth, and the dashed blue line indicates the ‘potential vorticity barrier’ in the 5° – 10°N latitude band. The lower panel depicts zonally averaged isopycnal depths (from 23 to 25.5 kg m^{-3} with a spacing of 0.5 kg m^{-3} ; solid lines: 23, 24 and 25 kg m^{-3} ; dashed lines: 23.5, 24.5 and 25.5 kg m^{-3}), and the flow of equatorward spiciness anomalies along isopycnal surfaces. (source: Capotondi et al. 2023) 11

Figure 1.7 Same as Figure 1.6, but for the $v'\bar{T}$ mechanism. The mean (anomalous) flows are denoted by black (red) arrows. (source: Capotondi et al. 2023). 13

Figure 1.8 A wave teleconnection from the midlatitude Pacific to the equator. Midlatitude planetary Rossby waves travel westward at all latitudes and are damped. The waves that are amplified in baroclinically unstable regions of the subtropical gyre arrive to the equator with a larger amplitude and therefore dominate the midlatitude signal there. (source: Galanti and Tziperman 2003)..... 14

Figure 1.9 Proposed framework for TPDV. (source: Joh and Di Lorenzo 2019) 16

Figure 1.10 Decadal interbasin connections with the Pacific. (a) Indian Ocean warming induces a Gill-type response that increases surface easterlies and cold SSTA in the western Pacific. (b) Atlantic Ocean warming creates a Gill-type response resulting in anomalous easterlies and cold SSTA over the western and western-central Pacific, respectively. (c) Sliding-window 20-year trends of interbasin SST differences (ERSST) and equatorial western Pacific wind stress. The wind stress and its 1-standard deviation spread (shading) are from a 56-member reanalysis of the 20th-century climate. Wind stress from Extended Reanalysis-Interim for the post-1979 period is also used. Pre- and post-1980 correlations between the transbasin SST (ERSST) and the ensemble-mean equatorial zonal wind trends are provided, along with the 1-standard deviation spread of correlations from the 56 realizations. Indian (IND), Pacific (PAC), and Atlantic (ATL) basin SST are calculated over 20°S-20°N and 21°E-120°E, 20°S-20°N and 121°E-90°W, and 20°S-20°N and 70°W-20°E, respectively. The Pacific wind is computed over 6°S-6°N, 180°E-210°E. (d) The atmospheric circulation and surface temperature changes generated owing to Atlantic warming in (b) are amplified by the Pacific Bjerknes feedback and IOD-Pacific interactions. The depth-longitude section in (d) illustrates the subsurface temperature and circulation anomalies in the Indo-Pacific. In (a), (b), and (d), the color shading indicates temperature, with red being warmest and blue being coolest. (source: Cai et al. 2019)... 18

Figure 1.11 Processes and mechanisms associated with TPDV. The warm phase of TPDV, characterized by the strongest equatorial positive SSTA (shading, upper), induces convective heating anomalies and cyclonic circulations in the extratropical North (blue circle) and South Pacific. The green arrows signify wave propagation mechanisms, including westward-propagating Rossby waves, followed by equatorward movement along the boundary as coastal Kelvin waves and along the equator as equatorial Kelvin waves. The contribution from the Indian and Atlantic Oceans is also represented by olive green arrows. On the right, subsurface processes proposed to explain the TPDV phase transition involve the propagation of spiciness anomalies (gray shading) by mean STC (pink arrows), along with variability in the strength of the STC (blue arrows). The decadal framework proposed by Joh and Di Lorenzo (2019) is depicted, indicating the Aleutian Low/NPO (blue circle) inducing westward-propagating Rossby waves (blue arrow) to change KE state, leading to storm track change to excite downstream atmospheric response (purple circle), contributing to the forcing of the PMM (white arrows) which in turn drives to TPDV. 19

Figure 2.1 Standard deviation of low-frequency spiciness variability averaged between 25-26 σ_{θ} in the North Pacific associated with CEOF1. The variance explained by CEOF1 is shown in (a) for EN422 and (b) for MOAA GPV, respectively. The spatial phase of the leading mode derived from (c) EN422 and (d) MOAA GPV. The thick black lines denote the mean acceleration potential contours of 19.7- and 21.0 m^2s^{-2} (NPP). The gray line in (a) indicates the latitude of 10°N. 31

Figure 2.2 Latitude-time diagram of reconstructed spiciness anomalies using the (a) first and (b) all CEOF modes averaged along the NPP based on EN422. The vertical solid (dashed) gray lines represent strong and very strong (moderate) El Nino events that peak in January based on the Oceanic Niño Index (ONI). 33

Figure 2.3 Normalized time series of (a) real and (b) imaginary expansion coefficients of CEOF1. The associated temporal phase (in degree) of the CEOF1 is shown as green dots. The black and red lines are the PDO index from the NOAA Physical Sciences Laboratory and Niño3 (5°S-5°N, 150°-90°W) index obtained from the NOAA Climate Prediction Center, respectively. The blue number in (a) is the simultaneous correlation between PC1 (real) of spiciness anomalies derived from MOAA GPV and EN422 during the same period (2002-2018) and similarly, the number in (b) is the correlation obtained from the first imaginary part of the two datasets. The second red number in (a) is the simultaneous correlation between the PDO and the Niño3. POS and NEG correspond to PDO positive and negative phases. 35

Figure 2.4 (a) Lead-lag correlation coefficients between the PC1 of spiciness anomalies and the PDO index. Horizontal dashed lines indicate the 95% confidence level. (b) Lead-lag correlation coefficients between the PDO index and reconstructed spiciness anomalies using CEOF1 averaged along the NPP. Shading indicates correlation coefficients that are significant at the 95% confidence level (Student's t-test). The thick black line in (b) indicates lag 0. Positive lags indicate PDO leads the spiciness anomalies. 36

Figure 2.5 (a) Reconstructed spiciness anomalies using CEOF1 regressed with the PDO index at lag 22 months (shading and green contours, only regressed values significant at the 95% confidence level according to a Student's t-test are shown). The contour interval is 0.025 kg m^{-3} and the solid (dashed) contours denote positive (negative) anomalies. (b) Spatial structure of the corresponding CEOF1 (real). The thick black lines represent the defined NPP. 38

Figure 2.6 Reconstructed spiciness anomalies using CEOF1 regressed with the PDO index from lag 0 to lag 84 months (shading and green contours, only regressed values significant at the 95% confidence level according to a Student's t-test are shown). The contour interval is 0.025 kg m^{-3} and the solid (dashed) contours denote positive (negative) anomalies. The red and blue boxes represent the midlatitude (40-50°N, 145-130°W) and subtropical (20-28°N, 140-125°W) regions, respectively. The thick black lines show the NPP. Positive lags indicate PDO leads the spiciness anomalies. 39

Figure 2.7 Bias-rectified wavelet power spectra and corresponding global wavelet spectra of (a) PDO, (b) PC1 (real), (c) Niño3, and (d) Niño4 (5°S-5°N, 160°E-150°W). Thin black

contours indicate statistically significant at the 95% confidence level when tested against a first-order autoregressive model null hypothesis. The parabola regions indicate the “cone of influence” where edge effects become important. The horizontal dashed green lines indicate the 8- and 16-year periods. All the data are analyzed from 1980 to 2018..... 41

Figure 2.8 (a) SLP (shading and gray contours) and (b) Qnet (shading) anomalies 22 months ahead regressed with the PC1 of spiciness anomalies. Wind vectors at 10 m regressed with the PC1 are also imposed. Regressed values significant at the 95% confidence level (Student’s t-test) are shaded for SLP and Qnet anomalies. Only regressed wind vectors significant at the 95% confidence level are shown. The red and blue boxes are described in Figure 2.6. The thick black lines represent the NPP. 43

Figure 2.9 Time-depth plot of (a) conservative temperature and (b) absolute salinity anomalies averaged in 40-50°N, 145-130°W (the red box in Figure 2.6). (c) Time- σ_θ plot of spiciness anomalies averaged over the same region and period as (a) and (b). The horizontal dashed back lines in (a) and (b) indicate the depth of 50- and 120 m. The thick black lines in (c) show the isopycnal depth of 50- and 120 m. Anomalies are calculated relative to the mean from 1980 to 2018. 45

Figure 2.10 (a) Annual mean outcrop position of $\sigma_\theta=25$ surface (thin black contours) and (b) standard deviation of spiciness anomalies averaged between 25-26 σ_θ in March. Superimposed in (a) is mean March sea surface density during 1980-2018 (shading). In all panels, the thick green and magenta contours denote the mean and extreme equatorward outcrop position of $\sigma_\theta=25$ in March, respectively. The red and blue boxes are the regions defined in Figure 2.6. 45

Figure 2.11 (a) Time series of the March outcrop latitude of $\sigma_\theta=25$ averaged from 145° to 130°W (black) and the areal mean (the red box) of spiciness anomalies averaged between 25-26 σ_θ (green). The mean outcrop latitude of $\sigma_\theta=25$ is shown by the dashed black line. (b) Time series of the areal mean (35-60°N, 150-115°W) SSTA (red) and SSS anomalies (blue). Superimposed is March PDO index (black). The red number is the simultaneous correlation between SSTA and PDO..... 47

Figure 2.12 Monthly mean (top) SSTA and (bottom) SSS anomalies in (left) 2015 and (right) 2017 March. The thick black contours show the corresponding outcrop position of $\sigma_\theta=25$. The red and blue boxes are the regions defined in Figure 2.6. 48

Figure 2.13 Same as Figure 2.9 but in the region 20-28°N, 140-125°W (the blue box in Figure 2.6). The horizontal dashed back lines in (a) and (b) indicate the depth of 120- and 250 m. The thick black lines in (c) show the isopycnal depth of 120- and 250 m..... 49

Figure 2.14 Spiciness anomalies averaged between 25-26 σ_θ regressed with the areal mean (black box) sea surface height anomalies from lag 0 to lag 36 months (only regressed values significant at the 95% confidence level according to a Student’s t-test are shown). The red and blue boxes are the regions defined in Figure 2.6. Positive lags indicate sea surface height leads..... 50

Figure 2.15 Lead-lag correlation coefficients between Nino SST indices and the PC1 of spiciness anomalies (a) during 1980-2018, (b) before 2000 and (c) after 2000. Horizontal dashed lines show the 95% confidence level. Positive lags indicate the Nino SST indices lead the PC1.	54
Figure 2.16 Schematic of decadal spiciness mode in the North Pacific. The solid red (dark blue) oval indicates positive (negative) spiciness anomalies in the midlatitude (subtropics).	56
Figure S2.1 Mean depth of the 25-26 σ_θ from 1980 to 2018 (EN422). The contour interval is 20 m. The red and blue boxes are described in Figure 2.6.	58
Figure S2.2 Reconstruction of the first CEOF mode of spiciness anomalies showing one full cycle (-180° to 180°) every 45° phase intervals. The thick black lines represent the NPP. The CEOF analysis is based on EN422.	59
Figure S2.3 Pacific (a) SSTA and (b) SLP anomalies (shading and gray contours) regressed with the PDO index. Wind vectors at 10 m regressed with the PDO index are also imposed in (b). Only regressed values significant at the 95% confidence level (Student's t-test) are shown. (c) Time series of the Aleutian Low (black, the first principal component of the EOF analysis of interannual SLP anomalies between 20°-60°N, 120°E-80°W. The first EOF mode explains 41% of the total SLP variance and the second EOF mode accounts for 19%). The red curve is the PDO index. The simultaneous correlation between the Aleutian Low and PDO is 0.63.	59
Figure S2.4 Pacific SSTA (shading) and SLP anomalies (hPa, gray contours) regressed with the PC1 of spiciness anomalies (PC1 lags 22 months). Wind vectors at 10 m regressed with the PC1 are also imposed. Only regressed values significant at the 95% confidence level are shown. The thick black lines represent the NPP. The CEOF analysis is based on EN422.	60
Figure S2.5 Lead-lag correlation coefficients between the February-April SSTA and temperature anomalies at different depths and months in the (a) midlatitude (the red box) and (b) 30-38°N, 145-130°W. The contour interval is 0.1. EN422 from 1980 to 2020 is used for the analysis.	60
Figure S2.6 (a) Lead-lag correlation coefficients between interannual MLD and interannual Ekman velocity (blue), friction velocity (gray), freshwater flux anomaly (red) and Qnet anomaly (black). Horizontal dashed lines indicate the 95% confidence level. (b) Same as (a) but for PDO index. (c) Time series of Qnet (positive downward). (d) Time series of anomalous MLD (black, left) with positive (negative) values indicate deepening (shoaling) of the mixed layer. Time series of the areal mean (the blue box) of spiciness anomalies averaged between 25 σ_θ (blue, right) and 25-26 σ_θ (red, right). (e) Same as Figure 13c but for depth-time plot. The black line denotes the MLD. All the four variables contribute to MLD changes are averaged in 20-30°N, 160-110°W.	61
Figure S2.7 Same as Figure 2.14 but for wind stress curl anomalies.	61

Figure S2.8 Sea surface height anomalies regressed with the PDO index from lag 0 to lag 36 months (only regressed values significant at the 95% confidence level according to a student's t-test are shown). The red and blue boxes are the regions defined in Figure 2.6. The thick black lines represent the NPP. Positive lags indicate PDO leads 62

Figure S2.9 Same as Figure S2.8 but for Qnet anomalies (positive downward)..... 62

Figure S2.10 Same as Figure S2.8 but for wind stress curl anomalies..... 63

Figure S2.11 Reconstructed spiciness anomalies using CEOF1 regressed with the (a) Niño3 and (b) Niño4 SST indices at lag 22 and 28 months, respectively. Only regressed values significant at the 95% confidence level according to a Student's t-test are shown. The contour interval is 0.025 kg m^{-3} and the solid (dashed) contours denote positive (negative) anomalies. The thick black lines represent the NPP. The CEOF analysis is based on EN422. 63

Figure 3.1 (a) Standard deviation of 8-20-year bandpass filtered temperature anomalies (shading and thin black contours) averaged between 5°S - 5°N . The contour interval is 0.2°C and zero contours are omitted. Violet lines denote the mean climatological potential density with 0.5 kg m^{-3} contour intervals. The vertical dashed black lines denote the longitude of 160°E and 150°W . (b) Bias-rectified wavelet power spectrum (shading) and corresponding global wavelet power spectrum of raw detrended Niño4 SST index. Thin black contours in the wavelet power spectrum and dashed black lines in the global power spectrum indicate statistically significance at the 90% confidence level when tested against a red-noise AR(1) process with lag-1 of 0.91. The parabola regions indicate the "cone of influence" where edge effects become important. The horizontal dashed pink lines indicate the 8 and 16 year periods. (c) same as (b) but for Niño3 SST index. Wavelet coherence between Niño4 SST index and Niño4 subsurface temperature anomalies averaged between (d) 22 - $24.5 \sigma_{\theta}$ and (e) 24.5 - $26 \sigma_{\theta}$. The 95% significance level against red noise is shown as thick black contours. The vectors designate the relative phase relationship (pointing right indicates in phase, pointing left indicates out of phase and pointing vertically upward means the Niño4 SST index lags subsurface temperature by 90°). The horizontal dashed magenta lines are the same as (b)..... 73

Figure 3.2 (a) Temporal evolution of raw detrended Niño4 SST index (left axis, thin blue) and its 8-20-year bandpass filtered component (TPDV index, right axis, thick blue) and 8-year lowpass filtered component (right axis, green). The reconstructed Niño4 SST index using the MTM-SVD method on a decadal timescale (period ~ 10.3 year) is shown in magenta (right axis). (b) Temporal evolution of raw detrended Niño4 subsurface temperature anomalies averaged between 22 - $24.5 \sigma_{\theta}$ (left axis, thin red) and its reconstruction using MTM-SVD on a decadal timescale (right axis, thick red). Similarly, the reconstruction of Niño4 subsurface temperature anomalies averaged between 24.5 - $26 \sigma_{\theta}$ is shown in black (right axis). The blue line is the same as (a). (c) Temporal evolution of raw detrended subsurface temperature anomalies averaged between 22 - $24.5 \sigma_{\theta}$ in 6° - 11°N , 140° - 160°E (NW box in Figure 3.4) (left axis, thin green) and its 8-20-year bandpass filtered component (right axis, thick green). Lead-lag correlation coefficients between TPDV index and (d) 8-20-year bandpass filtered temperature anomalies averaged between

22-24.5 σ_θ in (green) NW box, (blue) 6°-11°S, 150°-170°E (SW box) and (red) 5°S-5°N, 150°-160°E (W box), (e) reconstructed Niño4 subsurface temperature anomalies averaged between (red) 22-24.5 σ_θ and (black) 24.5-26 σ_θ using the MTM-SVD, (f) 8-20-year bandpass filtered Kuroshio Extension (KE) index defined as area-averaged SSH anomalies in 31°S-36°N, 140°-165°E and (g) 8-20-year bandpass filtered PMM SST (black) and wind (gray) index. Horizontal dashed lines in (d-g) show the 95% confidence level based on the non-parameter random-phase test. 75

Figure 3.3 Phase evolution of Pacific SST (shading), SLP (contours, hPa), and 10-m wind vector anomalies on decadal timescales (period ~10.3 years in the MTM-SVD analysis). The contour interval is 0.1 hPa (positive/negative is solid/dashed). Each panel corresponds roughly to six months. 76

Figure 3.4 Same as Figure 3.3 but for subsurface temperature anomalies averaged between 22-24.5 σ_θ . For clarity, positive (negative) temperature anomalies greater (smaller) than 0.3(-0.3) °C have been colored in red (blue). Vectors denote the mean current on 23.5 σ_θ derived from GODAS during 1980-2021. Only some representative current vectors are shown. The magenta rectangles in (a) are the region defined in Figure 3.2. 78

Figure 3.5 8-20-year bandpass filtered temperature anomalies averaged between 22-24.5 σ_θ in NW box (gray rectangle) regressed with 8-20-year bandpass filtered (a) SST, (b) SLP (shading, contour, and stipple) and 10-m wind anomalies, (c) wind stress curl and (d) Ekman pumping. In (a), contours are the correlation coefficients between 8-20 year bandpass filtered NW box subsurface temperature anomalies and 8-20 year bandpass filtered SST anomalies. The contour interval is 0.2 and only correlation coefficients greater than 0.8 are shown. The contour interval in (b) is 0.1 hPa (positive/negative is solid/dashed). Regressed wind vectors are shown as a whole for clarity. Stipples indicate the region exceeding 95% confidence level with the random-phase test. 82

Figure 3.6 Framework for TPDV. (a) Warm phase of TPDV is characterized by the strongest surface warming in the Niño4 region, off-equatorial western Pacific Gill-response, strong subsurface cooling, and extratropical cyclonic circulation. (b) Surfacing of off-equatorial northwestern subsurface temperature anomalies in the Niño4 region. (c) PMM (with contributions from KE) enhances the subsurface-produced equatorial disturbance in the Niño4 region. (d) Similar to the warm phase but with the sign reversed. 87

Figure S3.1 LFV spectrum for the combined raw detrended SST, SLP, 10-m wind, and subsurface temperature anomalies averaged between 22-24.5 σ_θ and 24.5-26 σ_θ . The horizontal dashed lines are the 90%, 95% and 99% confidence levels based on the bootstrap method. 89

Figure S3.2 Mean depth of (a) 22-24.5 σ_θ and (b) 24.5-26 σ_θ from 1950 to 2021. The contour interval is 20 m. 90

Figure S3.3 Mean temperature at (a) 45 m and (b) 75 m level averaged in the Niño4 region. Shown are all isopycnals between 22-25 σ_θ that intersect with these depth levels. 90

Figure S3.4 Same as Figure 3.3a but for (a) wind stress curl anomalies and (b) Ekman pumping..... 91

Figure S3.5 8-20-year bandpass filtered SST (shading) and SLP (contours, hPa) anomalies regressed with the 8-20-year bandpass filtered (a-d) KE index and (e-h) PMM SST index. The contour interval is 0.1 hPa (positive/negative is solid/dashed). Stipples indicate the regressed SST exceeding 95% confidence level with the random-phase test. Regressed SLP are shown as a whole for clarity. In all panels, the magenta rectangle indicates the KE region. The numbers indicate the KE and PMM index lead SST anomalies by months. . 91

Figure S3.6 Mean acceleration potential (shading) referenced to 1000 dbar and mean current vectors evaluated on (a) $22.5 \sigma_\theta$, (b) $23 \sigma_\theta$, (c) $23.5 \sigma_\theta$ and (d) $24 \sigma_\theta$. Only some representative current vectors are shown. Current data is from GODAS during 1980-2021. 92

Figure S3.7 Mean acceleration potential (shading) referenced to 1000 dbar evaluated on $23.5 \sigma_\theta$ and mean depth-integrated current vectors. Only some representative current vectors are shown. Current data is from GODAS during 1980-2021. 92

Figure S3.8 Hovmöller diagram of SSH anomalies along (a) 13°N (plotted from east to west), (b) 130°E (plotted north to south), and (c) equator (plotted from west to east). (d) Reconstructed subsurface temperature anomalies between $22-24.5 \sigma_\theta$ using MTM-SVD averaged along 6°N (shading) and $5^\circ\text{S}-5^\circ\text{N}$ (contour). The contour interval is 0.2°C (positive/negative is solid/dashed). (e) SST anomalies averaged between $5^\circ\text{S}-5^\circ\text{N}$. (f) TPDV index. The vertical dashed magenta lines indicate the longitude of 160°E and 150°W . The horizontal solid (dashed) green lines indicate strong and very strong El Niño (La Niña) events that peak in December based on the Oceanic Niño Index (ONI). All the data (a-c, e) are detrended and removed seasonal cycle only before plotting. SSH data is from GECCO3 (1948-2018). 93

Figure S3.9 Standard deviation of the 8-20-year bandpass filtered (a) temperature and (b) depth anomalies averaged between $22-24.5 \sigma_\theta$ 94

Figure S3.10 (a) Time series of subsurface temperature anomalies averaged in the NW box between $22-24.5 \sigma_\theta$. Hovmöller diagram of SSH anomalies along (b) 13°N , (c) 10°N , (d) 8°N and (e) 6°N . The vertical dashed magenta lines show the longitude of 140°E and 160°E . All the data are detrended and removed seasonal cycle only before plotting. SSH data is from GECCO3 (1948-2018). 94

Figure S3.11 8-20 year bandpass filtered SSH anomalies regressed with the 8-20 year bandpass filtered temperature anomalies averaged between $22-24.5 \sigma_\theta$ in NW box (magenta rectangle). Numbers in each panel indicate SSH anomalies lead subsurface temperature by months. Stipples indicate the region exceeding 95% confidence level with the random-phase test. 95

Figure S3.12 (a) Wintertime (December-February) and (b) annual response of 850 hPa geopotential height (shading and contour) and 850 hPa winds with specified 2°C SST

anomalies imposed in the magenta rectangle region shown in (a). Stipple indicates 95% significance level based on a Student's t-test..... 96

Figure S3.13 (a) Annual horizontal response structure of temperature averaged between 22-24.5 σ_θ to the superimposed anomalous wind fields associated with the positive phase of the TPDV. Same as (a) but for (b) longitude-depth and (c) longitude- σ_θ plot of the response of temperature at 6°N. Stipple indicates 95% significance level based on a Student's t-test. 96



List of Acronyms

CEOF	complex empirical orthogonal function
CP	central Pacific
ENSO	El Niño - Southern Oscillation
EOF	empirical orthogonal function
EUC	equatorial undercurrent
IPO	Interdecadal Pacific Oscillation
KE	Kuroshio Extension
LFV	local fractional variance
MTM-SVD	Multitaper Frequency-Domain Singular Value Decomposition
NECC	North Equatorial Countercurrent
NOAA	National Oceanic and Atmospheric Administration
NPGO	North Pacific Gyre Oscillation
NPO	North Pacific oscillation
NPP	North Pacific pathway
OGCM	ocean general circulation model
PC	principal component
PDO	Pacific Decadal Oscillation
PMM	Pacific Meridional Mode
Qnet	net surface heat flux

SLP	sea level pressure
SPDO	South Pacific Decadal Oscillation
SSA	subsurface spiciness anomalies
SSH	sea surface height
SSS	sea surface salinity
SST	sea surface temperature
STC	subtropical cell
STD	standard deviation
TPDV	tropical Pacific decadal variability
T-S	temperature-salinity
WSC	wind stress curl





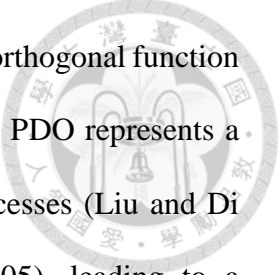
Chapter 1

Introduction

1.1 Pacific interannual to decadal climate variability

The Pacific Ocean is the world's largest and deepest ocean, covering over one-third of the planet's surface. It plays a vital role in the Earth's climate system by storing and transferring heat energy across the globe. The Pacific is also home to one of the most powerful interannual climate phenomena known as El Niño-Southern Oscillation (ENSO) (Timmermann et al., 2018). ENSO is a complex interaction of atmospheric and oceanic processes in the tropical Pacific (Bjerknes, 1964; Jin, 1997), occurring every 2-7 years. During an El Niño event, sea surface temperature (SST) anomalies (SSTA) in the equatorial central eastern Pacific exhibit abnormal warming, while the opposite scenario unfolds during a La Niña event. This warming/cooling has far-reaching impacts on weather patterns beyond the geographical boundaries of the Pacific, influencing precipitation patterns, temperature distributions, and wind regimes in various regions around the world (Lin and Qian, 2019) via atmospheric teleconnections (Alexander, 1990, 1992; Alexander et al., 2002; Liu and Alexander, 2007). Given the growing concerns about climate change and its potential consequences, accurate predictions of ENSO behavior under future climate scenarios are of paramount importance for informed decision-making and effective planning (Cai et al., 2021; Collins et al., 2010).

Since the late twentieth century, there has been a growing focus on understanding decadal and multidecadal climate variability, particularly in the Pacific (Folland et al., 2002; Minobe, 1997; Power et al., 1999; Trenberth and Hurrell, 1994; Zhang et al., 1997) and Atlantic Oceans (Bjerknes, 1964; Deser and Blackmon, 1993; Kushnir, 1994). Mantua et al. (1997)



identified the Pacific Decadal Oscillation (PDO) as the leading empirical orthogonal function (EOF) of monthly SSTA poleward of 20°N. The spatial structure of the PDO represents a basin-scale signature resulting from various superimposed physical processes (Liu and Di Lorenzo, 2018; Newman et al., 2016; Schneider and Cornuelle, 2005), leading to a predominance of one sign of variability in the tropics extending towards the eastern extratropics and an opposite sign of variability in the central North Pacific (Figure 1.1b). The resulting pattern is often referred to as the “warm phase” or “cold phase” depending on the sign of the anomalies in the central North Pacific (Deser and Phillips, 2006; Graham, 1994; Hare and Mantua, 2000; Trenberth, 1990). The PDO has been shown to have significant impacts on global climate (Wang et al., 2014; Xu et al., 2022; Zhang et al., 2020) and the North Pacific ecosystem (Mantua et al., 1997).

Apart from PDO, the second most prominent source of low-frequency variability in the North Pacific is associated with the second EOF mode of sea surface height (SSH) anomalies within the region 180°W-110°W, 25°N-62°N, or the second EOF mode of SSTA poleward of 20°N. The former is generally referred to as the North Pacific Gyre Oscillation (NPGO) (Di Lorenzo et al., 2008) (Figure 1.1c) while the latter is known as the Victoria Mode (Bond et al., 2003; Ding et al., 2015b). The NPGO measures changes in the North Pacific gyre circulation (Ceballos et al., 2009; Di Lorenzo et al., 2008) and is thus a good indicator of salinity, nutrients, and chlorophyll fluctuations. In contrast, the Victoria Mode is closely related to the onset of ENSO (Ding et al., 2015b), the development and propagation of the Madden-Julian Oscillation (MJO) (Wen et al., 2020), and other climatic variations in the North Pacific (Ding et al., 2015a; Pu et al., 2019; Zou et al., 2020).

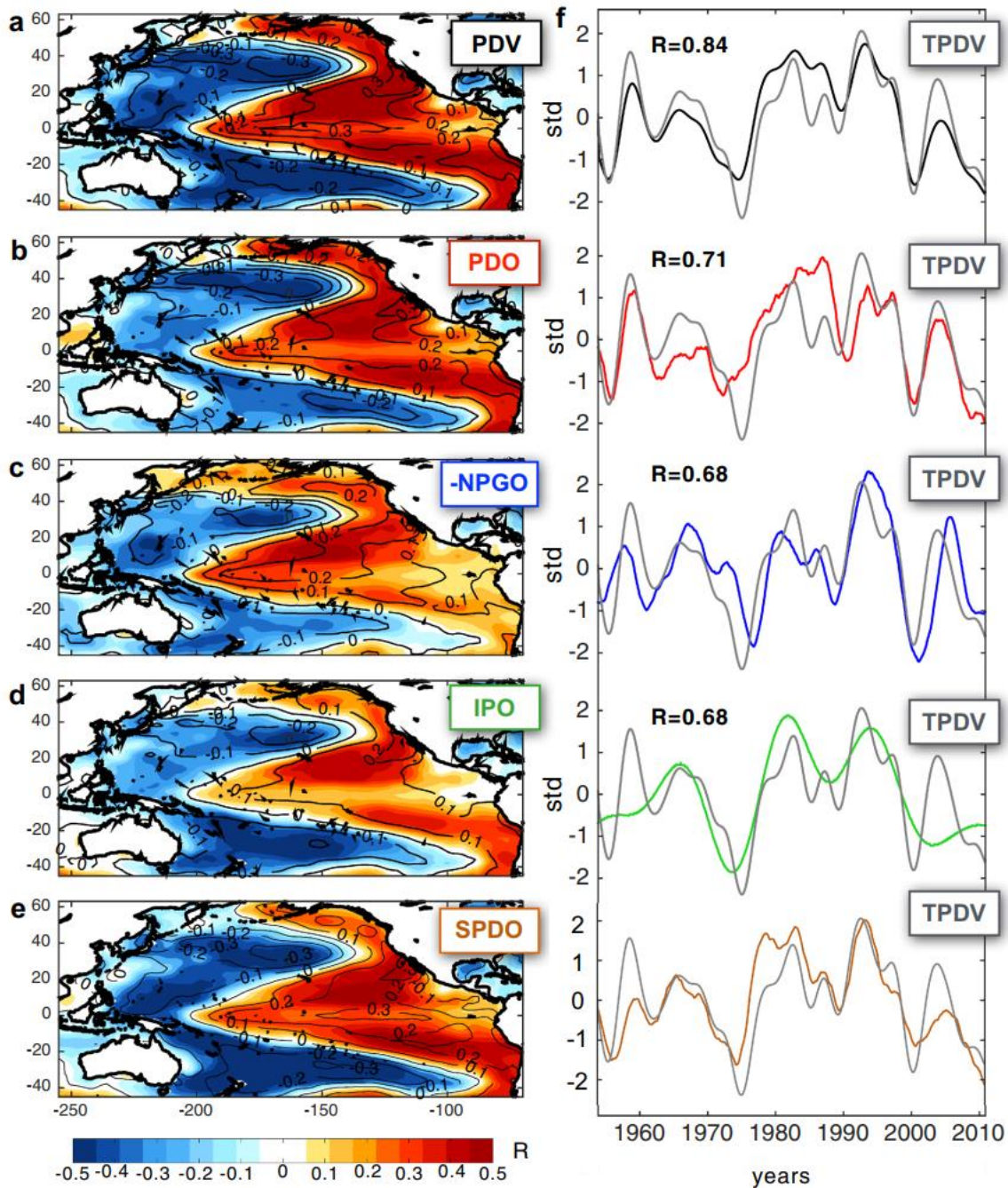
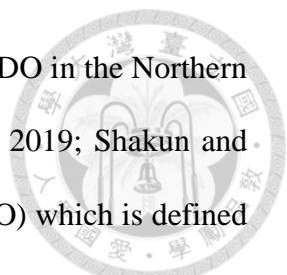


Figure 1.1 Patterns of Pacific low-frequency SST variability. Correlation maps between monthly NOAA ERSST.v3 SSTA and (a) Pacific Decadal Variability index defined as the first principal component (PC1) of 8-year low-pass SSTA over Pacific basin (45°S–65°N), (b) 8-year low-pass PDO index, (c) 8-year low-pass negative NPGO index, (d) IPO index, and (e) 8-year low-pass SPDO index. Black contours are regression coefficients (°C). The time series of the indices are shown in (f) and compared against a TPDV index defined as PC1 of 8 year low-pass SST over the equatorial Pacific (12°S–12°N). (source: Liu and Di Lorenzo 2018).



In the South Pacific, a significant decadal variation that mirrors the PDO in the Northern Hemisphere has also been identified (Hsu and Chen, 2011; Lou et al., 2019; Shakun and Shaman, 2009). It is termed the South Pacific Decadal Oscillation (SPDO) which is defined as the second EOF mode of SSTA poleward of 20°S (Chen and Wallace, 2015; Shakun and Shaman, 2009) (Figure 1.1e). The SPDO and PDO are commonly considered as the Southern and Northern Hemispheres expressions of the Pacific-wide Interdecadal Pacific Oscillation (IPO), which is defined as the dominant EOF of 13-year lowpass filtered SSTA over the entire Pacific (Power et al., 1999) (Figure 1.1d). The spatial structure of the IPO is qualitatively similar to that associated with ENSO (Figure 1.2d) but the IPO exhibits a larger meridional extent (Power et al., 2021). Consequently, the IPO is often referred to as the decadal manifestation of ENSO variability (Newman et al., 2016).

Recently, Di Lorenzo et al. (2023) proposed that all the aforementioned statistical climate modes can be decomposed into two empirical dynamical modes based on a linear inverse model: the Kuroshio-Oyashio Extension (KOE) and North Pacific-central Pacific (NP-CP) modes (Figure 1.2). The KOE mode exhibits multidecadal timescale variability with the center of action in the KOE region and central North Pacific. In contrast, the NP-CP mode exhibits decadal timescale variability with a center of action extending from the northeastern to the equatorial central Pacific, resembling the central Pacific ENSO and Pacific Meridional Mode (PMM) pattern. These two dynamical modes primarily arise from the bidirectional interaction between the tropics and extratropics, playing a fundamental role in elucidating the various basin-scale manifestations of Pacific decadal to multidecadal climate variability. Although extratropical-tropical air-sea coupling can explain the preferred time scale to a

certain degree, the physical processes responsible for the phase transition of the two dynamical modes remain unclear, warranting further investigation.

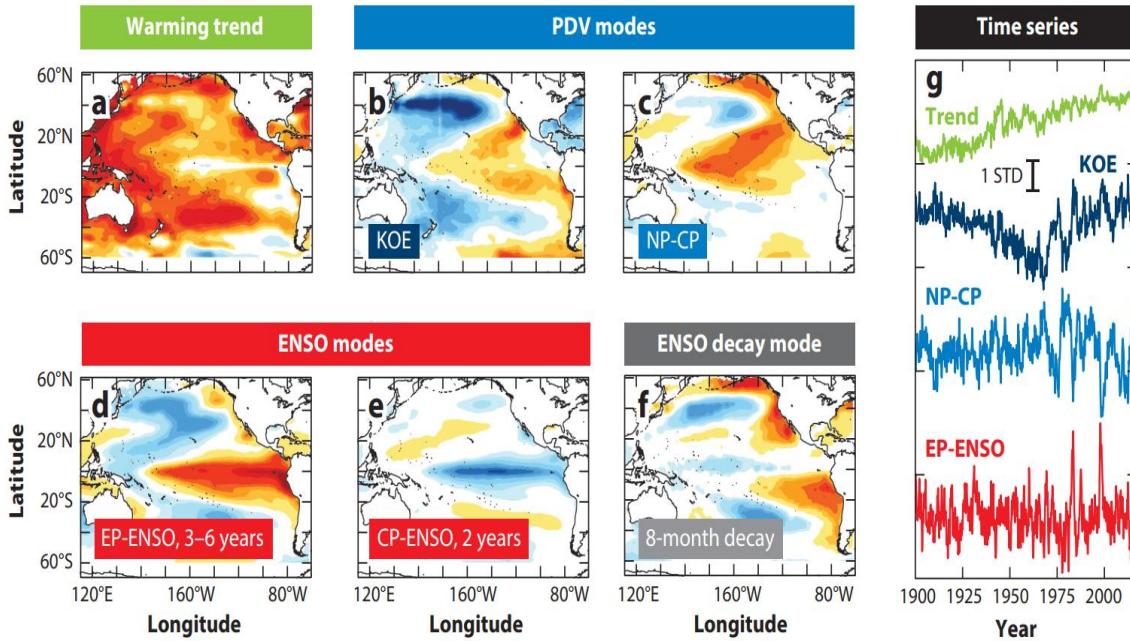
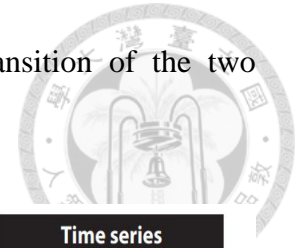


Figure 1.2 Dynamical modes of Pacific SSTA, derived from the ensemble average eigenmodes of the dynamical operator of linear inverse models. (a) warming trend, (b) KOE mode, (c) NP-CP mode, (d) eastern Pacific-ENSO mode, (e) central Pacific-ENSO mode and (f) ENSO decay mode. (g) The respective normalized time series (real) derived from HadISST. The units are nondimensional (-1, 1) and each pattern was normalized using the standard deviation of their correspondent real-part time series prior to taking the ensemble average. (source: Di Lorenzo et al. 2023)

1.2 Tropical Pacific Decadal Variability (TPDV)

Despite constituting a small fraction of the global surface, the equatorial Pacific is demonstrated to play a pivotal role in global temperature change (Kosaka and Xie, 2013, 2016). This is further confirmed by a model study suggesting that internal decadal variability in the tropical Pacific contributes significantly to the decrease in global mean surface temperature observed during the recent hiatus (Watanabe et al., 2014). Therefore, gaining a comprehensive understanding of decadal-scale climate variability in the tropical Pacific is

crucial for distinguishing between natural climate variability and human-induced climate change.

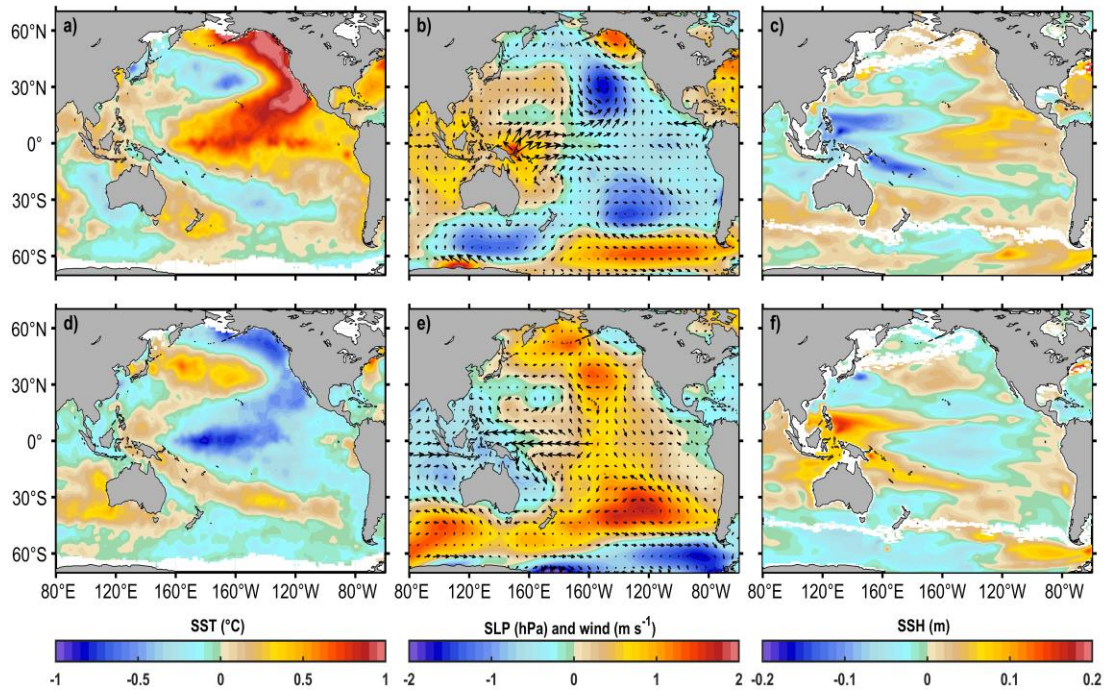
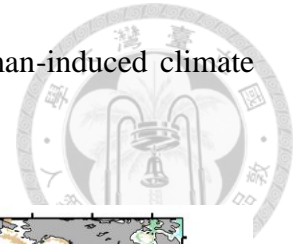


Figure 1.3 Observed basinwide changes associated with TPDV transitions. Differences of (a, d) SST, (b, e) sea level pressure (SLP) and 10-m wind, and (c, f) SSH between (top) 2013-2018 and 2007-2012 and (bottom) 2007-2012 and 2002-2007. The trend is linearly removed and anomalies are calculated by removing monthly averages over 1980-2020. SST data are from HadISST (Rayner et al., 2003), SSH is from GODAS (Behringer and Xue, 2004), SLP and winds are from NCEP-NCAR reanalysis (Kalnay et al., 1996).

The surface and subsurface changes associated with TPDV phase transitions are shown in Figures 1.3 and 1.4. The shift from the negative phase (2007-2012) to the positive phase (2013-2018) is marked by strong warming in eastern midlatitude, extending along the west coast of North America toward the central equatorial Pacific and cooling in the central-western midlatitude. The South Pacific exhibits a similar characteristic to its northern counterpart, albeit with a weaker magnitude. This SST anomaly pattern is qualitatively akin to the IPO pattern (Figure 1.1). Associated with the SSTA, negative SLP anomalies are

observed in the extratropical North and South Pacific, accompanied by strong westerlies in the equatorial western Pacific. The SLP anomaly structure in the North Pacific mirrors the North Pacific Oscillation (NPO) pattern while in the South it projects onto the Pacific-South American pattern (Okumura, 2013).

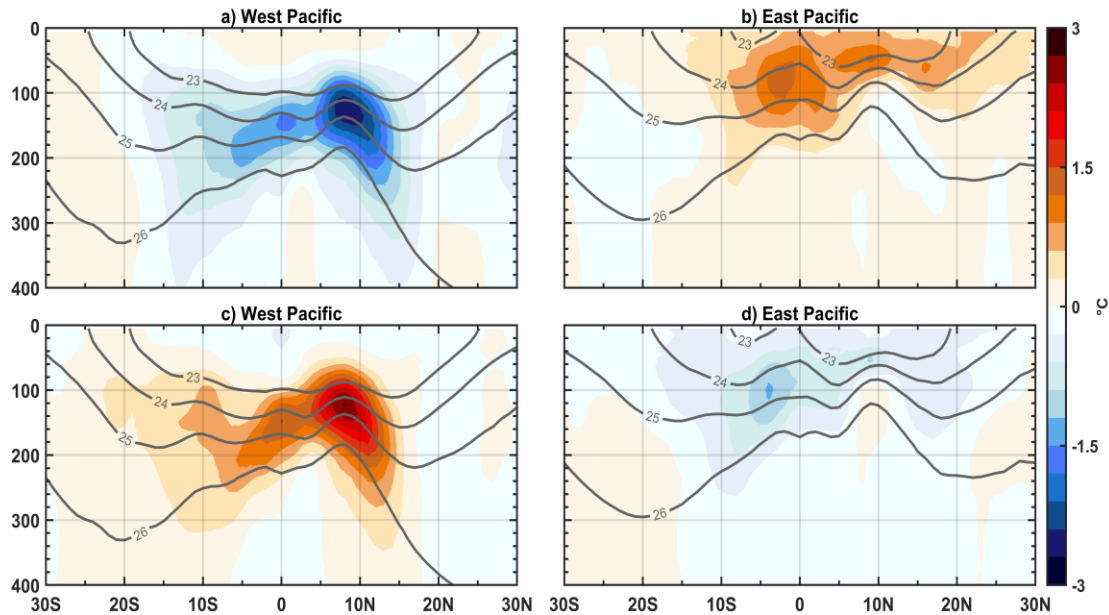
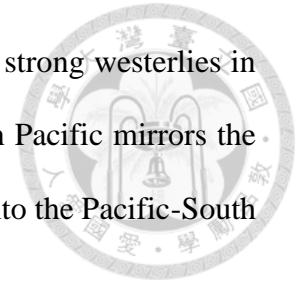


Figure 1.4 Same as **Figure 1.3** but for temperature anomalies averaged over the (left) western ($120^{\circ}\text{E}-180^{\circ}$) and (right) eastern ($180^{\circ}-60^{\circ}\text{W}$) Pacific. Contours indicate climatological values of potential density. Temperature data are from EN.4.2.2 (Good et al., 2013).

The SSH changes (a proxy for thermocline variations) exhibit pronounced zonal asymmetry in the tropical Pacific with a shallower thermocline in the west and a deeper thermocline in the central-eastern Pacific (Figure 1.4). The decadal-scale variability of the thermocline in the western Pacific may be linked to the westward-propagating oceanic Rossby waves (Capotondi et al., 2003; Capotondi and Qiu, 2022). Subsurface temperature changes in the western region are most dominant at $5^{\circ}-15^{\circ}\text{N}$ between the isopycnals 23-25 kg m^{-3} , primarily driven by local Ekman pumping (Capotondi and Qiu, 2022). In contrast, subsurface temperature changes in the eastern region are more confined to the equatorial

south Pacific at 0-5°S between the isopycnals 23-25 kg m⁻³. The opposite is qualitatively observed during the positive (2002-2007) to negative (2007-2012) phase transitions.

Internal TPDV is characterized by the strongest SSTA in the equatorial central Pacific, alternating between decadal periods of anomalously warm and cold events (Chunhan et al., 2021; Liu et al., 2022). During the peak phase of TPDV, tropical SST forcing induces atmospheric teleconnection (Alexander, 1992; Alexander et al., 2002), synchronizing decadal variance across the North and South Pacific (Di Lorenzo et al., 2023; Liu and Di Lorenzo, 2018; Zhao and Di Lorenzo, 2020). Therefore, TPDV shares common characteristics with other major statistical climate modes such as the PDO, NPGO, SPDO, and the IPO (Liu and Di Lorenzo, 2018), emphasizing the pivotal role of TPDV in Pacific climate variability.

TPDV has significant implications for global climate as it can influence the equatorial background mean state where interannual ENSO events dominate (McPhaden et al., 2011; Okumura et al., 2017b; Zhong et al., 2017). Any changes in the background mean state can modulate the amplitude and frequency of ENSO (Collins et al., 2010; Fedorov and Philander, 2000; Okumura et al., 2017b; Sun and Okumura, 2020; Zhao et al., 2016) as well as its teleconnections (Meehl and Teng, 2007; Power et al., 1999; Stevenson et al., 2012; Vecchi and Wittenberg, 2010). In addition, the persistence of decadal-scale climate variability, such as the IPO, can complicate the disentanglement of internal climate variability from anthropogenic climate change in the context of the global warming hiatus (England et al., 2014). Moreover, a recent study demonstrated that accurately reproducing the spatial structure and key mechanisms of TPDV remains a great challenge for Coupled Model Intercomparison Project Phase 6 models (Zhao et al., 2023). Therefore, understanding the

key mechanisms of internal TPDV is crucial for enhancing the prediction and management of the impacts of climate change on the Pacific and beyond.



1.3 Potential mechanisms of TPDV

TPDV as an ENSO residual

The spatial resemblance between ENSO and TPDV has led to a null hypothesis that TPDV arises as a residue of the long-term linear average of ENSO events (Vimont, 2005) or the nonlinearities inherent in ENSO dynamics (Cibot et al., 2005; Kim and Kug, 2020; Rodgers et al., 2004). The former can contribute to the SST pattern of TPDV from the developing to decaying phases of TPDV and from the random occurrence of uneven numbers of El Niño or La Niña events during different decadal epochs (Power et al., 2021). The latter gives rise to the spatial pattern of TPDV via the asymmetries in ENSO event-to-event variations, such as variations in event magnitude, duration, and location (Capotondi et al., 2020).

Some ENSO events can trigger the phase transition of TPDV through various mechanisms. Firstly, the strong El Niño-induced nonlinear dynamical heating in the ocean mixed layer can cause a transition of TPDV from a positive to a negative phase (Liu et al., 2022). Secondly, the onset of ENSO events combined with the establishment of heat content anomalies in the off-equatorial western Pacific (Meehl et al., 2016) (Figure 1.5) can facilitate the phase change of TPDV (Meehl et al., 2021). Specifically, these ENSO events can trigger off-equatorial oceanic Rossby waves, contributing to the accumulation of ocean heat content in the northwestern and southwestern Pacific (Capotondi and Alexander, 2001; Capotondi et al., 2003). Subsequently, both locally generated and Rossby wave-induced oceanic heat content are redistributed equatorward due to ENSO-associated wind anomalies, leading to a phase transition in TPDV (Meehl et al., 2021).

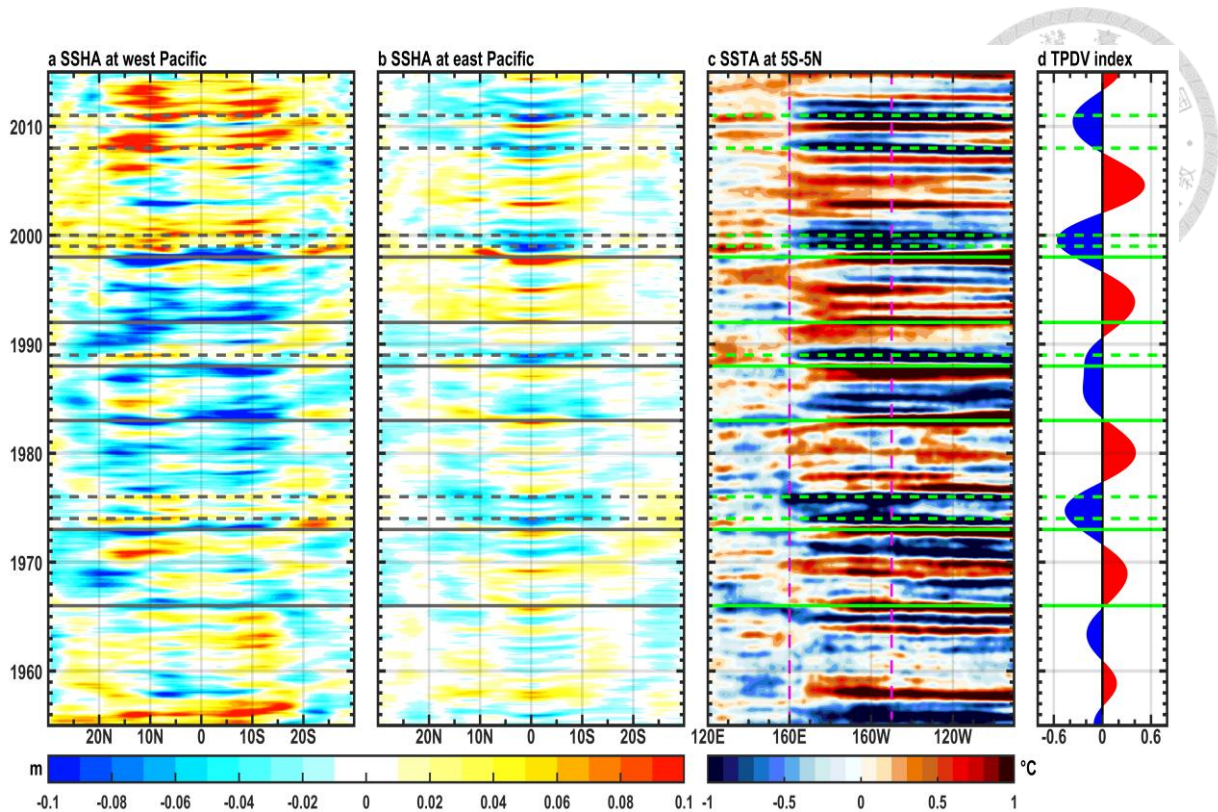


Figure 1.5 Latitude-time plot of SSH anomalies averaged (a) west and (b) east of the dateline. (c) Latitude-time plot of SSTA averaged over 5°S-5°N. (d) TPDV index defined as 8-20 year bandpass filtered SSTA over 5°S-5°N, 160°E-150°W. In a-c, SSTA and SSH anomalies are obtained by removing the linear trend and the climatological monthly mean over 1950-2020. The horizontal solid (dashed) green lines indicate strong and very strong El Niño (La Niña) events that peak in December based on the Oceanic Niño Index (ONI). SST data are from HadISST (Rayner et al., 2003) and SSH is from GECCO3 (Köhl, 2020).

Mean advection of temperature anomalies (the $\bar{v}T'$ mechanism)

The $\bar{v}T'$ mechanism, where \bar{v} denotes climatological mean circulation and T' is temperature anomalies, was proposed to account for the phase transition of TPDV with the time scale determined by the equatorward ventilation from the subtropical region (Figure 1.6). Gu and Philander (1997) suggested that extratropical surface thermal anomalies can subduct and propagate westward and equatorward through the subsurface branch of the subtropical cell (STC) (Liu, 1994; McCreary and Lu, 1994). These anomalies then upwell, initiating an anomaly of the opposite sign at the equator. Furthermore, subsurface-induced

anomalies further grow due to equatorial positive feedback, leading to the opposite phase of TPDV, which in turn teleconnects to the extratropics and contributes to the formation of surface anomalies there. While some subsequent studies have questioned the effectiveness of extratropical North Pacific subsurface temperature anomalies in facilitating the phase transition of TPDV (Hazeleger et al., 2001; Schneider et al., 1999a), temperature anomalies with density-compensated salinity signals or spiciness (Munk, 1981) have been suggested to play a more important role, particularly in the Southern Hemisphere (Tatebe et al., 2013; Zeller et al., 2021).

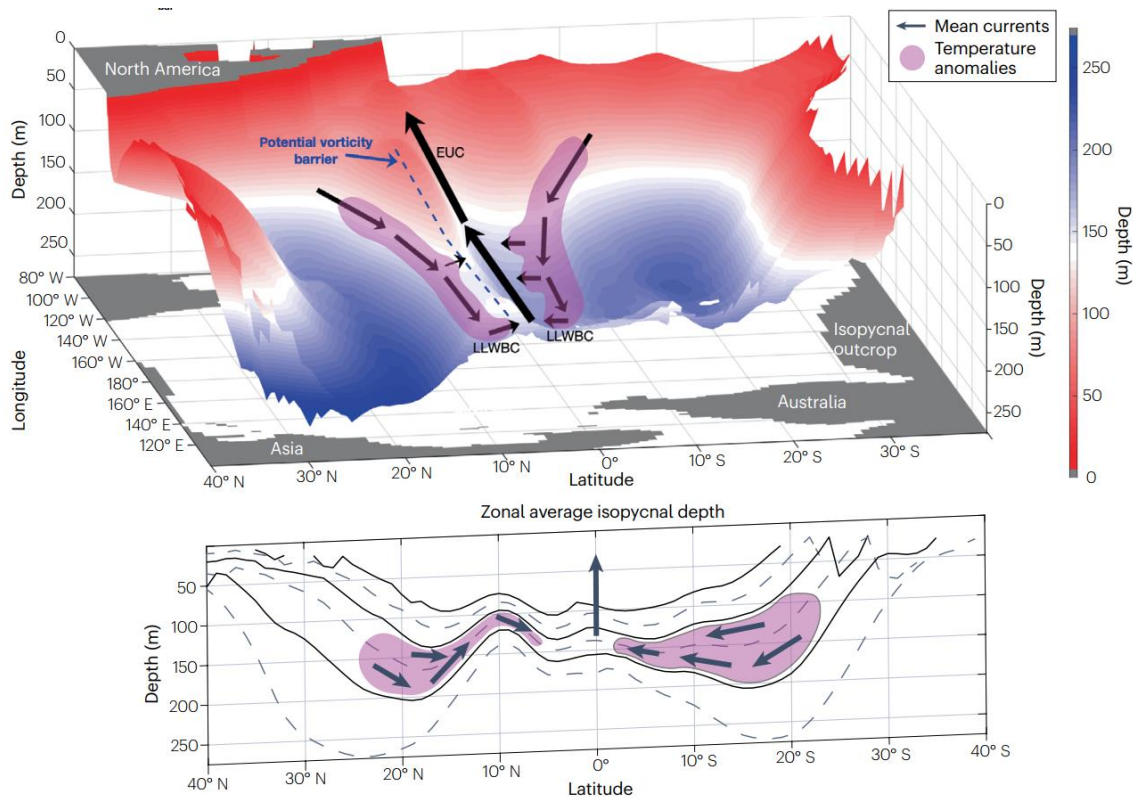
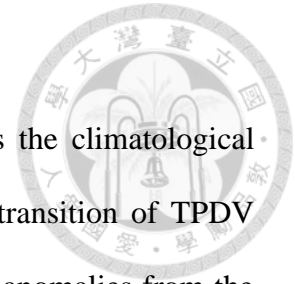


Figure 1.6 The advection of spiciness anomalies (pink shading) by the mean circulation (black arrows) on the 25.0 kg m⁻³ isopycnal surface. Shading indicates isopycnal depth, and the dashed blue line indicates the ‘potential vorticity barrier’ in the 5°–10°N latitude band. The lower panel depicts zonally averaged isopycnal depths (from 23 to 25.5 kg m⁻³ with a spacing of 0.5 kg m⁻³; solid lines: 23, 24 and 25 kg m⁻³; dashed lines: 23.5, 24.5 and 25.5 kg m⁻³), and the flow of equatorward spiciness anomalies along isopycnal surfaces. (source: Capotondi et al. 2023)

Anomalous advection of mean temperature (the $v'\bar{T}$ mechanism)

The $v'\bar{T}$ mechanism, where v' denotes circulation anomaly and \bar{T} is the climatological mean temperature, provides an alternative explanation for the phase transition of TPDV compared to the mean equatorial upwelling of subtropical temperature anomalies from the pycnocline (Figure 1.7). According to this mechanism, an increase in the rate of the STC enhances the equatorial upwelling of extratropical cold water, leading to the cooling of the equatorial surface temperature and consequently, transforming TPDV into a cold phase, and vice versa (Kleeman et al., 1999). Although there is a strong relationship between STC variability and TPDV in both models (Capotondi et al., 2005; Cheng et al., 2007; Farneti et al., 2014a; Klinger et al., 2002; Lübbecke et al., 2008; Solomon et al., 2003) and observations (McPhaden and Zhang, 2002, 2004), the exact contribution of STC variability to the phase transition of TPDV remains largely unknown due to the nearly in-phase relationship between equatorial SST variability and STC changes at the decadal time scale (Capotondi et al., 2023). Additionally, the strength of the STC depends strongly on the location and magnitude of the wind forcing, the origin of which is still challenging to determine unambiguously (Capotondi and Qiu, 2022; Graffino et al., 2019). These wind anomalies might be driven by extratropical internal atmospheric variability or as a response to equatorial SST anomalies (Stuecker, 2018; Zhang et al., 2022). In addition, some studies suggested that the Atlantic Ocean can also contribute to these wind anomalies via atmospheric teleconnection (Sun et al., 2017). Consequently, the precise importance of the STC-related mechanism to TPDV is yet to be fully understood.



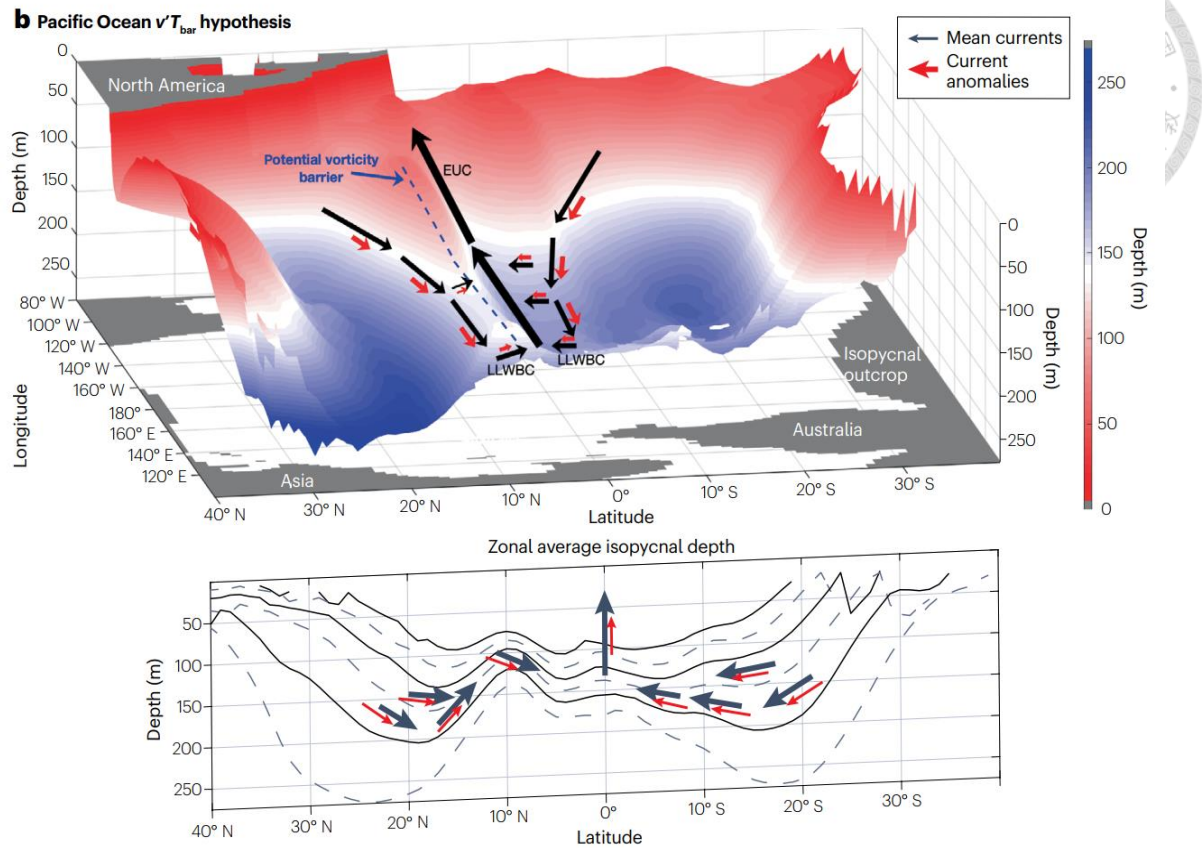


Figure 1.7 Same as **Figure 1.6**, but for the $v'\bar{T}$ mechanism. The mean (anomalous) flows are denoted by black (red) arrows. (source: Capotondi et al. 2023).

Wave propagation of temperature anomalies

The propagation of Rossby waves can induce isopycnal displacements that generate temperature anomalies on climatological mean isopycnal surfaces, contributing to the phase transition of TPDV (Capotondi and Alexander, 2001; Capotondi et al., 2003; Capotondi et al., 2023). Specifically, wind-forced oceanic Rossby waves in the off-equatorial region propagate slowly westward. After reaching the western boundary, these waves move equatorward along the boundary as coastal Kelvin waves and then eastward along the equator as equatorial Kelvin waves. The equatorial arrival of these waves then alters the depth of the thermocline and initiates an opposite sign of equatorial SSTA, causing a phase transition of

TPDV (Farneti et al., 2014b; Galanti and Tziperman, 2003; Jin et al., 2001; Knutson and Manabe, 1998; Lysne et al., 1997; Meehl and Hu, 2006; Tatebe et al., 2013; White et al., 2003) (Figure 1.8).

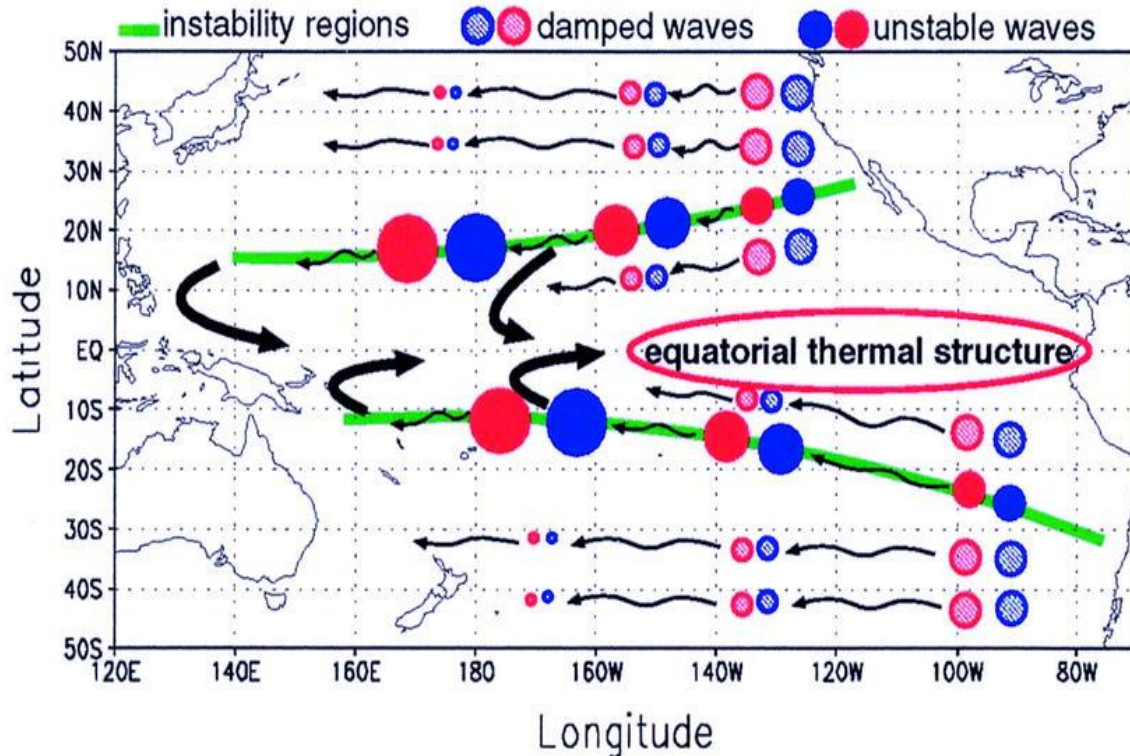
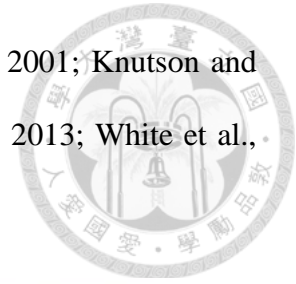
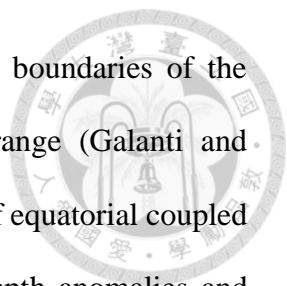


Figure 1.8 A wave teleconnection from the midlatitude Pacific to the equator. Midlatitude planetary Rossby waves travel westward at all latitudes and are damped. The waves that are amplified in baroclinically unstable regions of the subtropical gyre arrive to the equator with a larger amplitude and therefore dominate the midlatitude signal there. (source: Galanti and Tziperman 2003)

Several mechanisms have been proposed to elucidate the decadal-scale tropical climate variability induced by Rossby waves. Firstly, the zonal coherency of wind forcing, which becomes increasingly pronounced at decadal timescales, can effectively excite large-amplitude Rossby waves that maximize thermocline depth variability in latitudinal bands of 10-15°N and 10-14°S (Capotondi et al., 2003). Secondly, planetary Rossby waves originating in the eastern extratropics of both hemispheres can be significantly amplified due to



baroclinic instability when traveling westward along the equatorward boundaries of the subtropical gyres, resulting in longer transit times in the decadal range (Galanti and Tziperman, 2003) (Figure 1.8). Finally, the slow eastward propagation of equatorial coupled waves (White et al., 2003), arising from the coupling of isopycnal depth anomalies and anomalous zonal wind stress (Tatebe et al., 2013), can extend the delayed negative feedback to equatorial SST variability at decadal timescales.

Intrabasin atmospheric drivers

Apart from the oceanic processes mentioned earlier, atmospheric processes along the meridional axis within the Pacific basin can also contribute to TPDV. Based on model simulations and observations, Barnett et al. (1999) proposed that large-scale low-frequency atmospheric circulation in the North Pacific can induce zonal wind stress changes in the western-central equatorial Pacific. These changes subsequently provide feedback on the mean state of the thermocline, causing low-frequency tropical climate variability. This hypothesis is established through Hadley cells, which constitute the primary atmospheric conduit for transferring climate signals from the extratropics to the equator. A later study based on a 137-year simulation of a fully coupled general circulation model suggested that midlatitude SSTA can induce equatorial surface wind stress anomalies (Pierce et al., 2000). These anomalies, in turn, modulate the east-west slope of the equatorial thermocline, affecting tropical decadal-scale climate variability. Additionally, a similar mechanism has been proposed in the Southern Hemisphere where the Pacific-South American pattern can modulate southeasterly trade winds, leading to ENSO-like decadal climate variability (Okumura, 2013).

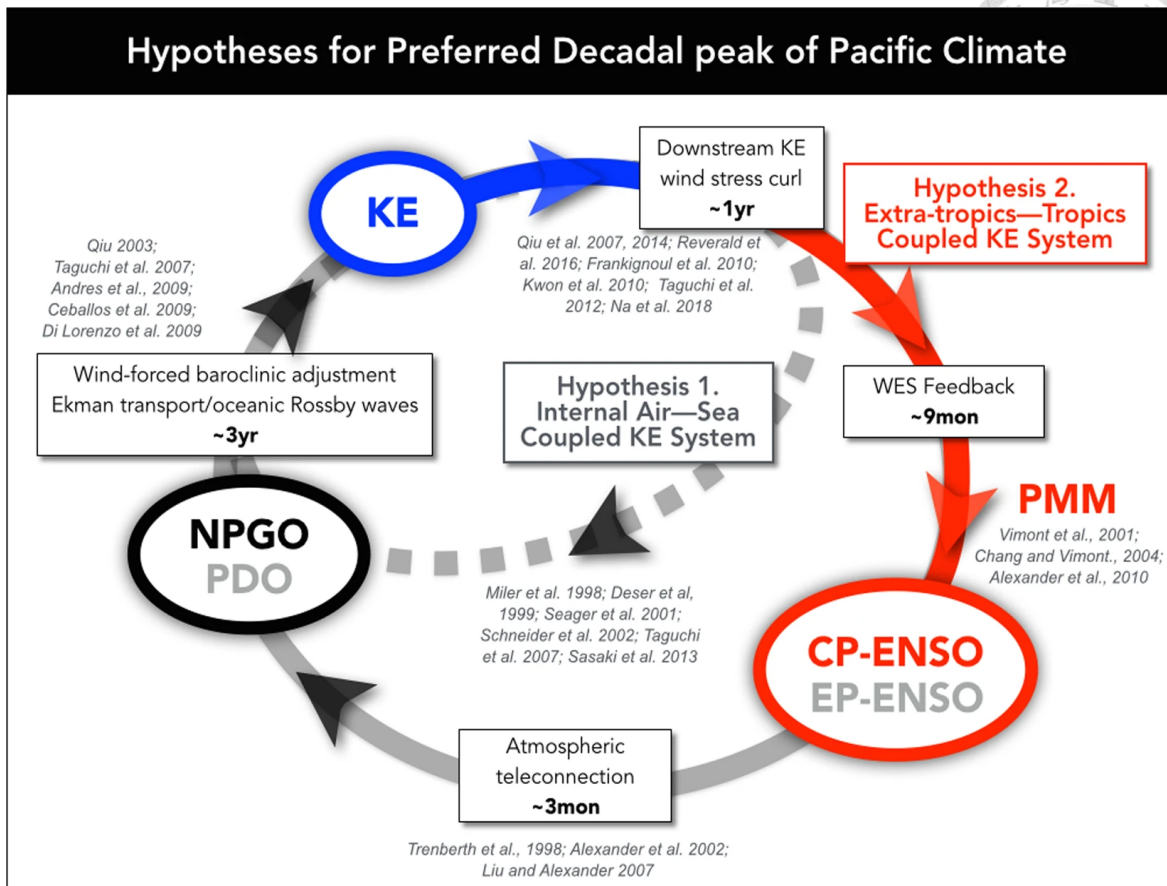
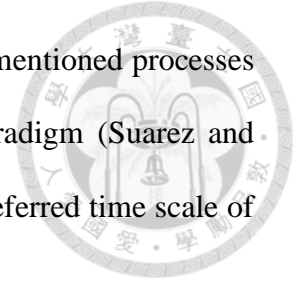


Figure 1.9 Proposed framework for TPDV. (source: Joh and Di Lorenzo 2019)

Recent research has proposed a framework for TPDV associated with the extratropical-tropical ocean-atmosphere interaction (Joh and Di Lorenzo, 2019). Specifically, during the positive phase of TPDV, equatorial SST warming induces anomalous extratropical atmospheric response (Alexander et al., 2002; Trenberth et al., 1998), thereby driving westward propagating Rossby waves (Ceballos et al., 2009; Qiu, 2003; Taguchi et al., 2007). The arrival of oceanic Rossby waves at the western boundary then modifies the Kuroshio Extension (KE) structure, leading to persistent downstream wind stress curl anomalies (Qiu et al., 2014; Qiu et al., 2007) that project onto the atmospheric forcing of the PMM (Joh and Di Lorenzo, 2019). The PMM then strengthens equatorial SSTA (Di Lorenzo et al., 2015; Zhao and Di Lorenzo, 2020), resulting in a negative TPDV phase after around five years

(Figure 1.9). The reverse cycle is simply the opposite sign of the aforementioned processes (Di Lorenzo et al., 2023). This hypothesis is a delayed oscillator paradigm (Suarez and Schopf, 1988) with delayed negative feedback which determines the preferred time scale of the oscillation given by the westward propagating Rossby wave.



Interbasin teleconnections

In the zonal axis, changes in the global Walker circulation associated with interbasin interaction can also contribute to the tropical Pacific climate (Cai et al., 2019) (Figure 1.10). Specifically, low-frequency surface warming in the Indian Ocean has been proposed to strengthen the atmospheric Walker circulation, increasing surface easterlies in the western-central Pacific, leading to a La Niña-like state through tropical atmosphere-ocean coupling (Luo et al., 2012) (Figure 1.10a). However, the influence of the Indian Ocean appears to have weakened in recent decades (Dong and McPhaden, 2017; Han et al., 2014) (Figure 1.10c). In contrast, the Atlantic Ocean exhibited a stronger impact on Pacific decadal climate variability from 1980 onwards (Figure 1.10c). Tropical Atlantic warming is demonstrated to intensify the atmospheric Walker circulation (Kucharski et al., 2016; Kucharski et al., 2011; Li et al., 2016; McGregor et al., 2014; Ruprich-Robert et al., 2017), leading to cooling in the central-eastern equatorial Pacific (Li et al., 2016; McGregor et al., 2014) (Figure 1.10b). Additionally, the influence of the tropical Atlantic on the Pacific can be strengthened by the Indian Ocean through the warming induced by the Atlantic Ocean in the Indo-Western Pacific (Li et al., 2016). This, in turn, further favors a La Niña-like response by enhancing the easterlies in the equatorial Pacific (Kug and Kang, 2006; Ohba and Ueda, 2007) (Figure 1.10d).

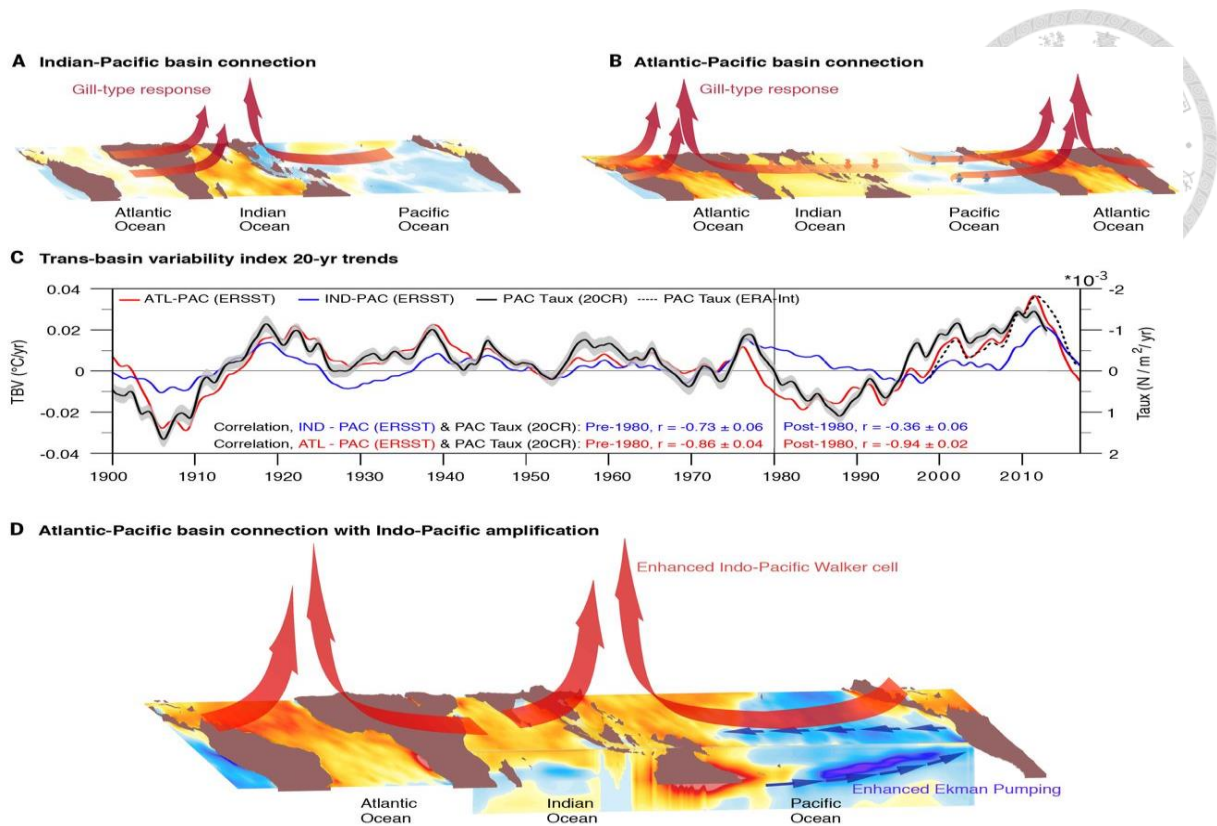


Figure 1.10 Decadal interbasin connections with the Pacific. (a) Indian Ocean warming induces a Gill-type response that increases surface easterlies and cold SSTA in the western Pacific. (b) Atlantic Ocean warming creates a Gill-type response resulting in anomalous easterlies and cold SSTA over the western and western-central Pacific, respectively. (c) Sliding-window 20-year trends of interbasin SST differences (ERSST) and equatorial western Pacific wind stress. The wind stress and its 1-standard deviation spread (shading) are from a 56-member reanalysis of the 20th-century climate. Wind stress from Extended Reanalysis-Interim for the post-1979 period is also used. Pre- and post-1980 correlations between the transbasin SST (ERSST) and the ensemble-mean equatorial zonal wind trends are provided, along with the 1-standard deviation spread of correlations from the 56 realizations. Indian (IND), Pacific (PAC), and Atlantic (ATL) basin SST are calculated over 20°S-20°N and 21°E-120°E, 20°S-20°N and 121°E-90°W, and 20°S-20°N and 70°W-20°E, respectively. The Pacific wind is computed over 6°S-6°N, 180°E-210°E. (d) The atmospheric circulation and surface temperature changes generated owing to Atlantic warming in (b) are amplified by the Pacific Bjerknes feedback and IOD-Pacific interactions. The depth-longitude section in (d) illustrates the subsurface temperature and circulation anomalies in the Indo-Pacific. In (a), (b), and (d), the color shading indicates temperature, with red being warmest and blue being coolest. (source: Cai et al. 2019)

1.4 Thesis objectives and structures

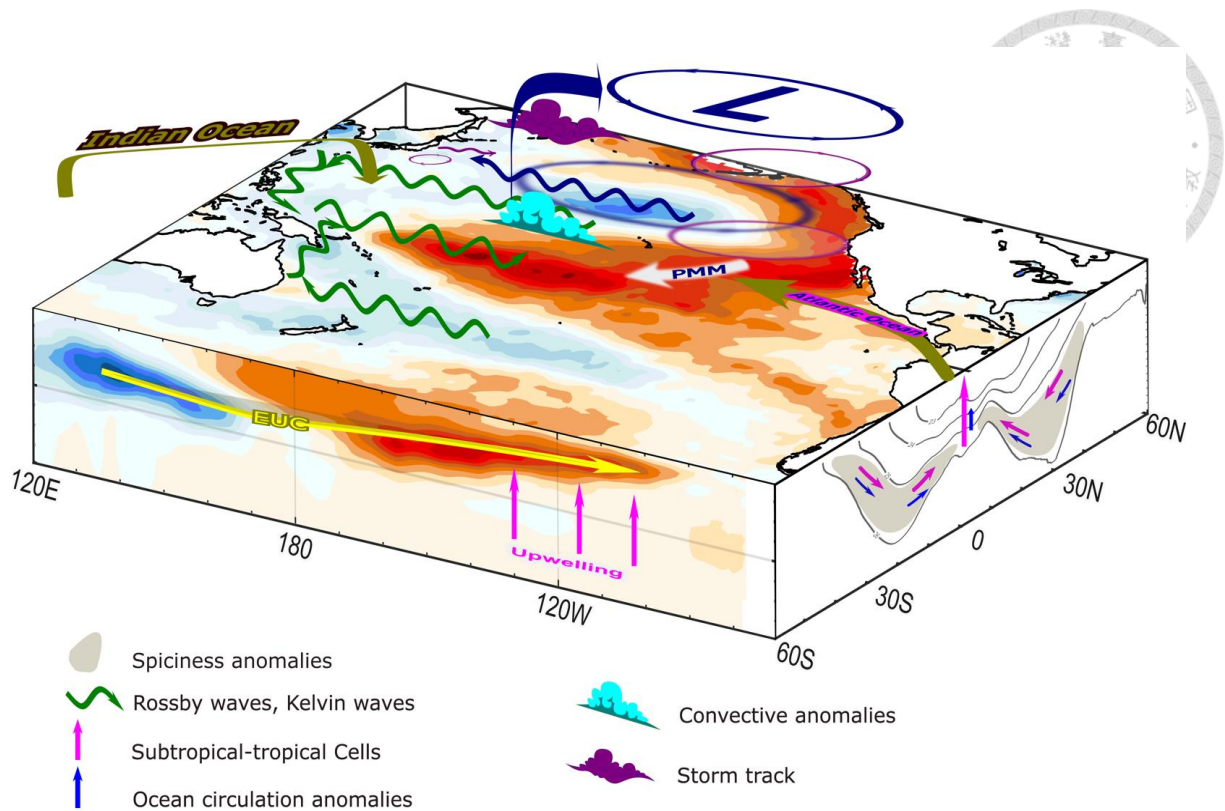
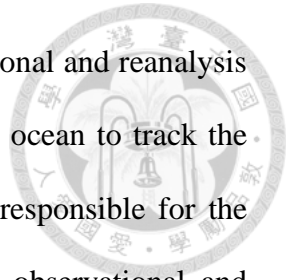


Figure 1.11 Processes and mechanisms associated with TPDV. The warm phase of TPDV, characterized by the strongest equatorial positive SSTA (shading, upper), induces convective heating anomalies and cyclonic circulations in the extratropical North (blue circle) and South Pacific. The green arrows signify wave propagation mechanisms, including westward-propagating Rossby waves, followed by equatorward movement along the boundary as coastal Kelvin waves and along the equator as equatorial Kelvin waves. The contribution from the Indian and Atlantic Oceans is also represented by olive green arrows. On the right, subsurface processes proposed to explain the TPDV phase transition involve the propagation of spiciness anomalies (gray shading) by mean STC (pink arrows), along with variability in the strength of the STC (blue arrows). The decadal framework proposed by Joh and Di Lorenzo (2019) is depicted, indicating the Aleutian Low/NPO (blue circle) inducing westward-propagating Rossby waves (blue arrow) to change KE state, leading to storm track change to excite downstream atmospheric response (purple circle), contributing to the forcing of the PMM (white arrows) which in turn drives to TPDV.

While various mechanisms have been proposed to explain TPDV, the primary mechanism driving its phase transition remains largely unknown (Figure 1.11). This thesis aims to enhance our understanding of the ocean's role in TPDV by investigating the impact of remotely generated subsurface temperature anomalies. The research focuses on two main themes. First, identifying a low-frequency subsurface propagating mode and the underlying



physical processes that generate this mode through analysis of observational and reanalysis datasets. We employ the “spiciness” variable as a passive tracer in the ocean to track the subsurface propagating pattern. Second, determining the mechanisms responsible for the phase reversal and the preferred time scale of TPDV by examining observational and reanalysis datasets. Furthermore, we conduct several numerical experiments to support the findings.

The following two Chapters (Chapter 2 and Chapter 3) are presented as independent manuscripts that have been submitted for publication. Therefore, each Chapter is organized with its Introduction, Methods, Results, Summary, and Discussion section. For brevity, the references from each Chapter are combined into a single bibliography at the end of the thesis.

In Chapter 2, we investigate the surface forcing of isopycnal spiciness anomalies, paying specific attention to the Aleutian Low and PDO. Moreover, we scrutinize the physical processes that are responsible for the creation of subsurface spiciness anomalies. This chapter has been published as a research article in *Climate Dynamics*.

In Chapter 3, we investigate the origin of water upwelling in the equatorial central Pacific. Specifically, we focus on two distinct isopycnal ranges, characterized by tropical and extratropical origins, respectively. We also propose a comprehensive framework for TPDV that incorporates the role of tropical subsurface temperature anomalies, Kuroshio Extension, and Pacific Meridional Mode. The finding of this Chapter is to be submitted for publication in *npj climate and atmospheric science*.

In Chapter 4, we discuss and conclude the main findings of the study.

Chapter 2

Aleutian Low/PDO forces a decadal subsurface spiciness propagating mode in the North Pacific



This Chapter is based on the publication:

San S-C and Tseng Y-h (2023). Aleutian Low/PDO Forces a Decadal Subsurface Spiciness Propagating Mode in the North Pacific. *Climate Dynamics*. DOI: 10.1007/s00382-023-06938-w

Preface

Analysis of observational data reveals the existence of a decadal subsurface spiciness mode that involves ocean-atmosphere coupling in the North Pacific. Specifically, the Aleutian Low, the dominant atmospheric forcing of the Pacific Decadal Oscillation (PDO), drives a dipole pattern of positive and negative spiciness anomalies in the eastern midlatitude and subtropics, respectively. These anomalies then propagate equatorward along a deflected route defined by the mean acceleration potential. The positive anomaly can be observed at 14°N after seven years of propagation while the downstream negative anomaly can be tracked to 10°N after three years of its occurrence. In addition, a negative spiciness anomaly appears in the midlatitude, followed by the formation of the positive spiciness anomaly two years later. It takes a similar pathway toward the tropics. Further analysis demonstrates the strong connection between the equatorial sea surface temperature variability and the extratropical spiciness anomalies. These, in turn, potentially lead to a decadal climate oscillation in the North Pacific involving extratropical-tropical interaction.

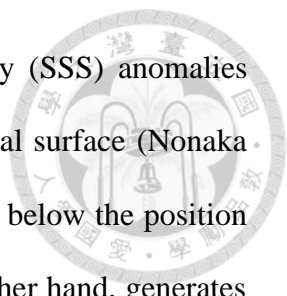
The dominant physical processes responsible for the subsurface spiciness variability are significantly different between the eastern midlatitude and subtropical North Pacific. In the midlatitude, isopycnal spiciness variability exhibits similar characteristics as the temperature variations at around 50-120 m depth, mainly produced via the subduction, reemergence, and anomalous advection across mean spiciness gradients. In contrast, interior subtropical spiciness variability follows the evolution of salinity anomalies at around 120-250 m. Subduction, spice injection, and anomalous advection generate the isopycnal spiciness variability.



2.1 Introduction

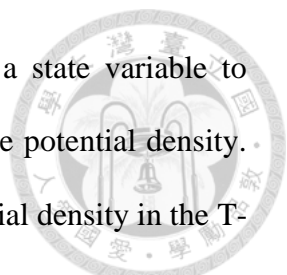
The low-frequency dynamics of subsurface temperature/salinity anomalies in the eastern Pacific Oceans have long been an active theme of research due to their important role in connecting extratropics with the tropics (Gu and Philander, 1997; Schneider, 2000, 2004). After a positive temperature anomaly is formed in the subtropical North Pacific, it is then advected adiabatically by the mean current westward and equatorward along isopycnal surfaces toward the tropical region (Kolodziejczyk and Gaillard, 2012; Sasaki et al., 2010). Along the equator, the anomaly flows east by the Equatorial Undercurrent (EUC), upwells, and warms the surface in the central-eastern equatorial Pacific. The surface warming also concurrently relaxes the local easterlies. Therefore, this warming is further enhanced via the positive Bjerknes feedback. Subsequently, the equatorial warming forces deep atmospheric convection that propagates into the extratropical North Pacific through the Pacific-North American teleconnection (Alexander, 1990, 1992). This atmospheric perturbation modulates the strength of the Aleutian Low, zonal wind anomalies, and hence turbulent heat flux in the midlatitude. Eventually, a negative subsurface temperature anomaly is generated and then propagates along a similar path of the positive anomaly toward the equator. This could form a decadal climate variability in the North Pacific with the time scale determined by the equatorward ventilation of the anomalous signals (Gu and Philander, 1997).

The generation of subsurface temperature/salinity anomalies can be classified into two distinct mechanisms: subduction and injection. Subduction occurs when an isopycnal is exposed to the surface and allows sea surface signals to follow the outcrop line toward the interior ocean (Kolodziejczyk and Gaillard, 2012; Nonaka and Sasaki, 2007). Therefore, the meridional displacement of the outcrop line which is governed by the compensated



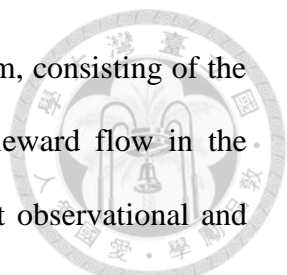
contribution of sea surface temperature (SST) and sea surface salinity (SSS) anomalies determines the positive or negative sign of the anomaly on the isopycnal surface (Nonaka and Sasaki, 2007). This mechanism generates anomaly locally, i.e., just below the position of the outcrop line. The injection mechanism (spice injection), on the other hand, generates subsurface anomaly further equatorward away from the isopycnal outcrop position and is responsible for the positive anomaly (Kolodziejczyk and Gaillard, 2012; Luo et al., 2005; Wang and Luo, 2020; Yeager and Large, 2004). The injection occurs when the examined isopycnal is not exposed to the surface, but the large unstable vertical salinity gradient in conjunction with weak stratification in winter favors convective mixing at the base of the mixed layer (Yeager and Large, 2004). As a result, the surface saline water is injected into the ocean interior, creating a density-compensating layer of temperature and salinity anomalies, termed spiciness anomaly, at the base of the mixed layer (Wang and Luo, 2020; Yeager and Large, 2004). Furthermore, subsurface anomaly generation involving atmospheric stochastic forcing is also proposed. In particular, the ocean filters the overlying atmospheric noise (Hasselmann, 1976) resulting in a large-scale first baroclinic mode pressure response. The anomalous geostrophic advection then crosses the mean spiciness gradients which in turn generate low-frequency subsurface spiciness variability (Kilpatrick et al., 2011). Isopycnal spiciness anomaly formation via this mechanism has also been shown to dominate in model simulation, leading to a decadal spiciness mode in the tropical North Pacific (Schneider, 2000).

The spiciness variable, which is often represented as temperature or salinity on a certain isopycnal surface (Kolodziejczyk and Gaillard, 2012; Li et al., 2012; Zeller et al., 2021), has been increasingly employed in recent literature to investigate low-frequency ocean climate

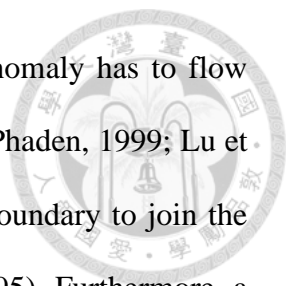


variability. Initially, spiciness (or potential spicity) is constructed as a state variable to characterize the rest information of thermodynamics not included by the potential density. Therefore, isolines of spiciness are required to be orthogonal with potential density in the T-S diagram (Huang, 2011; Huang et al., 2018, 2021; Müller and Willebrand, 1986; Munk, 1981; Stommel, 1962; Veronis, 1972). Spiciness defined in this way is assumed to be dynamically passive, accurately measuring mixing along isopycnal surfaces (Veronis, 1972). However, later studies identified that such orthogonal constraint is ambiguous because the scaling in the axes of the T-S diagram can vary in tandem with the thermal expansion and haline contraction coefficients (Flament, 2002; Jackett and McDougall, 1985; McDougall and Krzysik, 2015). In addition, the passive behavior of spiciness lies in its variations along isopycnal surfaces but not the inherited property of any thermodynamic variable (McDougall et al., 2021; McDougall and Krzysik, 2015). McDougall and Krzysik (2015) sacrificed the orthogonal enforcement but strictly required the variation of spiciness along isopycnal surfaces to be proportional to the isopycnal water-mass variations, expressed in density units. A solid theory available for the construction of spiciness so far is still a matter of ongoing debate and largely evolving along two main streams: orthogonality (Huang et al., 2021) and nonorthogonality (McDougall et al., 2021) with the potential density in the T-S diagram. Recently, Tailleux (2021) suggested that before the construction of spiciness, a neutral density variable (Tailleux, 2016) that is materially conserved should be well-defined first, and then any material density function can be used to construct spiciness quantified in terms of its anomaly along the neutral surfaces.

The corridor for the eastern extratropical subsurface signals propagating toward the equator is via the so-called subtropical cell (STC) (Liu, 1994; Liu et al., 1994; McCreary and

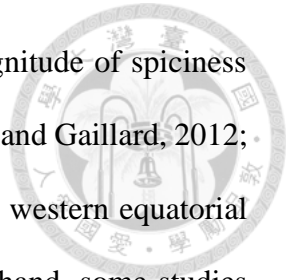


Lu, 1994), a shallow overturning circulation confined to the upper 500 m, consisting of the subsurface equatorward branch, equatorial upwelling branch, and poleward flow in the surface Ekman layer (Capotondi et al., 2005; Schott et al., 2004). Past observational and modeling studies have demonstrated the existence of the STC and drawn an overall picture of the characteristics of the communication windows between the equatorial thermocline and midlatitude subduction regions (Fine et al., 1987; Liu and Huang, 1998; Liu et al., 1994; Lu and McCreary, 1995; Lu et al., 1998; McPhaden and Fine, 1988; Rothstein et al., 1998). Depending upon the longitude at which subduction occurs, the anomaly advected within the lower branch of the STC can reach the equator via two distinct pathways. In the central North Pacific, the subducted water first flows southwestward to arrive at the western boundary and then turns southward toward the equator by the low latitude western boundary undercurrent (the western boundary pathway). In contrast, water subducted in the eastern subtropical basin first flows southwestward and then directly feeds into the EUC in the central-eastern equatorial Pacific (the interior pathway). Though many dynamical aspects of the two pathways have been well documented in previous literature, a comprehensive separation of the western boundary and interior pathways remains challenging. Up to now, most of the studies mainly employed virtual or Montgomery streamfunction evaluated on isopycnal surfaces to differentiate between the two pathways (Fukumori et al., 2004; Johnson and McPhaden, 1999; Li et al., 2012). In addition, the preferential pathway that the subducted anomaly takes to reach the equator as well as the relative contribution of Northern versus Southern Hemisphere western boundary and interior pathways remain unclear. In the North Pacific, there is a barrier associated with the high potential vorticity induced by positive Ekman pumping in the northeastern Pacific, which inhibits the direct communication of



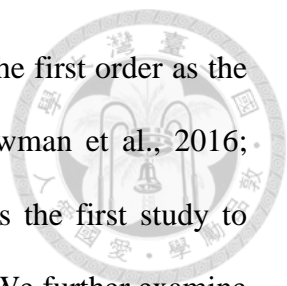
lower-layer water from the subtropics to the tropics. Therefore, the anomaly has to flow through a more convoluted route to reach the equator (Johnson and McPhaden, 1999; Lu et al., 1998; Rothstein et al., 1998) or almost flows toward the western boundary to join the EUC (Fukumori et al., 2004; Furue et al., 2015; Lu and McCreary, 1995). Furthermore, a considerable amount of North Pacific ventilated thermocline water heads into the Indian Ocean via the Indonesian Throughflow which strongly reduces the exchange flux of subtropical water to the western equatorial region (Lee et al., 2002; Nie et al., 2016; Rodgers et al., 1999). In the South Pacific, however, due to the absence of such a high potential vorticity barrier, the anomaly can take a direct pathway toward the equator in the interior ocean (Luo et al., 2003; Luo and Yamagata, 2001). As a result, the South Pacific contributes significantly more subtropical water to the tropics than the North Pacific does via the interior pathway (Fukumori et al., 2004; Goodman et al., 2005; Johnson and McPhaden, 1999). Also, as the distance coverage of the anomaly in the South Pacific along the interior pathway is much shorter than its Northern counterpart, the impact of the South Pacific subtropical anomaly on the tropical climate variability appears to be of greater magnitude and shorter lead time (Kolodziejczyk and Gaillard, 2012; Kuntz and Schrag, 2018; Luo et al., 2005; O'Kane et al., 2014; Tatebe et al., 2013; Yang et al., 2005; Zeller et al., 2021).

One appealing question is whether the advection of remotely generated spiciness anomaly by the mean current can effectively migrate to the equator and impact tropical climate variability. Modeling (Fukumori et al., 2004; Giese et al., 2002; Pierce et al., 2000; Schneider, 2000; Schneider et al., 1999b; Yeager and Large, 2004), as well as observational studies (Schneider et al., 1999a; Zhang & Liu, 1999), have obtained ambiguous conclusions regarding such propagating signal from the extratropical subduction zone in both



hemispheres. On the one hand, some studies demonstrated that the magnitude of spiciness anomaly diminishes significantly during the propagation (Kolodziejczyk and Gaillard, 2012; Liu and Shin, 1999; Sasaki et al., 2010) and likely cannot arrive in the western equatorial Pacific (Hazeleger et al., 2001; Schneider et al., 1999a). On the other hand, some studies found that the spiciness anomaly can spread to the equator via the interior pathway (Li et al., 2012; Luo et al., 2005) and/or the western boundary pathway (Kolodziejczyk and Gaillard, 2012; Luo et al., 2005; Sasaki et al., 2010; Yeager and Large, 2004) but at much-reduced amplitude. Moreover, the relative contribution of the mean advection of spiciness anomaly along the interior pathway versus the western boundary pathway at each hemisphere to the low-frequency signal peak in the equator is subject to event dependence. Employing an ocean general circulation model combined with a Lagrangian particle simulator forced with climatological surface conditions, Zeller et al. (2021) showed one positive event peak in the subsurface equator is mainly contributed by Southern Hemisphere water traveling along the interior pathway while another negative event peak is primarily caused by water traveling via the western boundary pathway in the Northern Hemisphere. Although many efforts have been made in the role of extratropical signals on the interannual to decadal tropical climate variability, a thorough understanding regarding the surface forcing of subsurface spiciness anomaly (SSA) as well as the dominant physical processes responsible for the formation of isopycnal spiciness anomalies in the North Pacific is still unclear.

In this study, a low-frequency subsurface spiciness propagating mode in the North Pacific is characterized and linked with the Aleutian Low/PDO by employing two different observational datasets. The Aleutian Low is the dominant sea level pressure (SLP) pattern in the North Pacific primarily driven by internal atmospheric dynamics (Alexander et al., 2010;



Pierce, 2001) while the PDO (Mantua et al., 1997) can be regarded as the first order as the oceanic expression of the high-frequency atmospheric variability (Newman et al., 2016; Schneider and Cornuelle, 2005). To the best of our knowledge, this is the first study to investigate the relationship between SSAs and the Aleutian Low/PDO. We further examine the physical processes responsible for isopycnal spiciness variability in the midlatitude and subtropics, respectively. We find that the net surface heat flux (Q_{net}) and wind stress curl anomalies associated with the Aleutian Low/PDO create SSAs via subduction and spice injection mechanisms. In addition, flow pattern change related to the interaction between the Aleutian Low and PDO generates SSAs through the anomalous advection across the mean spiciness gradient mechanism. This paper is organized as follows. Section 2 describes the data and the method utilized. Section 3 presents the main result of the study followed by discussion and concluding remarks in Section 4 and Section 5, respectively.

2.2 Data and methodology

For the ocean subsurface temperature and salinity, we use the latest EN.4.2.2 in the ‘EN’ series of data sets from the Met Office Hadley Centre (Good et al., 2013), 1° horizontal grids over 42 non-uniform spaced depth levels spanning from 1900 to present at monthly intervals. Four ensemble members are available in EN.4.2.2. EN.4.2.2.analysis.g10 (hereinafter referred to as EN422) is chosen for our analysis while the results extracted from the other three ensembles are qualitatively consistent and similar. All available sources of oceanographic measurements are adopted in this product, primarily from the WOD09. In addition, the gridded Grid Point Value of the Monthly Objective Analysis (MOAA GPV) (Hosoda et al., 2008) is also used to compare the evolution of subsurface anomalies during 2001-2019. The MOAA GPV is constructed mainly from Argo floats in combination with

buoy measurements and casts of research cruises. The horizontal resolution is 1° on standard pressure levels between 10 and 2000 dbar. For the sea surface height, we use the Global Ocean Data Assimilation System (GODAS) with 0.33° latitude \times 1° longitude during 1980-2019 (Behringer et al., 1998; Behringer and Xue, 2004). In addition, the SLP, SST, and 10-m wind data from the ERA5 are used (Hersbach et al., 2020). To be consistent with atmospheric data, our analysis uses the period of 1979 to 2019 except for MOAA GPV which is analyzed from 2001 to 2019.

The temperature and salinity are first converted to conservative temperature and absolute salinity based on the TEOS-10 (McDougall and Barker, 2011) before calculating spiciness following the method proposed by Jackett and McDougall (1985) and McDougall and Krzysik (2015):

$$\int_{\rho^\ominus} d\pi = 2 \int_{\rho^\ominus} \left. \frac{\partial \rho^\ominus}{\partial S_A} \right|_{\Theta, p_r} dS_A \quad (1)$$

$$\pi_0(S_A, \Theta) = \pi_u \sum_{j=0}^6 \sum_{k=0}^6 A_{jk} s^j y^k \quad (2)$$

$$\pi_1(S_A, \Theta) = \pi_u \sum_{j=0}^6 \sum_{k=0}^6 B_{jk} s^j y^k \quad (3)$$

$$\pi_2(S_A, \Theta) = \pi_u \sum_{j=0}^6 \sum_{k=0}^6 C_{jk} s^j y^k \quad (4)$$

where π is spiciness, Θ is conservative temperature, S_A is absolute salinity, ρ is potential density and p_r is reference pressure. π_0 , π_1 and π_2 are spiciness referenced to 0 dbar, 1000 dbar, and 2000 dbar, respectively. $\pi_u \equiv 1 \text{ kg m}^{-3}$, $S_{A_u} \equiv (40 \times 35.16504 \text{ g kg}^{-1}) / 35$ and $\Theta_u = 40^\circ\text{C}$. The nondimensional salinity s and nondimensional temperature y are

$$s \equiv \sqrt{\frac{S_A + 24 \text{ g kg}^{-1}}{S_{A_u}}} \text{ and } y \equiv \frac{\Theta}{\Theta_u}$$

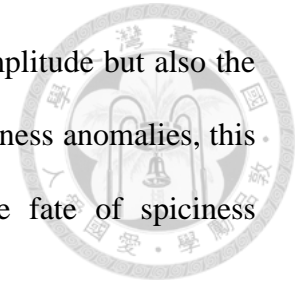


A_{jk} , B_{jk} , and C_{jk} are the coefficients of the polynomials for spiciness (see McDougall and Krzysik (2015) for more details). The spiciness in the pressure coordinates is then transformed to sigma coordinates by linear interpolation on the isopycnals $\sigma_\theta = 25\text{-}26 \text{ kg m}^{-3}$ with $\Delta\sigma_\theta = 0.01 \text{ kg m}^{-3}$. The chosen isopycnal level is within the main thermocline (Figure S2.1). It can capture a larger portion of the formation of spiciness signal than that typically defined using $25\text{-}25.5 \sigma_\theta$ (not shown), and thus tracking water mass from the source generation region to the tropics more appropriately. To remove the impacts of the annual cycle, the interpolated data are filtered with a 13-month running mean. We also analyze the spiciness based on the definition of Huang et al. (2018). The results are qualitatively similar despite some small differences in the magnitude of the anomalies.

To account for the pathway connecting extratropics with the tropics, we calculate the mean acceleration potential, referenced to 2000 dbar (McDougall and Klocker, 2010). It is then interpolated to sigma coordinates and low-pass filtered with a 13-month running mean. In this study, the interior and western boundary pathways are not explicitly separated. Here, we define the North Pacific Pathway (hereinafter referred to as NPP) as the passage between the acceleration potential contours of 19.7 and 21 $\text{m}^2 \text{ s}^{-2}$ which covers a large portion of extratropical-tropical exchange window to describe the propagation features.

The temporal and spatial characteristics of low-frequency spiciness variability are investigated using a complex empirical orthogonal functions (CEOF) analysis (Barnett, 1983; Horel, 1984) performed in the North Pacific ($0\text{-}60^\circ\text{N}$, $120^\circ\text{E}\text{-}80^\circ\text{W}$). The advantage of CEOF over traditional empirical orthogonal function (EOF) analysis lies in its ability to

extract propagating properties in the data by providing not only the amplitude but also the potential phase change. Given the propagative nature of isopycnal spiciness anomalies, this method can reveal important propagation properties relating to the fate of spiciness variability (see Text S1 for the details).



2.3 Results

2.3.1 Characteristics of low-frequency spiciness variability

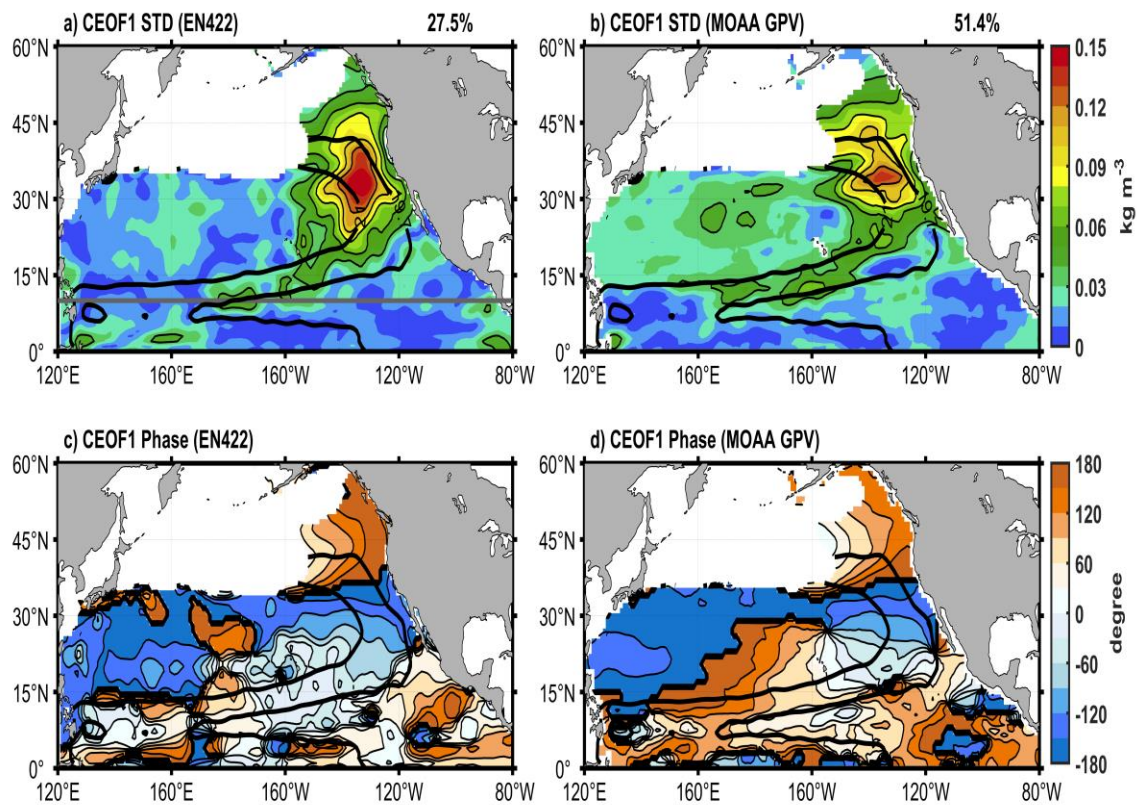
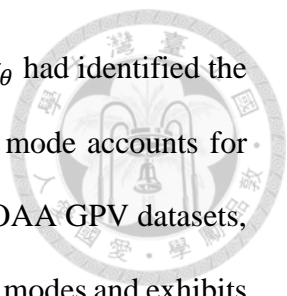


Figure 2.1 Standard deviation of low-frequency spiciness variability averaged between $25\text{-}26\sigma_\theta$ in the North Pacific associated with CEOF1. The variance explained by CEOF1 is shown in (a) for EN422 and (b) for MOAA GPV, respectively. The spatial phase of the leading mode derived from (c) EN422 and (d) MOAA GPV. The thick black lines denote the mean acceleration potential contours of $19.7\text{-}21.0\text{ m}^2\text{s}^{-2}$ (NPP). The gray line in (a) indicates the latitude of 10°N .



The CEOF analysis of spiciness anomalies averaged between 25-26 σ_θ had identified the dominant mode of low-frequency variability in the North Pacific. This mode accounts for about 28% and 51% of the total spiciness variance in the EN422 and MOAA GPV datasets, respectively (Figure 2.1a, b). It is significantly distinguished from the rest modes and exhibits the most prominent propagating feature (Figures 2.1c, d, and 2.2). Therefore, we focus entirely on the first CEOF mode (CEO1) in this study. The spatial amplitude of CEO1 is similar between the EN422 and MOAA GPV although the latter shows a weaker magnitude in the eastern midlatitude (Figure 2.1a, b). In general, CEO1 exhibits maximum variability equatorward from the outcropping area, centering at 38°N, 140°W. The associated magnitude reaches 0.12 kg m⁻³ in the center of action but decreases considerably downstream along the NPP as indicated by the acceleration potential contours of 19.7 and 21 m² s⁻². This area of maximum spiciness variability is consistent with that identified by Li et al. (2012) based on the potential temperature averaged between 25-25.5 σ_θ from the MOAA GPV dataset. While CEO1 of the present study possesses only one center of maximum variability in the extratropics, Li et al. (2012) showed the other secondary variability in the eastern subtropical region around 20°N east of 130°W. Compared to the CEO1 of interannual salinity anomalies evaluated on the $\sigma_\theta=25.5$ surface of Kolodziejczyk and Gaillard (2012), the spiciness signal in the present study is much more coherent and stronger, and the center of action expands further northward to about 50°N (Figure 2.1a, b). These differences may be ascribed to the isopycnal levels as well as the thermodynamic variable employed for the analysis. The two previous studies mainly evaluate the anomalies between $\sigma_\theta=25-25.5$ which are shallower than the isopycnal levels considered here.

A propagating signal can be seen from the increasing spatial phase of CEOF1 along the NPP (Figure 2.1c, d). This propagating feature is further demonstrated by the reconstruction of the first CEOF mode from -180° to 180° at 45° phase intervals (Figure S2.2). The abrupt zonal change of phase around 38°N coincides with the large variance of the first mode. At lower latitudes, the phase structure is strongly modulated by the turn to the eastern edge of the pathway where the potential vorticity barrier (Lu and McCreary, 1995) hinders the direct equatorward transport from the extratropics to the tropics. Though the spatial phase along the NPP is qualitatively similar between the two products poleward of 20°N , significant differences can be observed downstream. While the MOAA GPV shows a smoother phase transition, the EN422 experiences a significant phase change which is probably due to the decadal changes in the propagating characteristics. These will be further shown next.

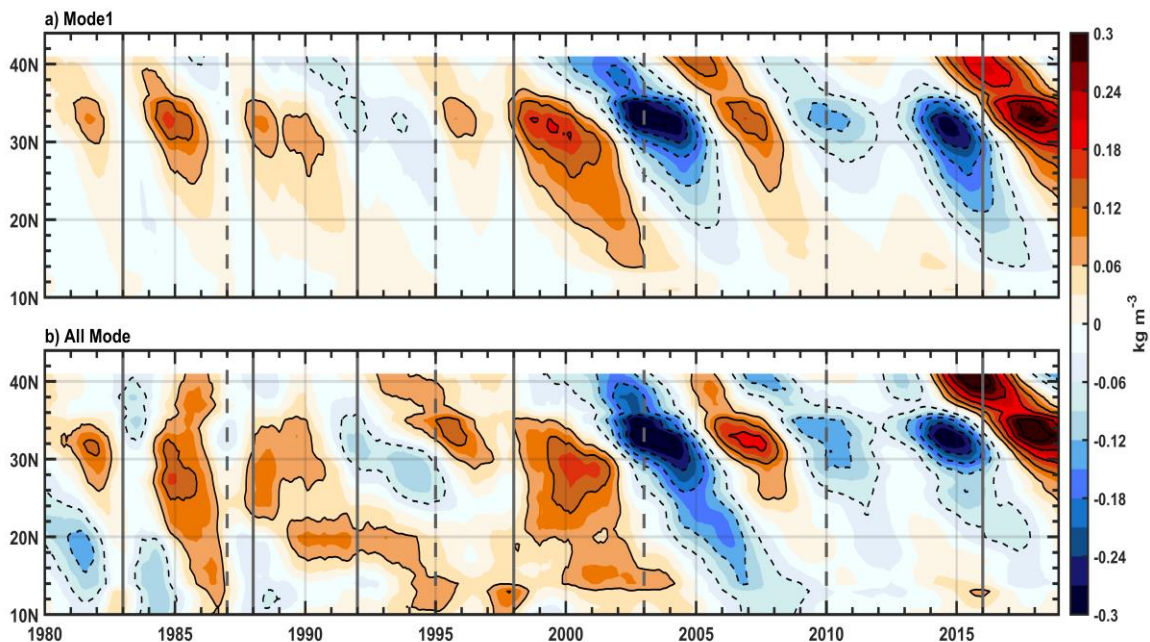
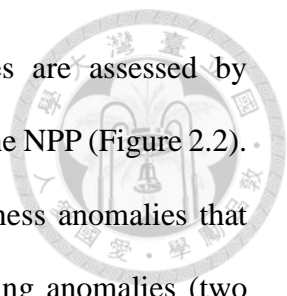


Figure 2.2 Latitude-time diagram of reconstructed spiciness anomalies using the (a) first and (b) all CEOF modes averaged along the NPP based on EN422. The vertical solid (dashed) gray lines represent strong and very strong (moderate) El Niño events that peak in January based on the Oceanic Niño Index (ONI).



The propagating characteristics of the first and all CEOF modes are assessed by reconstructing the spiciness anomalies on the Hovmöller diagram along the NPP (Figure 2.2). During 1980-2018, there were episodes of positive and negative spiciness anomalies that occurred in the extratropical North Pacific (Figure 2.2a). The alternating anomalies (two negative and one positive) during 2003-2011 have previously been reported (Kolodziejczyk and Gaillard, 2012; Li et al., 2012; Sasaki et al., 2010) (Figure 2.2). In addition, two major spiciness events of opposite signs emerged from 2012 onwards: one negative anomaly appeared in 2012-2013 and the other positive anomaly originated in 2014-2015. Our results suggest that considering deeper isopycnal levels can characterize the spiciness occurrence (variability) from the high latitude region at least one to two years in advance compared to the previous studies.

The reconstructed spiciness anomalies using CEOF1 show a clear pattern of equatorward propagation with the strongest variability observed poleward of 24°N , consistent with the spatial amplitude distribution (Figures 2.1a, b and 2.2a). For a positive spiciness anomaly centering at 35°N , 130°W (-180° , Figure S2.2), it propagates westward and equatorward along the NPP, corresponding with the increasing phase (Figures S2.2 and 2.3). The magnitude is then gradually reduced (-45° to 180° , Figures S2.2 and 2.2). In addition, a negative spiciness anomaly formed in the midlatitude North Pacific centering at 40°N , 150°W subsequently follows the pathway that the positive takes to reach the tropics (-135° , Figures S2.2 and 2.2). As a result, the equatorward propagation of prominent spiciness anomalies from 40°N to 10°N lasts for about seven years (Figures 2.2a and S2.2) which is consistent with the temporal phase change (Figure 2.3). This time scale is in good agreement with the estimated 7-8 years for the extratropical origin of subsurface signals to reach the

tropics (Kolodziejczyk and Gaillard, 2012; Schneider et al., 1999a). Our study also reveals that the propagating signals along the NPP can reach 10°N, especially after 1998/1999 (Figure 2.2). The more equatorward arrival of spiciness anomalies after 1998/1999 on the one hand may result from the decadal change of the intertropical convergence zone. In particular, the width of the intertropical convergence zone has narrowed in recent decades as a response to climate change (Byrne et al., 2018) thus weakening the potential vorticity barrier in the lower layer (Lu and McCreary, 1995) to facilitate the equatorward propagation of extratropical signals. On the other hand, the quality-poor data pre-Argo period (before 2001) might contribute to the discrepant signal before and after 1998/1999.

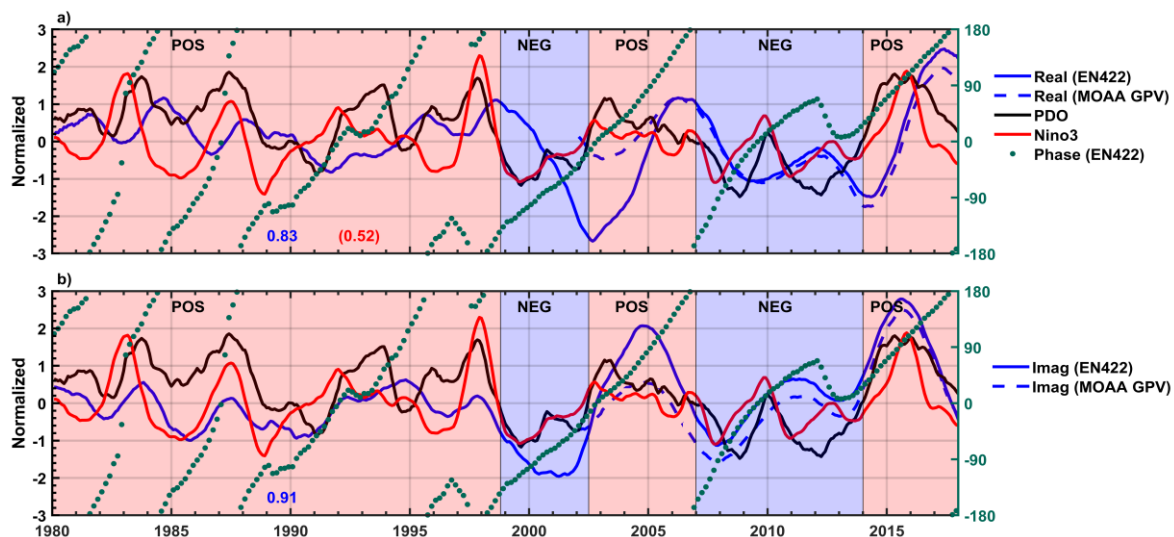


Figure 2.3 Normalized time series of (a) real and (b) imaginary expansion coefficients of CEOF1. The associated temporal phase (in degree) of the CEOF1 is shown as green dots. The black and red lines are the PDO index from the NOAA Physical Sciences Laboratory and Niño3 (5°S-5°N, 150°-90°W) index obtained from the NOAA Climate Prediction Center, respectively. The blue number in (a) is the simultaneous correlation between PC1 (real) of spiciness anomalies derived from MOAA GPV and EN422 during the same period (2002-2018) and similarly, the number in (b) is the correlation obtained from the first imaginary part of the two datasets. The second red number in (a) is the simultaneous correlation between the PDO and the Niño3. POS and NEG correspond to PDO positive and negative phases.

There is a substantial difference between the spiciness signals before and after 1998/1999 (Figure 2.2), a period when the North Pacific SST and the relevant atmospheric conditions

changed abruptly (Lyon et al., 2014), which is often referred to as climate regime shift occurring after the winter of 1998/1999. This shift has resulted in shorter persistence of the PDO cold/warm phases since 1998/1999 compared to the prolonged warm condition before the regime shift (Figure 2.3). For comparison, the temporal evolution of the first principal component (PC1) of spiciness anomalies is shown in Figure 2.3. While the imaginary component almost varies in tandem with the PDO index, there is a time lag between the peak of the real part with the peak of the PDO in which the latter leads the former longer than a year. The in-phase relation can be further confirmed by the strong correlation when PDO leads PC1 (real) of spiciness anomalies by 18-24 months (Figure 2.4a), suggesting the relevance between the two leading modes of surface and subsurface oceanic variability in the North Pacific (Figure 2.3). This will be elaborated more in the next section.

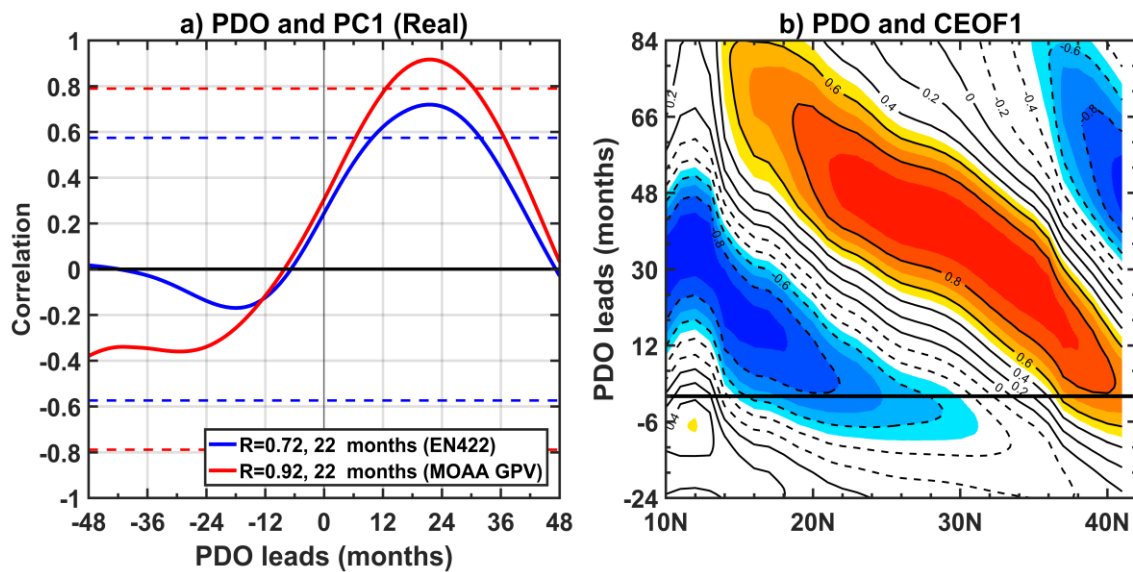
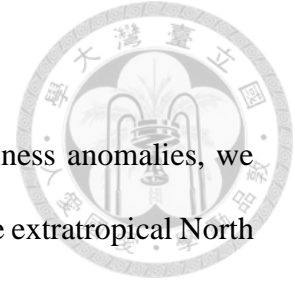


Figure 2.4 (a) Lead-lag correlation coefficients between the PC1 of spiciness anomalies and the PDO index. Horizontal dashed lines indicate the 95% confidence level. (b) Lead-lag correlation coefficients between the PDO index and reconstructed spiciness anomalies using CEOF1 averaged along the NPP. Shading indicates correlation coefficients that are significant at the 95% confidence level (Student's t-test). The thick black line in (b) indicates lag 0. Positive lags indicate PDO leads the spiciness anomalies.



2.3.2 Forcing mechanism

Motivated by the linkage between PDO and the PC1 (real) of spiciness anomalies, we further investigate the role of PDO in forcing subsurface variability in the extratropical North Pacific. All of the following analyses will be based on the long-term EN422 data set unless noted otherwise. Defined as the leading EOF of monthly SST anomalies (SSTA) poleward of 20°N (Mantua et al., 1997), the spatial pattern of the positive PDO phase is characterized by a positive anomaly extending from the high latitude toward the equator along the west coast of North America combining a negative anomaly in the western-central Pacific (Figure S2.3a). As the SLP and 10-m wind vector anomalies are regressed onto the PDO index, an intense cyclonic circulation corresponding with the strengthening of the Aleutian Low can be found in the North Pacific (Figure S2.3b). In addition, the interannual variability of the Aleutian Low (defined as the principal component of leading EOF of interannual SLP anomalies between 20°-60°N, 120°E-80°W) is strongly correlated with PDO, reaching a simultaneous correlation of 0.63 and as high as 0.68 when Aleutian Low leads the PDO for three months (Figure S2.3c). This result is consistent with previous studies (Newman et al., 2016; Schneider and Cornuelle, 2005).

Comparing the spatial structure of CEOF1 (Figure 2.1a, b) and the PDO pattern (Figure S2.3a) accompanied by its atmospheric forcing (Figure S2.3b), we find that the region of maximum spiciness variability coincides with the south-eastward extension of positive temperature anomaly below the center of Aleutian Low. As the SSTA are regressed onto the PC1 of spiciness anomalies (shading in Figure S2.4), the resulting pattern is similar to the positive phase of the PDO. The role of the PDO forcing is further confirmed by the lead-lag correlation between the PDO index and the PC1 (real) of spiciness anomalies (Figure 2.4a).

As expected, the highest correlation obtained when the PDO leads the spiciness anomalies by 22 months. This characteristic is not only present in the short-term but also in the long-term datasets with very high correlations, 0.92 and 0.72 for MOAA GPV and EN422, respectively. In addition, at negative lag months, the PC1s do not possess any significant correlations with the PDO index. These further demonstrate that PDO actively forces the spiciness anomalies while the latter responds passively.

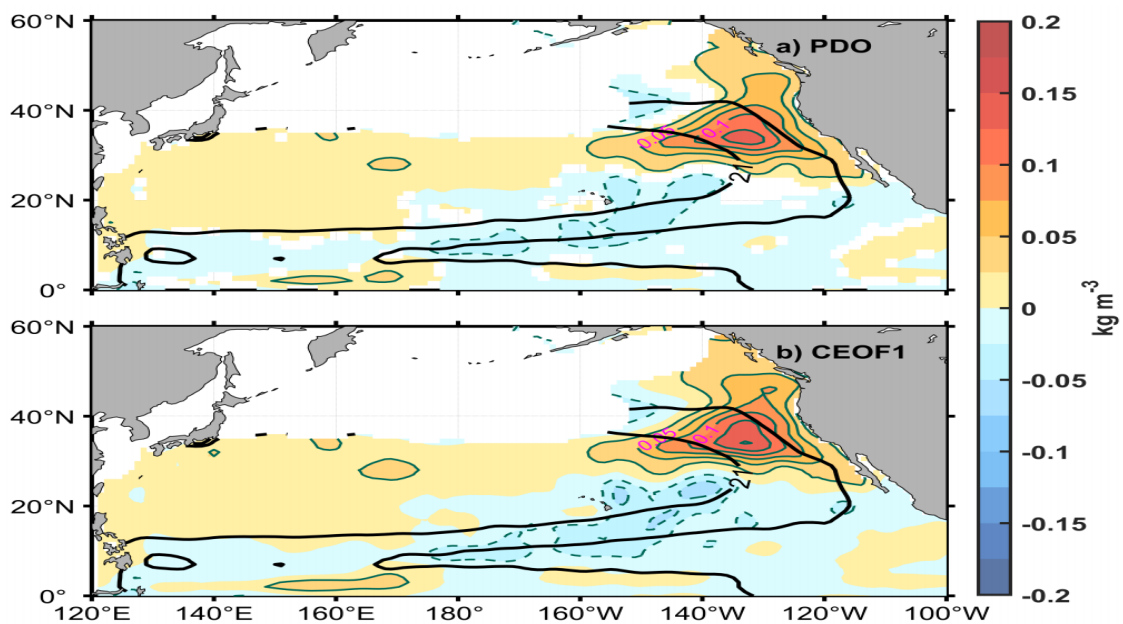


Figure 2.5 (a) Reconstructed spiciness anomalies using CEOF1 regressed with the PDO index at lag 22 months (shading and green contours, only regressed values significant at the 95% confidence level according to a Student's t-test are shown). The contour interval is 0.025 kg m^{-3} and the solid (dashed) contours denote positive (negative) anomalies. (b) Spatial structure of the corresponding CEOF1 (real). The thick black lines represent the defined NPP.

To demonstrate the role of the PDO forcing, we regress the reconstructed spiciness anomalies using the CEOF1 with the PDO index at a lag of 22 months (the highest correlation between the PDO and the associated PC1) in Figure 2.5a. The spatial pattern of CEOF1 associated with the real part is also presented in Figure 2.5b. The strongest positive variability

in the eastern midlatitude is largely explained by the PDO forcing. In addition, there is another region of negative anomaly associated with the PDO forcing that centers on 20°N, 145°W. The defined NPP almost lies in the region of spiciness variability explained by the PDO forcing and, thus can be employed to depict the propagation of spiciness anomalies from the source region toward the tropics.

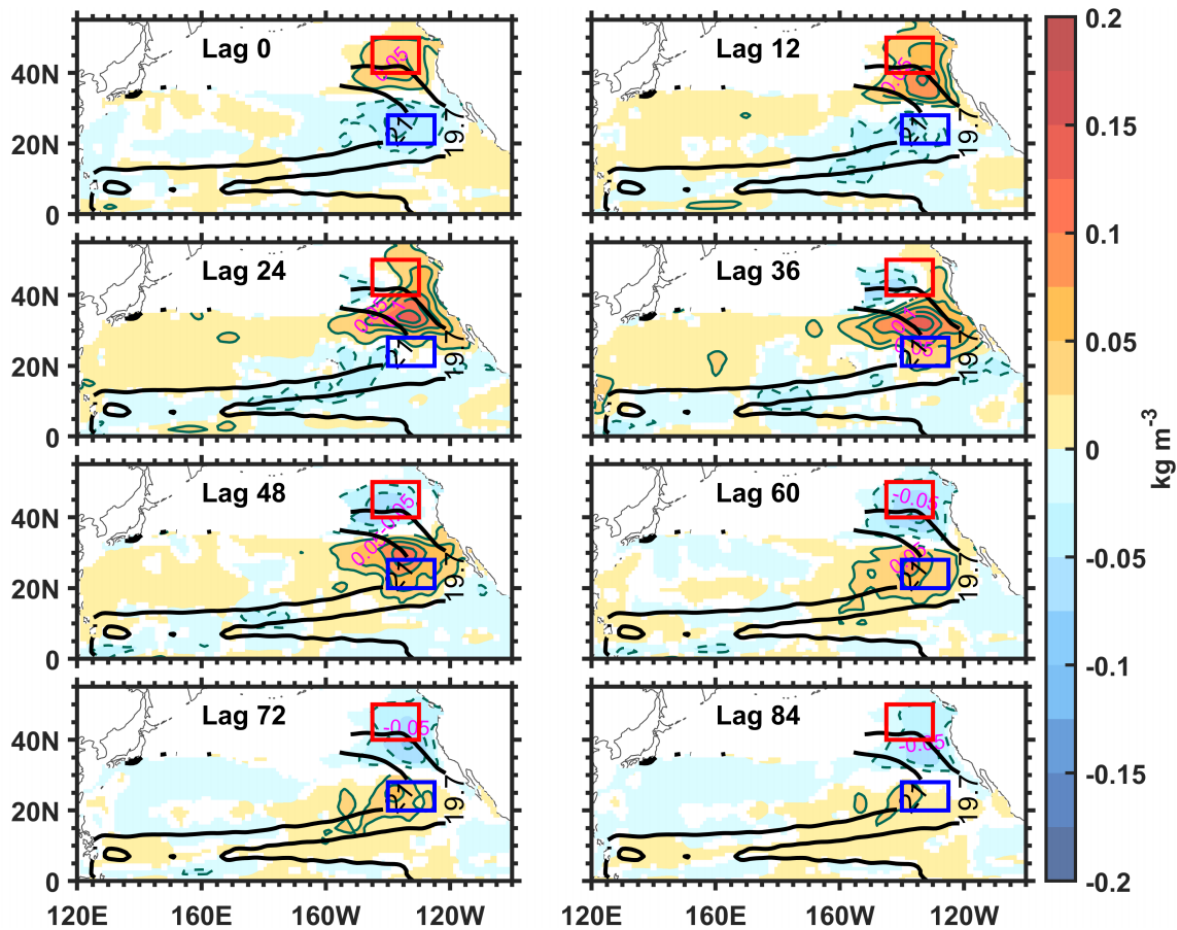
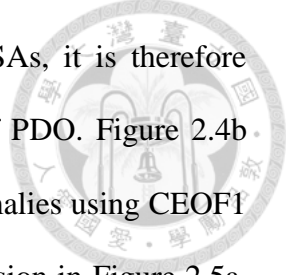


Figure 2.6 Reconstructed spiciness anomalies using CEOF1 regressed with the PDO index from lag 0 to lag 84 months (shading and green contours, only regressed values significant at the 95% confidence level according to a Student's t-test are shown). The contour interval is 0.025 kg m^{-3} and the solid (dashed) contours denote positive (negative) anomalies. The red and blue boxes represent the midlatitude ($40\text{-}50^\circ\text{N}$, $145\text{-}130^\circ\text{W}$) and subtropical ($20\text{-}28^\circ\text{N}$, $140\text{-}125^\circ\text{W}$) regions, respectively. The thick black lines show the NPP. Positive lags indicate PDO leads the spiciness anomalies.



Having established a strong relationship between the PDO and SSAs, it is therefore interesting to see how the spiciness signals evolve after the forcing of PDO. Figure 2.4b shows the lead-lag correlation between the reconstructed spiciness anomalies using CEOF1 averaged along the NPP and the PDO index. Consistent with the regression in Figure 2.5a, the derived lag correlation shows an equatorward evolving positive (negative) pattern that originates from the midlatitude (subtropics). The robustness of the PDO in forcing subsurface spiciness propagating mode can reach approximately 14°N after seven years (positive anomaly). The negative anomaly that formed in the eastern subtropics can propagate further equatorward, reaching 10°N roughly after three years.

The equatorward subsurface propagation is hypothesized to play a key role in modulating tropical climate variability at decadal time scales (Gu and Philander, 1997; Schneider, 2000). We further examine the PDO-forced propagating characteristic of the subsurface by regressing the reconstructed spiciness anomalies using CEOF1 with the PDO index from no lag (lag 0) to seven years later (Figure 2.6). A simultaneous dipole pattern of spiciness variability is formed associated with the PDO forcing at no lag: positive in the midlatitude centering at 40°N , 135°W and negative in subtropics centering at 25°N , 130°W . Afterward, the two anomalous signals propagate equatorward along the NPP. The positive spiciness anomaly not only propagates downstream but also strengthens until four years later (lag 48). It then weakens subsequently and continues to propagate until reaching 14°N after seven years (lag 84). The other negative anomaly formed in the eastern subtropical Pacific can also be observed three years later (lag 36) around 10°N with a much stronger magnitude than the above positive anomaly arriving at 14°N . In addition, another negative anomaly (centers at 40°N , 150°W) is formed alternatively in the midlatitude around two years later (lag 24). It

then gradually amplifies (Stephens et al., 2001) and follows a similar pathway to the positive one to approach the tropics (see also Figures 2.2a and S2.2). This in turn could create a decadal cycle of equatorward ventilation, similar to the hypothesis of Gu and Philander (1997). Further analysis of the power spectrum of the PC1 (real) confirms the robustness of this propagating mode as there is a significant peak within the 8- to 16-year periods, similar to the spectral peak of the PDO (Figure 2.7a, b).

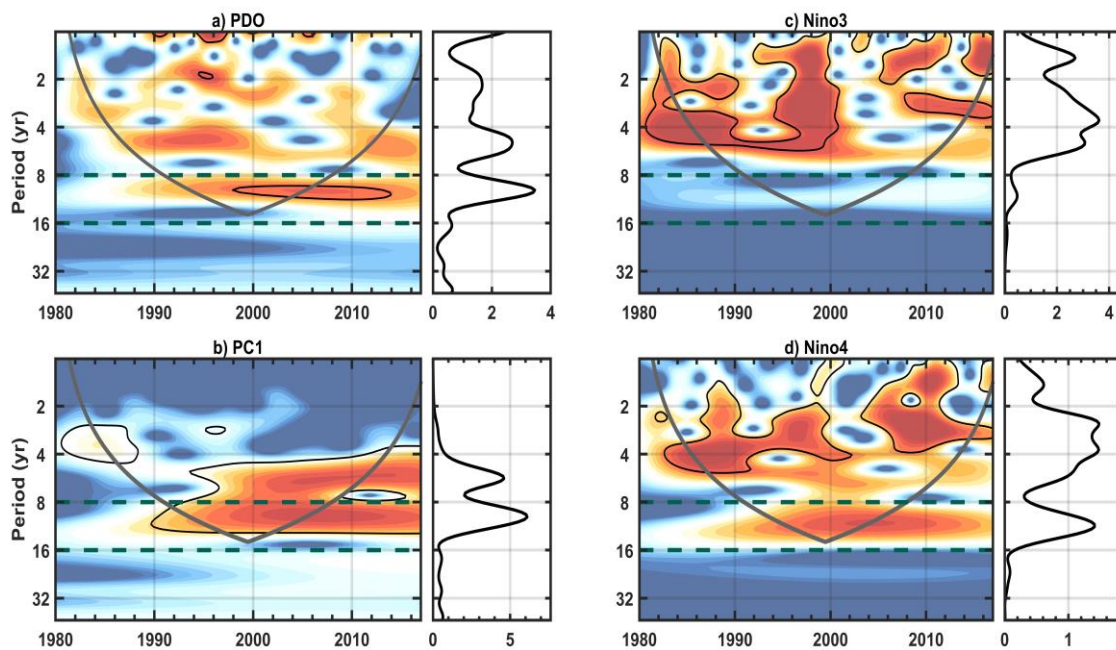
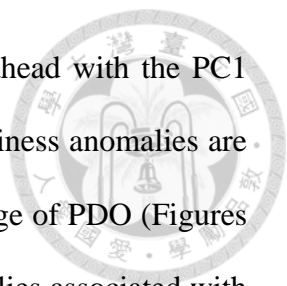


Figure 2.7 Bias-rectified wavelet power spectra and corresponding global wavelet spectra of (a) PDO, (b) PC1 (real), (c) Niño3, and (d) Niño4 (5°S-5°N, 160°E-150°W). Thin black contours indicate statistically significant at the 95% confidence level when tested against a first-order autoregressive model null hypothesis. The parabola regions indicate the “cone of influence” where edge effects become important. The horizontal dashed green lines indicate the 8- and 16-year periods. All the data are analyzed from 1980 to 2018.

The above analysis has identified the role of PDO in forcing SSAs in both midlatitude and subtropical North Pacific. In addition, the Aleutian Low has been demonstrated as a primary driver of the PDO (Figure S2.3). We further investigate the connection between SSAs and the dominant atmospheric forcing of the PDO. Figure 2.8 shows the regression of SLP, 10-



m wind vector, and Q_{net} (positive downward) anomalies 22 months ahead with the PC1 (real) of spiciness anomalies. As expected, the midlatitude positive spiciness anomalies are associated with the strengthening of the Aleutian Low through the change of PDO (Figures 2.5a and 2.8a). Previous studies suggested that the cyclonic wind anomalies associated with the intensified Aleutian Low produce downward heat flux anomalies along the west coast of North America (Yu and Kim, 2011), consistent with the band of positive Q_{net} in the eastern midlatitude in Figure 2.8b. This pattern is coincident with the positive SSAs in Figure 2.5. Therefore, our results confirm the strengthening (weakening) of the Aleutian Low drives a positive (negative) Q_{net} anomaly in the eastern midlatitude, forcing the corresponding positive (negative) SSAs.

2.3.3 Formation of isopycnal spiciness anomalies

The generation of SSAs in the eastern extratropical South Pacific can be quantified in terms of both subduction (Nonaka and Sasaki, 2007) and injection (Kolodziejczyk and Gaillard, 2012; Wang and Luo, 2020; Yeager and Large, 2004). However, the formation of isopycnal spiciness anomalies in the eastern subtropical North Pacific (25-33°N, 150-135°W) can only be ascribed in part to the injection during boreal winter (Katsura, 2018). In contrast, subduction is proposed for isopycnal temperature variability in the central midlatitude North Pacific (Schneider et al., 1999a). As a result, whether the subduction or spice injection can explain the anomalies observed along the isopycnals of 25-26 kg m⁻³ is still unclear.

The PDO-forced subsurface variability results in a dipole pattern of spiciness anomalies in the midlatitude and subtropics. This suggests that different physical processes are involved in the formation of SSAs. Therefore, we investigate the positive signal in the midlatitude (the

red box, Figure 2.6) and the negative signal in the subtropics (the blue box, Figure 2.6) separately to identify the governing generation mechanisms in the two regions.

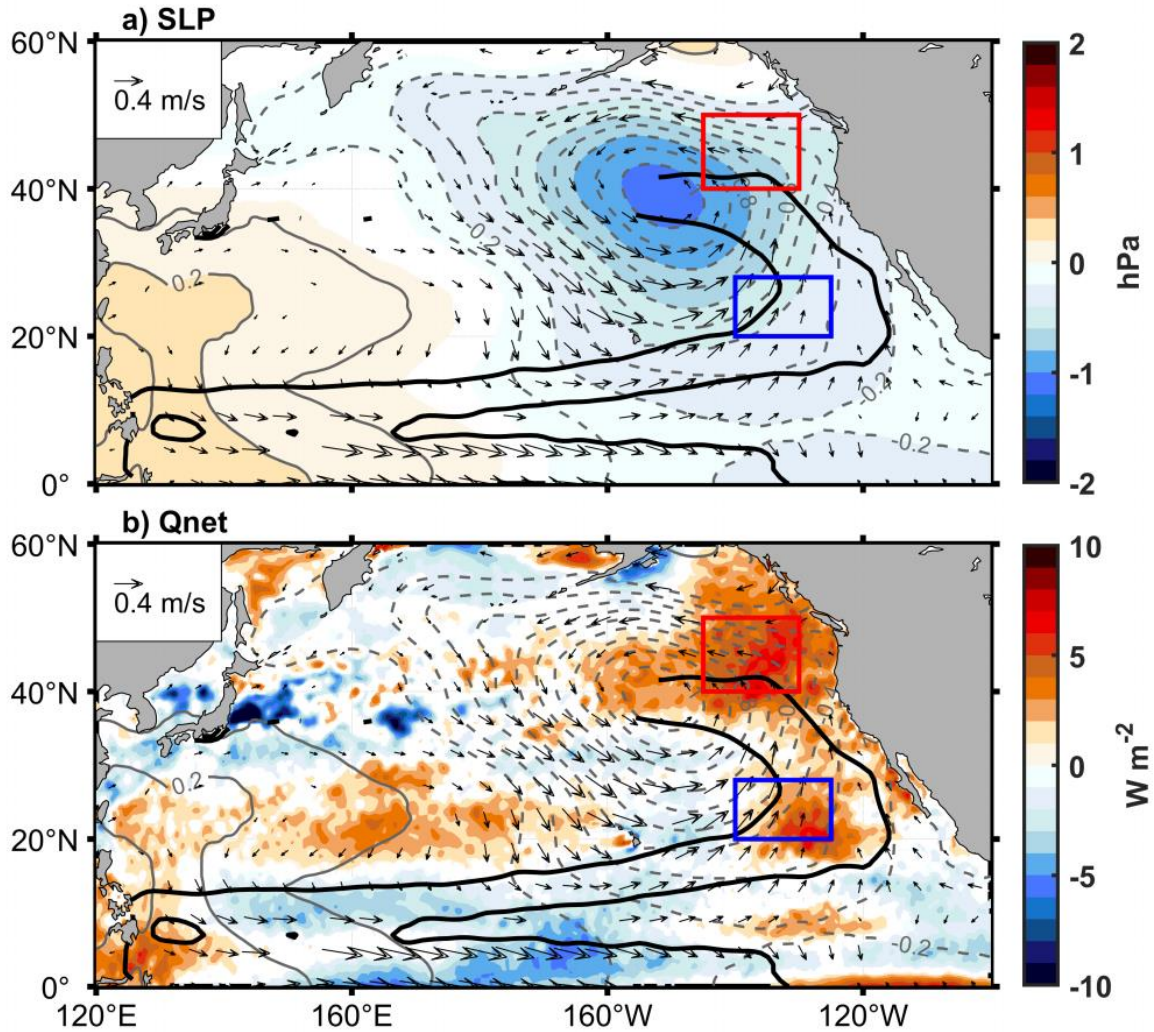
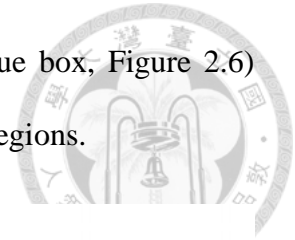
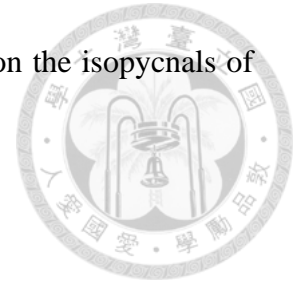


Figure 2.8 (a) SLP (shading and gray contours) and (b) Qnet (shading) anomalies 22 months ahead regressed with the PC1 of spiciness anomalies. Wind vectors at 10 m regressed with the PC1 are also imposed. Regressed values significant at the 95% confidence level (Student's t-test) are shaded for SLP and Qnet anomalies. Only regressed wind vectors significant at the 95% confidence level are shown. The red and blue boxes are described in **Figure 2.6**. The thick black lines represent the NPP.

In general, subsurface spiciness evolution can be determined by the combined vertical variations of temperature and salinity. In addition, surface oceanic conditions favor the formation of SSAs (Nonaka and Sasaki, 2007). By combining these features, we can verify

whether the subduction or spice injection is relevant to the anomalies on the isopycnals of $25\text{-}26 \text{ kg m}^{-3}$.



a. Midlatitude

Spiciness variability between $25\text{-}26 \sigma_\theta$ largely follows the pattern of temperature anomalies at around $50\text{-}120 \text{ m}$, demonstrating the key role of temperature in regulating SSAs (Figure 2.9a, c). Salinity anomalies, however, enhance (weaken) the isopycnal spiciness variability when having the same (opposite) sign with temperature anomalies and are most pronounced below 100 m (Figure 2.9b, c). While interior temperature variability can generally be traced to the surface of outcrop, the salinity anomalies between $50\text{-}120 \text{ m}$ are disconnected from surface variability, suggesting different dynamics are involved in the generation of anomalous signals associated with the two variables. Interior salinity variability in the region might relate to the propagation of subsurface salinity anomalies originating in the Gulf of Alaska (Pozo Buil and Di Lorenzo, 2015).

To characterize the contribution of subduction versus spice injection in the midlatitude, Figure 2.10 shows the maps of the isopycnal $\sigma_\theta=25$ outcrop position and the standard deviation of spiciness anomalies averaged between $25\text{-}26 \sigma_\theta$ in March. Because the mean isopycnal depth is shallow in the region (Figure S2.1), $\sigma_\theta=25$ is exposed to the surface and its annual wintertime outcrop position is largely located at the southern edge or even outside the red box (Figure 2.10a). In addition, the mean outcrop line is located at the area associated with the large standard deviation of late winter isopycnal spiciness variability while the extreme outcrop line extends further equatorward to the northern edge of the blue box (Figure 2.10b). Therefore, subduction is expected to play a significant role in the formation of SSAs in the midlatitude.

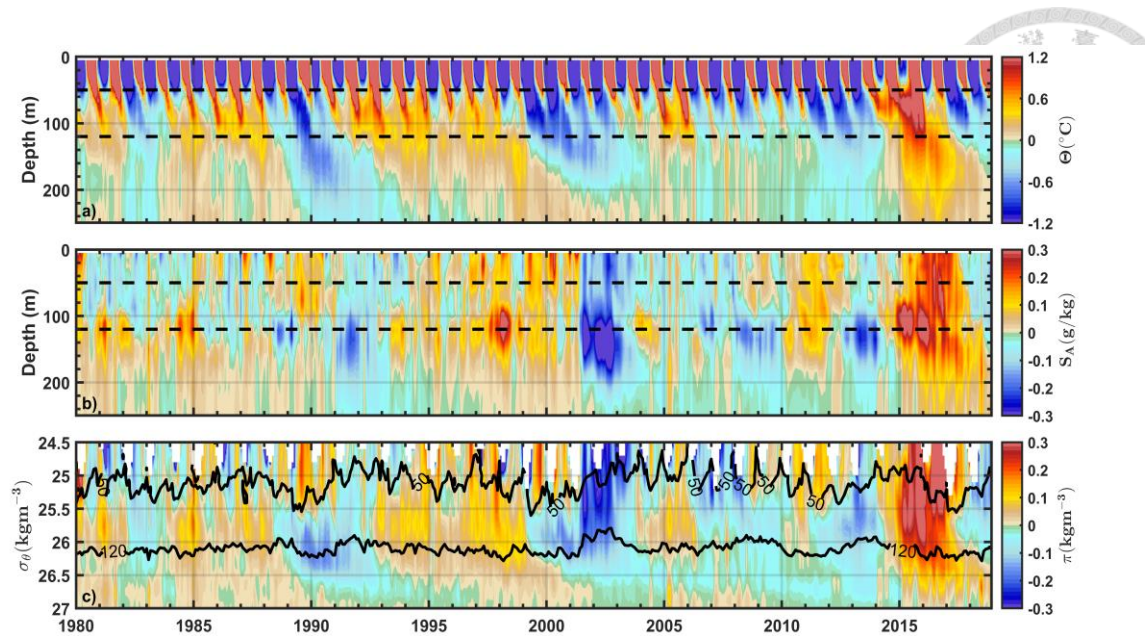


Figure 2.9 Time-depth plot of (a) conservative temperature and (b) absolute salinity anomalies averaged in 40-50°N, 145-130°W (the red box in **Figure 2.6**). (c) Time- σ_θ plot of spiciness anomalies averaged over the same region and period as (a) and (b). The horizontal dashed back lines in (a) and (b) indicate the depth of 50- and 120 m. The thick black lines in (c) show the isopycnal depth of 50- and 120 m. Anomalies are calculated relative to the mean from 1980 to 2018.

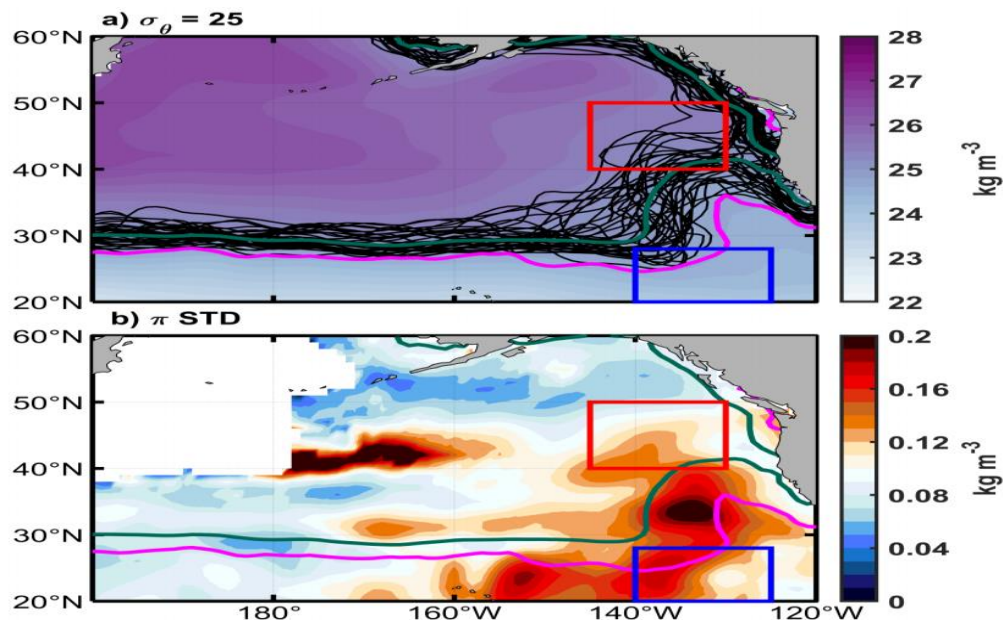


Figure 2.10 (a) Annual mean outcrop position of $\sigma_\theta=25$ surface (thin black contours) and (b) standard deviation of spiciness anomalies averaged between 25-26 σ_θ in March. Superimposed in (a) is mean March sea surface density during 1980-2018 (shading). In all panels, the thick green and magenta contours denote the mean and extreme equatorward outcrop position of $\sigma_\theta=25$ in March, respectively. The red and blue boxes are the regions defined in **Figure 2.6**.

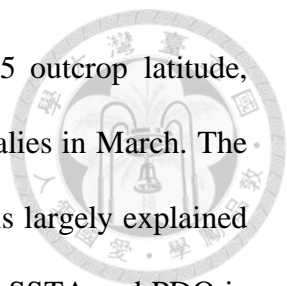


Figure 2.11 shows the temporal evolution of the isopycnal $\sigma_{\theta}=25$ outcrop latitude, spiciness anomalies averaged between $\sigma_{\theta}=25$ -26, SSTA and SSS anomalies in March. The $\sigma_{\theta}=25$ displaces meridionally from its mean position of 35.5°N which is largely explained by the variation of SSTA associated with PDO (the correlation between SSTA and PDO is 0.75, significance at 99% level). The temporal evolution of isopycnal spiciness anomalies almost tracks the variability of SSTA but some out-of-phase variations do occur. This suggests that a variety of surface forcing might play different roles in the formation of SSAs. To examine how subduction generates SSAs, two representative years are selected for example, in 2015 when the sea surface was warm and the outcrop line migrated poleward, and in 2017 when the sea surface was cold and the outcrop line migrated equatorward. The corresponding spatial distribution of SSTA, SSS anomalies, and the $\sigma_{\theta}=25$ outcrop position is shown in Figure 2.12. In 2015, surface oceanic variability was characterized by strong positive temperature anomalies and relatively weak SSS anomalies (Figure 2.12a, c). The warm SSTA caused the isopycnal $\sigma_{\theta}=25$ to migrate poleward from its mean position, forming the positive spiciness anomalies (Figure 2.11a). In this case of “purely” subduction, isopycnal spiciness anomalies have the same sign as SSTA. In 2017, the anomalously cold SSTA caused the isopycnal $\sigma_{\theta}=25$ to migrate equatorward from its mean position. Supposedly, negative SSAs were expected but positive signals were found (Figure 2.11a). This is because the strong positive SSS anomalies have compensated for the impact of negative SSTA to form positive SSAs as demonstrated by Nonaka and Sasaki (2007). In general, when the wintertime PDO-related SSTA dominate over salinity, the subduction generates isopycnal spiciness anomalies that mainly exhibit SSTA signature. In contrast,

when there is strong meridional compensation between SSTA and SSS anomalies, the resulting isopycnal anomalies vary out of phase with the SSTA.

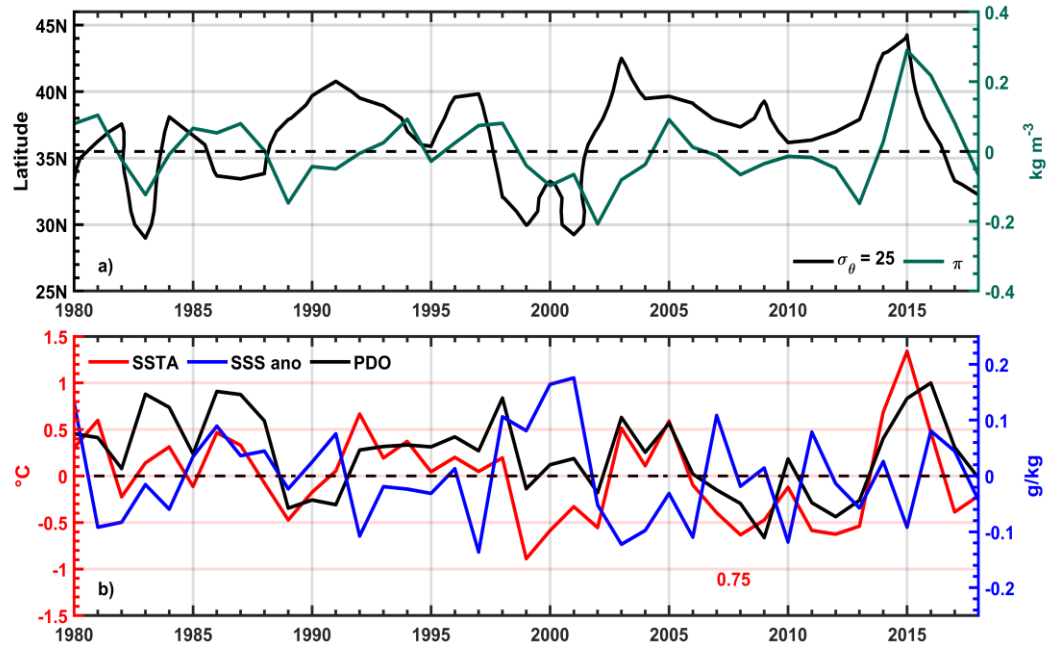


Figure 2.11 (a) Time series of the March outcrop latitude of $\sigma_{\theta}=25$ averaged from 145° to 130°W (black) and the areal mean (the red box) of spiciness anomalies averaged between 25-26 σ_{θ} (green). The mean outcrop latitude of $\sigma_{\theta}=25$ is shown by the dashed black line. (b) Time series of the areal mean (35-60°N, 150-115°W) SSTA (red) and SSS anomalies (blue). Superimposed is March PDO index (black). The red number is the simultaneous correlation between SSTA and PDO.

However, subduction alone cannot fully explain SSAs in the midlatitude North Pacific. The prolonged periods of warm temperature anomalies at around 60-140 m such as during 1991-1995, 1996-1997, 2005-2006, and 2014-2016 are associated with the persistence of temperature anomalies via the reemergence mechanism (Alexander and Deser, 1995), which reinforces the subsurface signals to the following winter (Figure S2.5a) and form positive spiciness anomalies between 25-26 σ_{θ} (Figure 2.9a, c). The persistence of negative temperature anomalies in 1999 hindered the downward penetration of positive surface signal in the following winter which in turn induced negative isopycnal spiciness anomalies during

1999-2001. The formation of SSAs in the midlatitude is also consistent with the large reemergence area in the North Pacific (Figure 1a in Murata et al. 2020). Therefore, subduction and reemergence are responsible for midlatitude isopycnal spiciness variability.

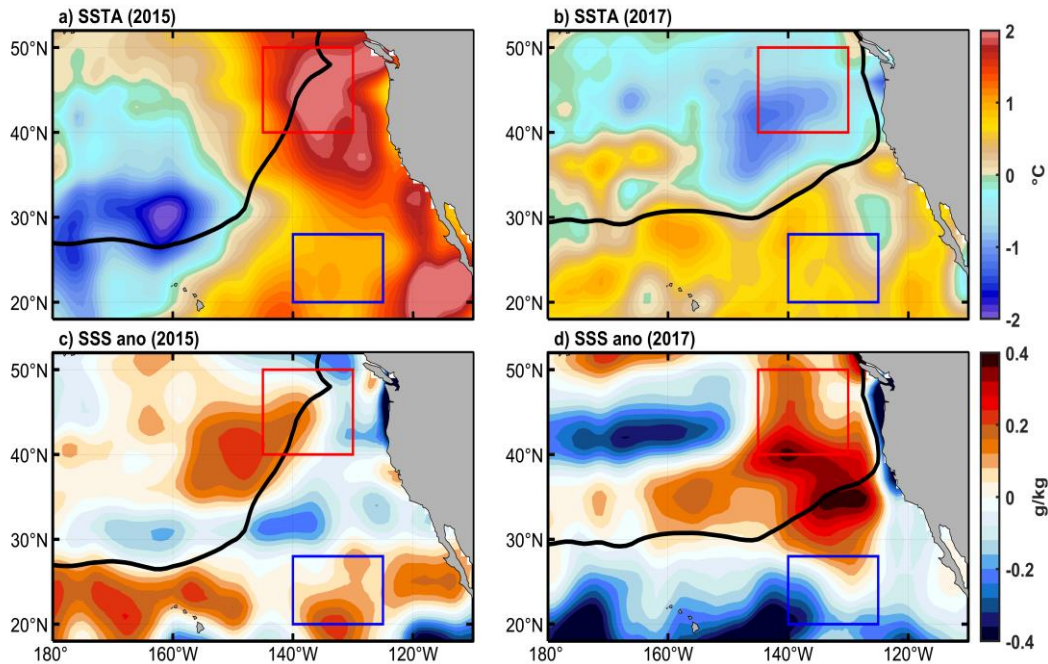
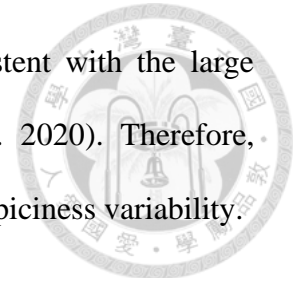


Figure 2.12 Monthly mean (top) SSTA and (bottom) SSS anomalies in (left) 2015 and (right) 2017 March. The thick black contours show the corresponding outcrop position of $\sigma_{\theta}=25$. The red and blue boxes are the regions defined in **Figure 2.6**.

b. Subtropics

As the isopycnal surface $\sigma_{\theta}=25$ outcrops in the northern edge of the blue box (Figure 2.10), subduction plays a role in the formation of SSAs in the subtropics. This can be further verified by the persistent penetration of surface temperature anomalies to the interior ocean (Figure 2.13a). However, the interannual variability of SSAs in the subtropics greatly follows the variation of salinity anomalies (Figure 2.13b, c). For example, in 1990 observed positive spiciness anomaly between $\sigma_{\theta}=25$ -26 kg m⁻³ was in tandem with positive salinity anomaly at around 120-250 m while temperature showed an opposite signature. Due to the critical role

of salinity in SSAs (Yeager and Large, 2004), injection is expected to play a role in the formation of spiciness anomalies in the region. During the winter of 1988, a pulse of greater than normal salinity detrained the interior ocean, and thus formed subsurface warm/salty anomalies. The penetration of fresher than normal pulse of salinity from the surface down to around 200 m in 1997 can also explain a large fraction of negative spiciness anomaly in the isopycnal surfaces 25-25.5 σ_θ . Therefore, spice injection contributes considerably to isopycnal spiciness variability in the subtropical North Pacific.

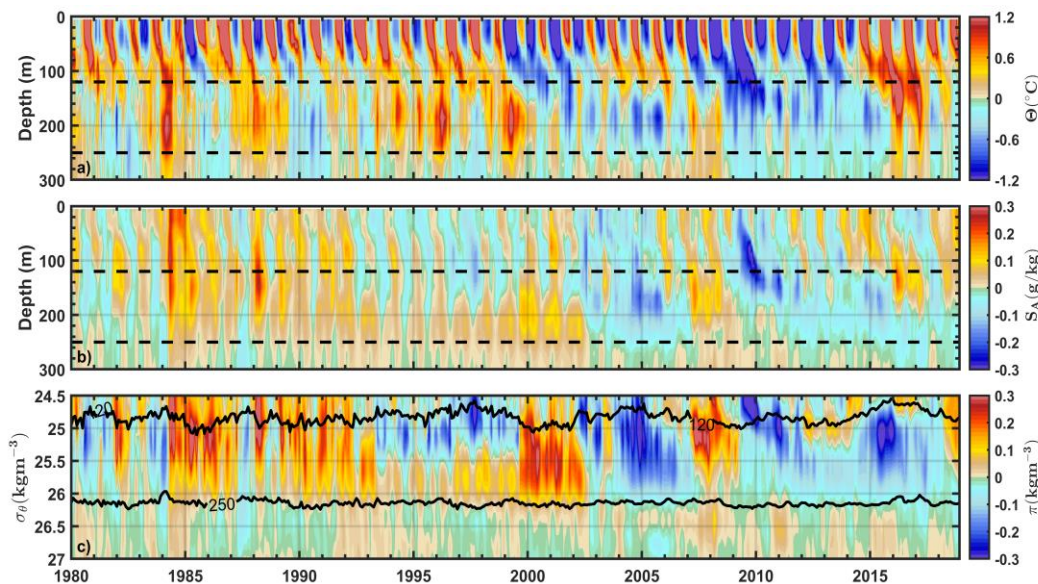


Figure 2.13 Same as **Figure 2.9** but in the region 20-28°N, 140-125°W (the blue box in **Figure 2.6**). The horizontal dashed back lines in (a) and (b) indicate the depth of 120- and 250 m. The thick black lines in (c) show the isopycnal depth of 120- and 250 m.

As spice injection is associated with the deepening or shoaling of wintertime mixed layer depth (MLD) (Kolodziejczyk and Gaillard, 2013; Wang and Luo, 2020), following Wade et al. (2011) and Wang and Luo (2020), we show in Figure S2.6a the lead-lag correlation between MLD and Ekman pumping, friction velocity, freshwater flux and Qnet anomalies. Here the MLD is determined by the use of 0.2°C as the temperature threshold (de Boyer

Montégut et al., 2004). Figure S2.6a suggests that Qnet and Ekman velocity are the two dominant contributors to MLD changes. These two factors are also closely related to PDO forcing (Figure S2.6b). As a result, Qnet and wind stress curl anomalies associated with Aleutian low/PDO induce MLD changes to generate SSAs via the spice injection mechanism (Figure S2.6). Our result is also consistent with the findings of Katsura (2018).

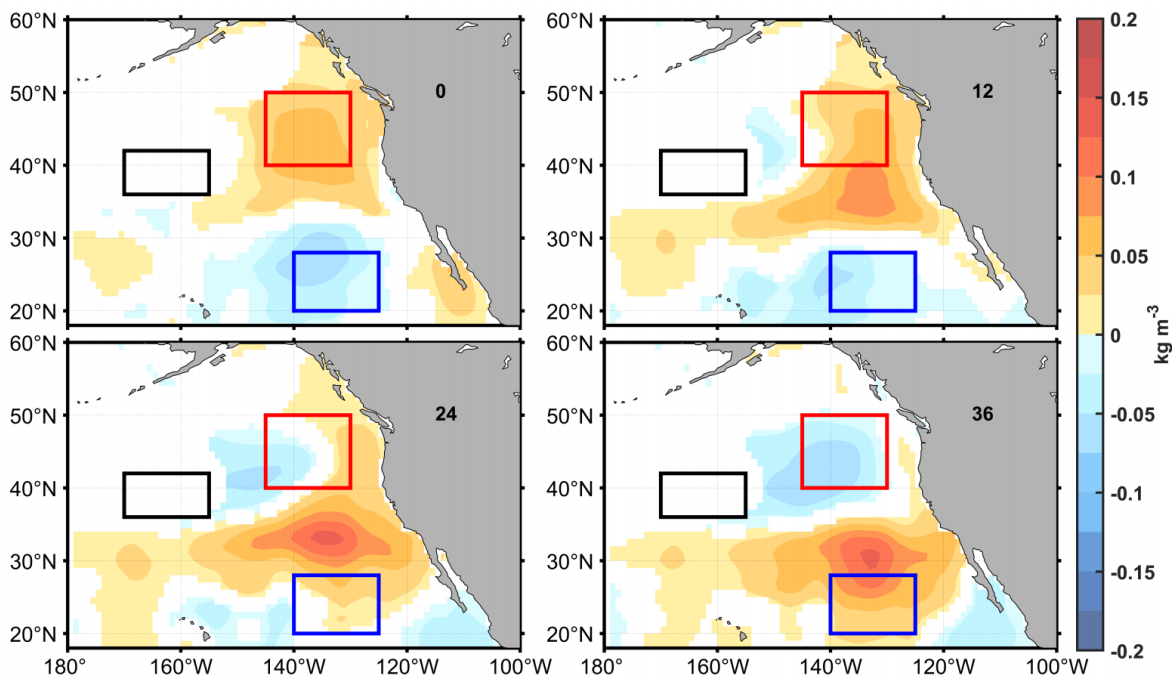
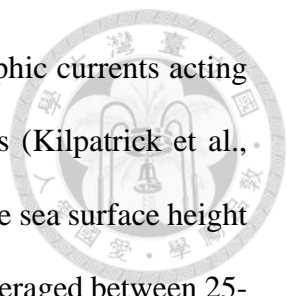


Figure 2.14 Spiciness anomalies averaged between 25-26 σ_θ regressed with the areal mean (black box) sea surface height anomalies from lag 0 to lag 36 months (only regressed values significant at the 95% confidence level according to a Student's t-test are shown). The red and blue boxes are the regions defined in **Figure 2.6**. Positive lags indicate sea surface height leads.

However, a considerable fraction of salinity variation leading to SSAs is not traceable to the surface, suggesting that other processes than subduction and spice injection are involved in the generation of isopycnal spiciness anomalies. For example, the positive salinity anomaly in 1993 was observed at a depth below 150 m which is completely disconnected from the anomaly above (Figure 2.13b). This vertical discontinuity can also be found during 1996-2002 and 2014-2017. These years coincide with the phase change of the PDO and

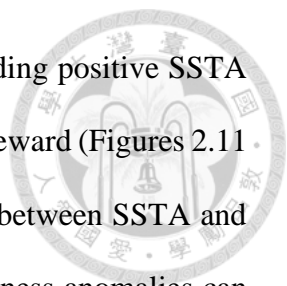


strong El Niño events (Figure 2.3) that can generate anomalous geostrophic currents acting against mean spiciness gradients to form isopycnal spiciness anomalies (Kilpatrick et al., 2011; Schneider, 2000). Following Kilpatrick et al. (2011), we regress the sea surface height anomalies averaged in 36-42°N, 170-155°W with spiciness anomalies averaged between 25-26 σ_θ at various time lags. Figure 2.14 reveals that a large fraction of subsurface spiciness variability in the blue box is associated with the anomalous advection across the mean spiciness gradient, consistent with the finding of Kilpatrick et al. (2011). Therefore, variability of the flow pattern associated with the Aleutian Low/PDO contributes significantly to the formation of isopycnal spiciness anomalies in the subtropical region (Figures S2.7 and S2.8).

2.4 Discussion

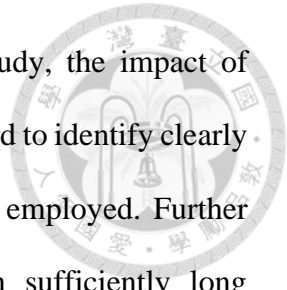
The SSAs between 25-26 σ_θ can enhance significantly within the first four years of their downstream propagation (lags 12-48, Figure 2.6). This equatorward amplification is associated with the geostrophic currents acting against the mean spiciness gradient (Figure 2.14), consistent with the study of Kilpatrick et al. (2011) who has demonstrated that the gradients between alongshore and offshore (black box in Figure 2.14) pressure anomalies account for the largest fraction of low-frequency spiciness variability below the red box (region of signal amplification). In addition, the sea surface height variability in the North Pacific (Figure S2.8) is primarily linked with Qnet (Figure S2.9) and wind stress curl anomalies (Figure S2.10) as a result of the interaction between the Aleutian Low and PDO (Fang and Yang, 2016; Luo et al., 2020).

Generally, the boreal winter atmospheric and surface oceanic forcings lead to the formation of SSAs in the North Pacific. In the eastern midlatitude, the strengthening of the



Aleutian Low drives positive Q_{net} anomalies that induce the corresponding positive SSTA (Figures S2.9 and 2.12). The sea surface density then migrates further poleward (Figures 2.11 and 2.12). Depending upon the degree of the meridional compensation between SSTA and SSS anomalies (Nonaka and Sasaki, 2007), the resulting isopycnal spiciness anomalies can have the same or opposite sign with the SSTA (Figure 2.11). In addition, the winter-to-winter persistence of subsurface temperature signals also contributes to the formation of SSAs via the reemergence mechanism (Figure S2.5). In the eastern subtropics, subduction and spice injection contribute to isopycnal spiciness anomalies (Figures 2.10 and 2.13). The latter is associated with the deepening or shoaling of MLD due to Aleutian Low/PDO-induced Q_{net} and wind stress curl anomalies (Figure S2.6). Furthermore, the variability of the flow pattern as a result of the interaction between the Aleutian Low and PDO generates isopycnal spiciness anomalies in the two regions (Figure 2.14).

The spiciness is useful to track the water mass variation which can relate to the low-frequency ocean climate variability. For the SSA change of magnitude $\pm 0.03 \text{ kg m}^{-3}$ observed at 10°N (Figure 2.2a), the corresponding temperature and salinity anomalies can reach more than $\pm 0.1 \text{ }^\circ\text{C}$ and $\pm 0.02 \text{ g/kg}$, respectively (not shown). Thus, the emergence of extratropical origin of spiciness anomalies in the central-eastern equatorial Pacific is of great interest because of their key role in driving tropical climate variability (Gu and Philander, 1997; Schneider, 2000; Zeller et al., 2021). By artificially imposing continual interior perturbations in the western equatorial Pacific, Schneider (2004) showed that the arrival of spiciness signals can induce a modest coupled mode of ocean-atmosphere response in the tropics. The occurrences of subsurface warming during 2003-2005 and cooling during 2008-2010 in the equatorial central Pacific were hypothesized to initiate the weak 2004-2005 El Niño and



strong 2010-2011 La Niña events (Li et al., 2012). In the present study, the impact of extratropical spiciness anomalies on tropical climate variability is still hard to identify clearly due to the coarse resolution and relatively short record of the dataset employed. Further investigations that employ coupled general circulation models with sufficiently long integration are needed to quantify the degree of extratropical subsurface spiciness influence on tropical climate.

The emergence of subsurface signals in the off-equatorial Pacific, resulting from the SSAs through the NPP, is also hypothesized to act as an oceanic “precursor” triggering the onset of ENSO (Ding et al., 2015b). When these signals reach the subtropical and tropical boundary, the STC and tropical dynamics start to play a role (Chen et al., 2015). There are consistent warm anomalies observed equatorward of 10°N that precede those strong and very strong El Niño events for about one year (Figure 2.2). These positive anomalies in conjunction with the impact of the Victoria mode, defined as the second EOF of SSTA poleward of 20°N, may further initiate an anomalous signal of similar sign in the central-eastern equatorial Pacific which eventually leads to the development of ENSO (Ding et al., 2015b).

The interannual SST variability in the tropical Pacific can affect the extratropical SSAs through atmospheric teleconnection. The highest correlations of PC1 (real) with Niño3 and Niño4 indices are 0.48 (PC1 lags 22 months) and 0.61 (PC1 lags 28 months), respectively (Figure 2.15a). The regression maps of reconstructed spiciness anomalies using CEOF1 with the Niño3 (at lag 22 months) and Niño4 (at lag 28 months) SST indices account for a large fraction of the positive and negative subsurface signals in the midlatitude and subtropics, respectively (Figure S2.9), similar to the pattern associated with PDO forcing (Figure 2.5a).

The main difference between the PDO and tropical forcing is the negative anomaly centers at 40°N, 150°W that can only be explained by the former, confirming the primary role of extratropical air-sea interaction in driving the spiciness mode. In addition, the contribution of Niño4 has greater magnitudes than Niño3, consistent with the 21st century shift toward a more Central Pacific (here represented by Niño4) type of ENSO (Lee and McPhaden, 2010; McPhaden, 2012) (Figures 2.7c, d and 2.15b, c). These in turn can potentially generate a decadal climate oscillation in the North Pacific that involves both oceanic and atmospheric bridges.

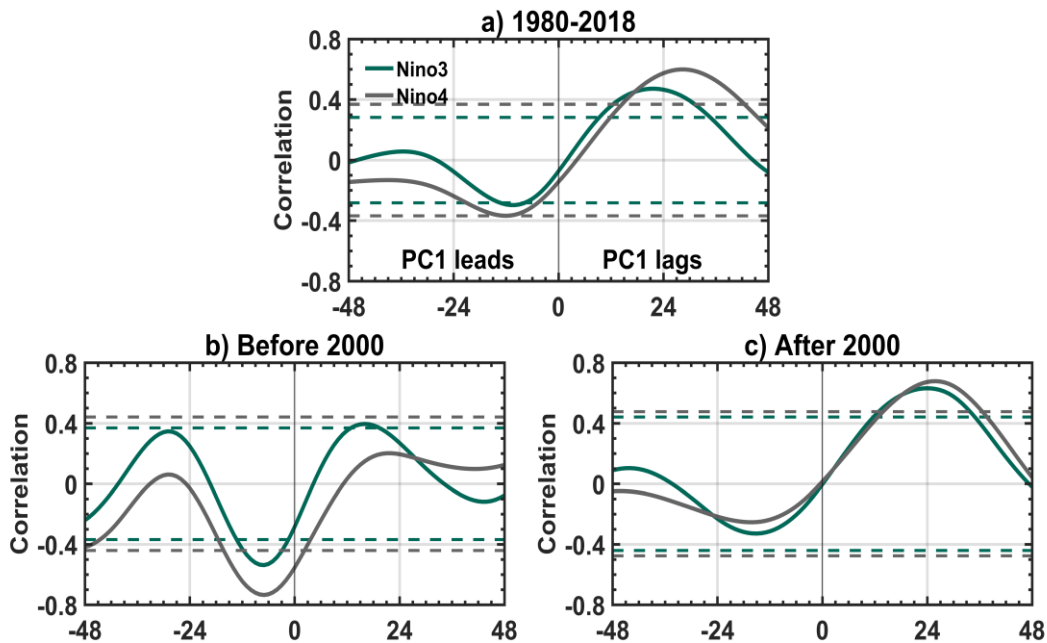
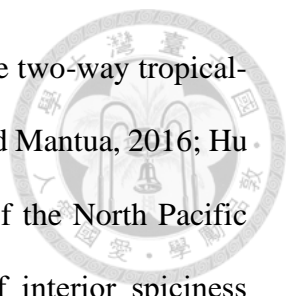


Figure 2.15 Lead-lag correlation coefficients between Niño SST indices and the PC1 of spiciness anomalies (a) during 1980-2018, (b) before 2000 and (c) after 2000. Horizontal dashed lines show the 95% confidence level. Positive lags indicate the Niño SST indices lead the PC1.

During the boreal winter of 2013-2015, prolonged near-surface warming was observed in the northeastern Pacific, termed the “Pacific warm blob” (Bond et al., 2015) or marine heat wave (Frölicher et al., 2018; Oliver et al., 2018; Smale et al., 2019). The occurrence of this extraordinary phenomenon has been connected with different physical processes such as the



coupling between the North Pacific Gyre Oscillation and PDO due to the two-way tropical-extratropical interactions via atmospheric teleconnection (Di Lorenzo and Mantua, 2016; Hu et al., 2017; Joh and Di Lorenzo, 2017), and an extended weakening of the North Pacific High (Amaya et al., 2020). The “warm blob” overlies the region of interior spiciness formation in the midlatitude (Figure 2.6). In 2013, positive surface temperature anomaly can penetrate as deep as 200 m (Hu et al., 2017) and precedes the positive surface salinity anomaly for around half a year (Figure 2.9a, b). However, variations of salinity and temperature are almost in phase below 80 m depth and these subsurface signals persist year-round until 2017. As a result, the strongest warm/salty anomaly is produced in the interior ocean (Figure 2.9c). Given the strong connection between the warm blob and PDO (Joh and Di Lorenzo, 2017), and future projection of the intensification of extreme Aleutian Low events (Giamalaki et al., 2021) as well as the increasing variance of PDO under greenhouse forcing (Di Lorenzo and Mantua, 2016), the longer and more frequent occurrence of marine heat waves (Frölicher et al., 2018; Oliver et al., 2018) could lead to greater subsurface spiciness variability and stronger impact on Pacific climate variability.

2.5 Conclusions

This study shows a strong connection between the PDO and subsurface spiciness variability in which during the positive (negative) phase of the PDO, a dipole pattern of positive (negative) and negative (positive) SSAs is formed in the midlatitude and subtropics, respectively (Figure 2.16). The resulting anomalies then propagate equatorward along the North Pacific pathway. The positive anomaly of midlatitude origin can reach 14°N after seven years of propagation while the negative anomaly of subtropical origin can arrive at 10°N after three years. In addition, a negative anomaly emerges in the midlatitude after the

occurrence of the positive signal two years later, then follows the pathway that the positive takes to reach the tropics. This ultimately leads to a decadal propagating mode of SSAs in the North Pacific. Further analysis demonstrates that the Aleutian Low, the primary driver of the PDO, is responsible for the formation of the dipole pattern by inducing net surface heat flux changes and anomalous subsurface currents.

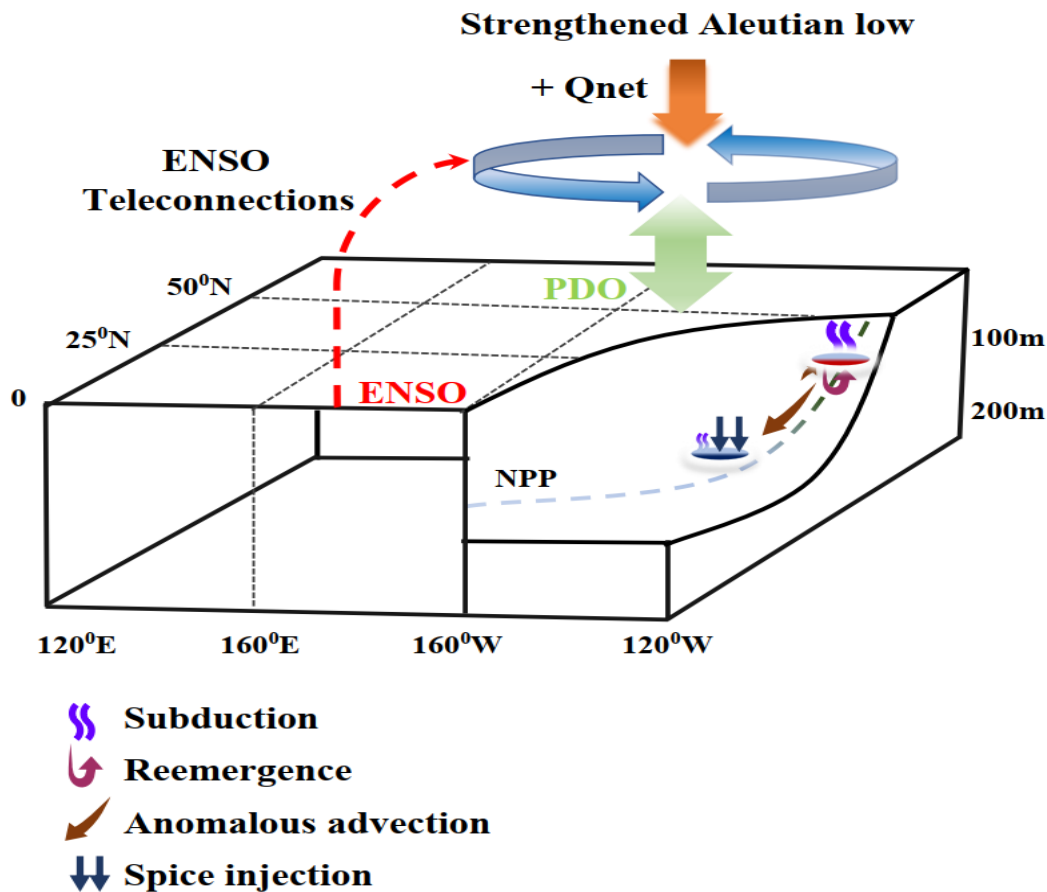
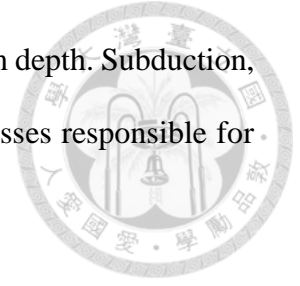


Figure 2.16 Schematic of decadal spiciness mode in the North Pacific. The solid red (dark blue) oval indicates positive (negative) spiciness anomalies in the midlatitude (subtropics).

In the eastern midlatitude North Pacific, isopycnal spiciness variability largely follows the pattern of temperature anomalies at around 50-120 m depth. Spiciness anomalies between 25-26 σ_θ are generated via the subduction, reemergence, and anomalous advection across mean spiciness gradients. In contrast, eastern subtropical isopycnal spiciness variability

generally follows the variation of salinity anomalies at around 120-250 m depth. Subduction, spice injection, and anomalous advection are the three governing processes responsible for subsurface spiciness variability in the region.



2.6 Supporting information

Text S1: CEOF

The complexification of an original scalar field $u_j(t)$ (where j denotes spatial position and t is time) is accomplished by adding its Hilbert transform $\hat{u}_j(t)$ as an artificial imaginary component

$$U_j(t) = u_j(t) + i\hat{u}_j(t)$$

The imaginary part of the complex observation $U_j(t)$ has the same amplitude as the original data field but the phase is advanced by $\pi/2$. In practice, \hat{u}_j is commonly obtained from the Fourier coefficients derived from fast Fourier transform (FFT) routines (Barnett, 1983). However, Hilbert transforms obtained from FFT are more strongly influenced by end effects than are the Fourier transforms themselves (Horel, 1984). Therefore, each end of the time series should be cosine-tapered to eliminate this problem before any further analysis.

The rest of the CEOF procedure is similar to the traditional EOF analysis except that the statistics are performed on the complex time series. The eigenvalues λ_n and eigenvectors $B_n(x)$ obtained, where n denotes mode number and x represents spatial dependence, are real for the former and complex for the latter, respectively. Accordingly, the complex time-dependent principal components are given by

$$A_n(t) = \sum_{j=1}^N U_j(t) B_n(x)$$

The corresponding EOF representation of complex time series can then be expressed as

$$U_j(t) = \sum_{n=1}^N A_n(t) B_n^*(x)$$

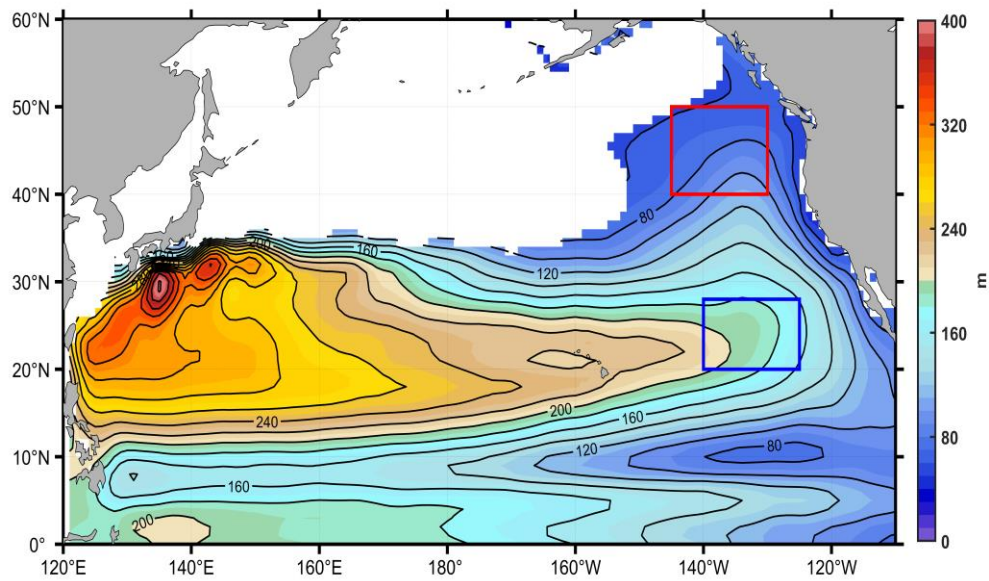


Figure S2.1 Mean depth of the 25-26 σ_θ from 1980 to 2018 (EN422). The contour interval is 20 m. The red and blue boxes are described in **Figure 2.6**.

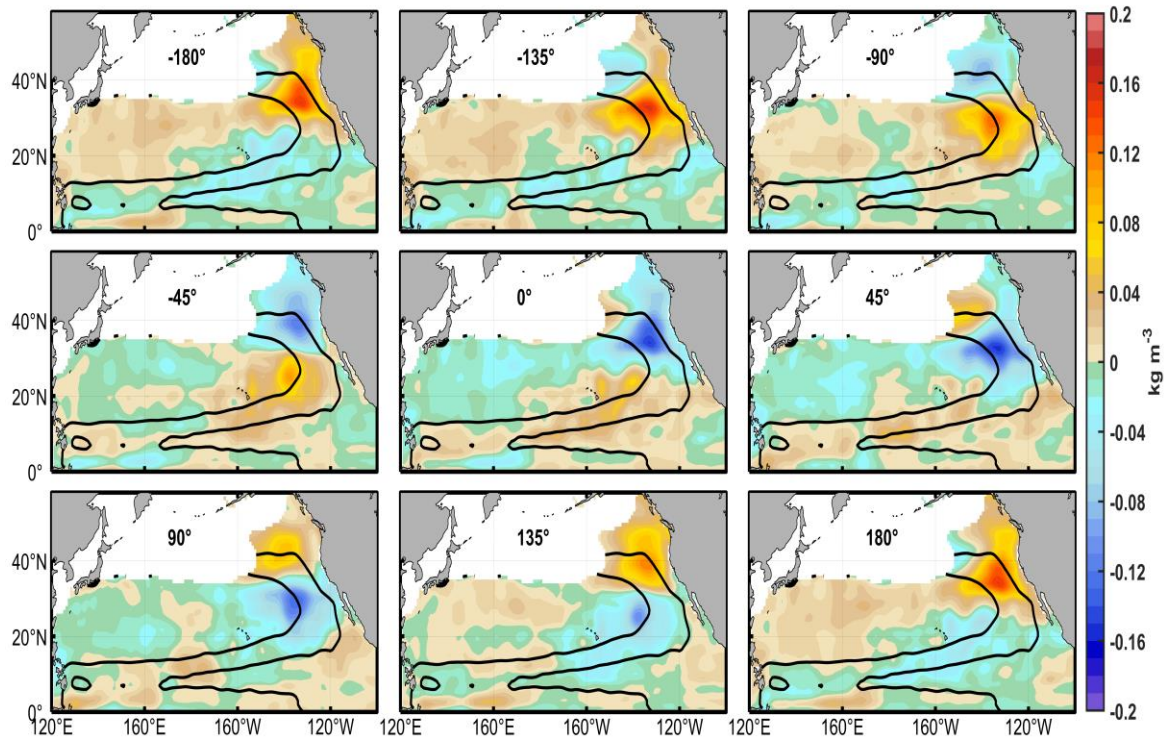


Figure S2.2 Reconstruction of the first CEOF mode of spiciness anomalies showing one full cycle (-180° to 180°) every 45° phase intervals. The thick black lines represent the NPP. The CEOF analysis is based on EN422.

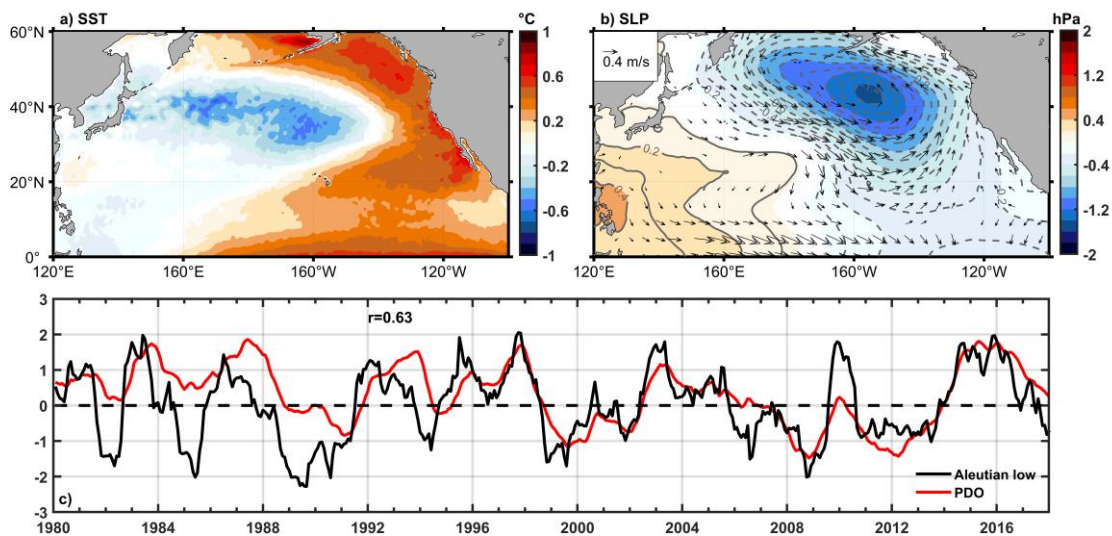


Figure S2.3 Pacific (a) SSTa and (b) SLP anomalies (shading and gray contours) regressed with the PDO index. Wind vectors at 10 m regressed with the PDO index are also imposed in (b). Only regressed values significant at the 95% confidence level (Student's *t*-test) are shown. (c) Time series of the Aleutian Low (black, the first principal component of the EOF analysis of interannual SLP anomalies between 20° - 60° N, 120° E- 80° W. The first EOF mode explains 41% of the total SLP variance and the second EOF mode accounts for 19%). The red curve is the PDO index. The simultaneous correlation between the Aleutian Low and PDO is 0.63.

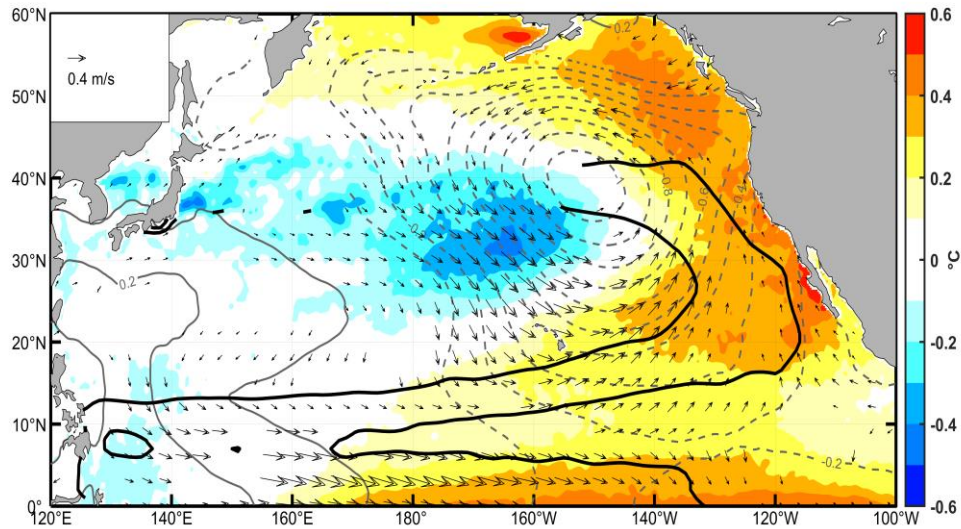
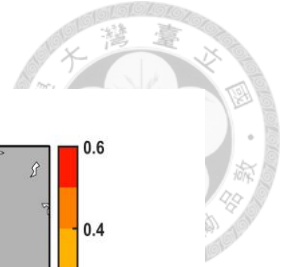


Figure S2.4 Pacific SSTA (shading) and SLP anomalies (hPa, gray contours) regressed with the PC1 of spiciness anomalies (PC1 lags 22 months). Wind vectors at 10 m regressed with the PC1 are also imposed. Only regressed values significant at the 95% confidence level are shown. The thick black lines represent the NPP. The CEOF analysis is based on EN422.

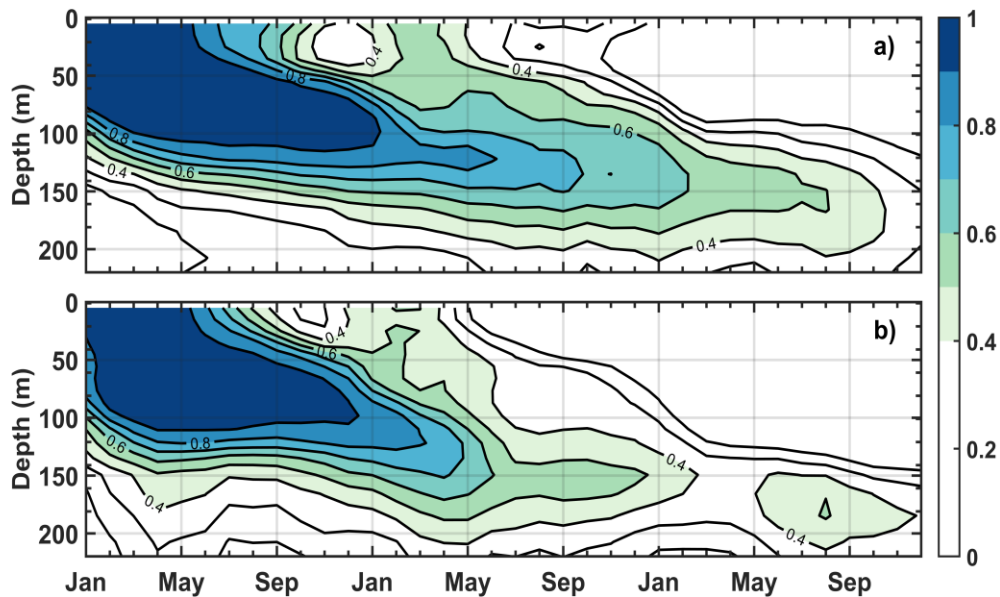


Figure S2.5 Lead-lag correlation coefficients between the February-April SSTA and temperature anomalies at different depths and months in the (a) midlatitude (the red box) and (b) 30-38°N, 145-130°W. The contour interval is 0.1. EN422 from 1980 to 2020 is used for the analysis.

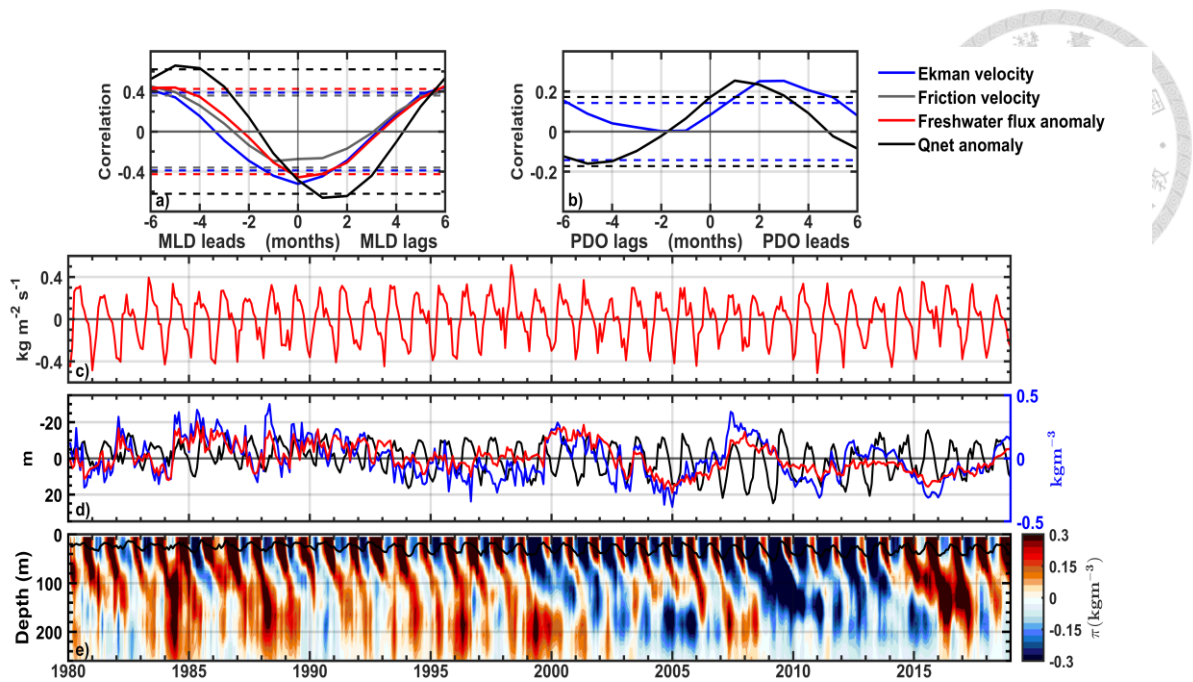


Figure S2.6 (a) Lead-lag correlation coefficients between interannual MLD and interannual Ekman velocity (blue), friction velocity (gray), freshwater flux anomaly (red) and Qnet anomaly (black). Horizontal dashed lines indicate the 95% confidence level. (b) Same as (a) but for PDO index. (c) Time series of Qnet (positive downward). (d) Time series of anomalous MLD (black, left) with positive (negative) values indicate deepening (shoaling) of the mixed layer. Time series of the areal mean (the blue box) of spiciness anomalies averaged between $25 \sigma_\theta$ (blue, right) and $25\text{-}26 \sigma_\theta$ (red, right). (e) Same as **Figure 2.13c** but for depth-time plot. The black line denotes the MLD. All the four variables contribute to MLD changes are averaged in $20\text{-}30^\circ\text{N}$, $160\text{-}110^\circ\text{W}$.

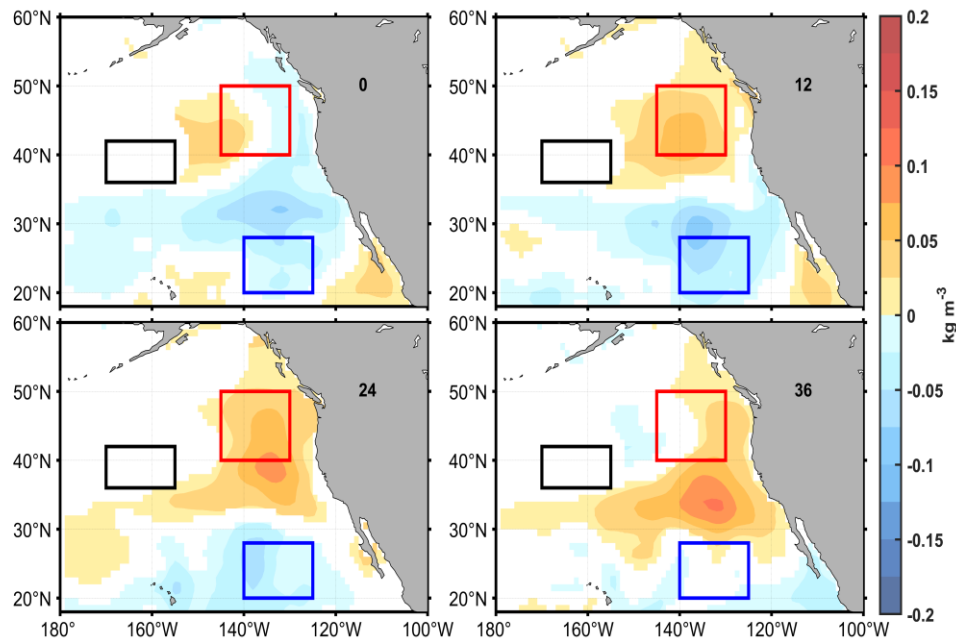


Figure S2.7 Same as **Figure 2.14** but for wind stress curl anomalies.

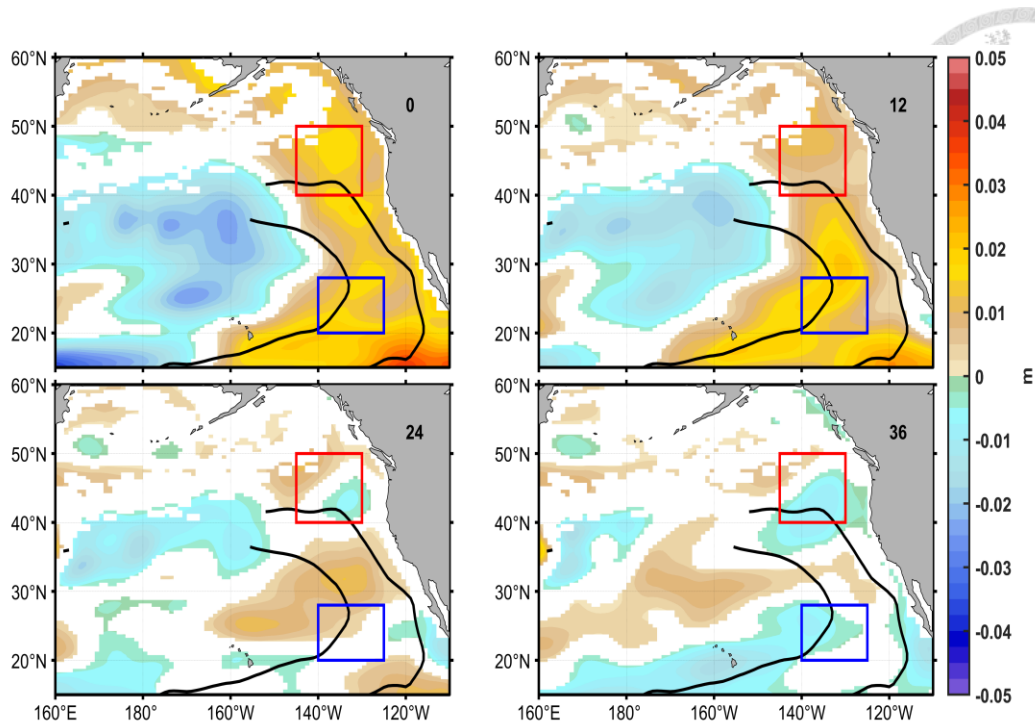


Figure S2.8 Sea surface height anomalies regressed with the PDO index from lag 0 to lag 36 months (only regressed values significant at the 95% confidence level according to a student's t-test are shown). The red and blue boxes are the regions defined in **Figure 2.6**. The thick black lines represent the NPP. Positive lags indicate PDO leads

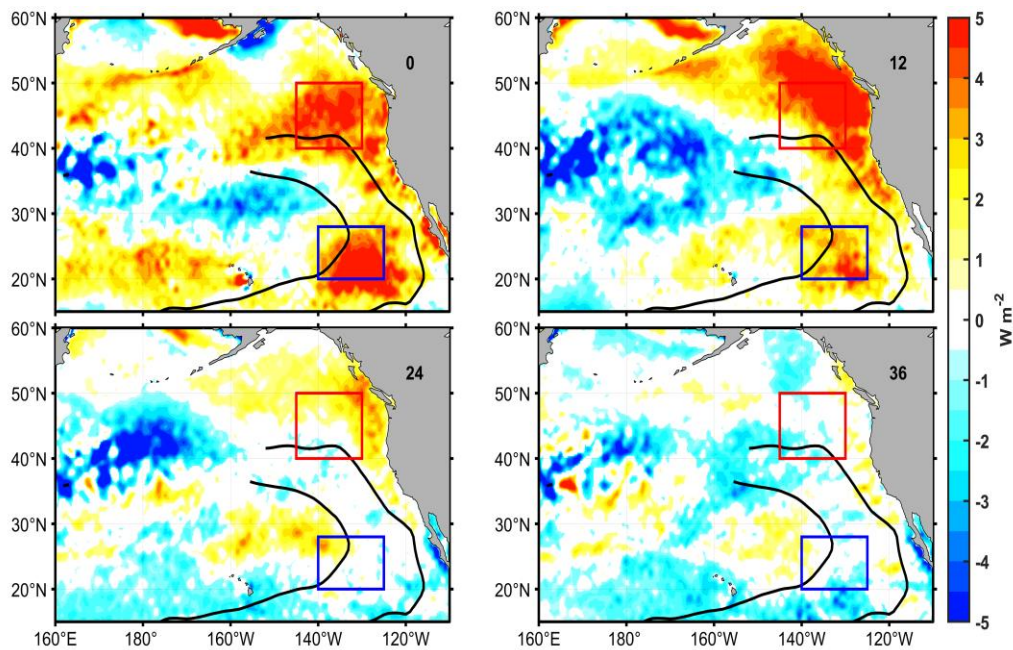


Figure S2.9 Same as **Figure S2.8** but for Qnet anomalies (positive downward).

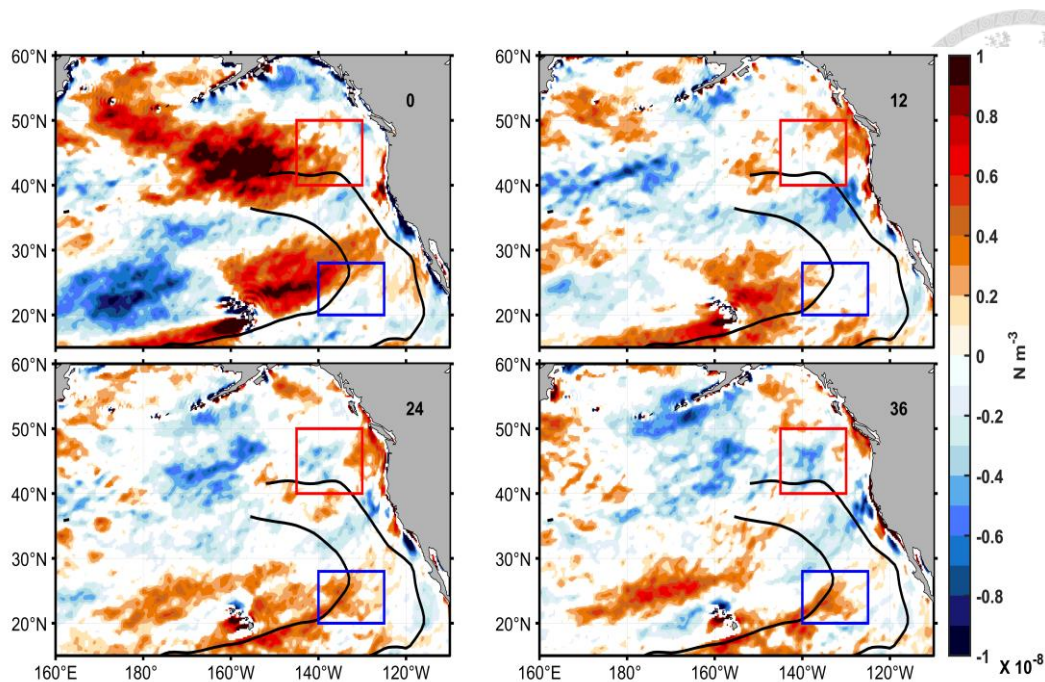


Figure S2.10 Same as **Figure S2.8** but for wind stress curl anomalies.

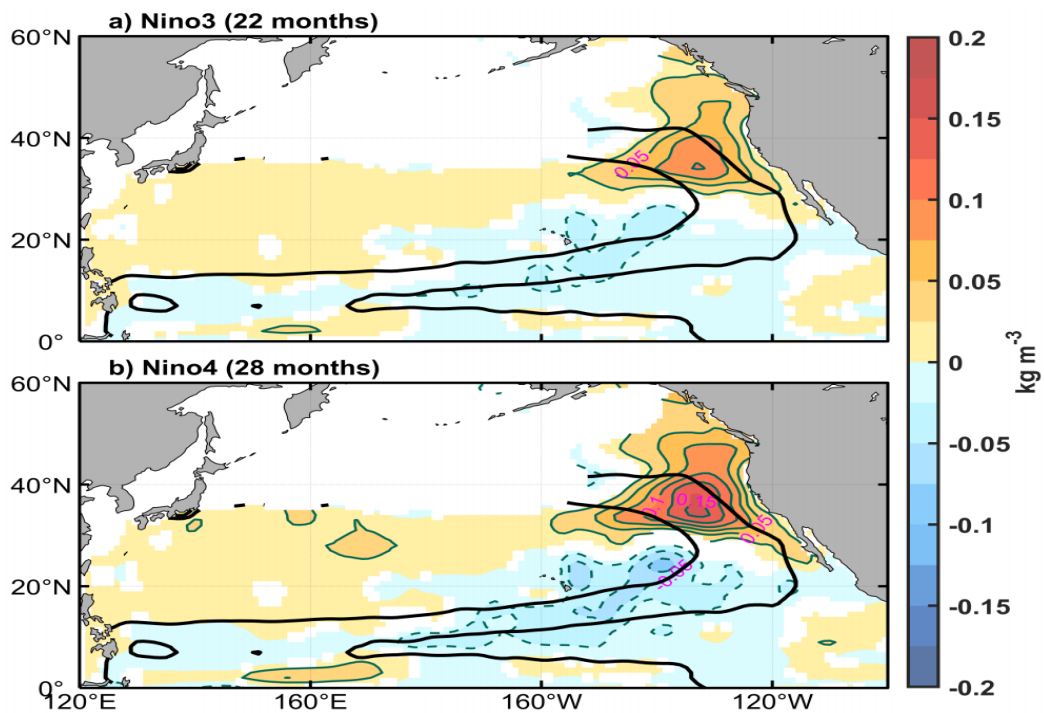


Figure S2.11 Reconstructed spiciness anomalies using CEOF1 regressed with the (a) Niño3 and (b) Niño4 SST indices at lag 22 and 28 months, respectively. Only regressed values significant at the 95% confidence level according to a Student's t-test are shown. The contour interval is 0.025 kg m^{-3} and the solid (dashed) contours denote positive (negative) anomalies. The thick black lines represent the NPP. The CEOF analysis is based on EN422.

Chapter 3

The role of off-equatorial subsurface temperature anomalies in the phase reversal of Tropical Pacific Decadal Variability



This Chapter is to be submitted for publication as:

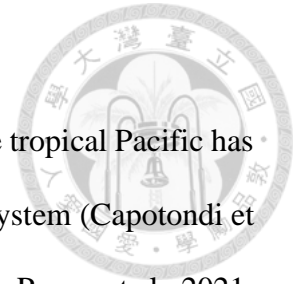
San S-C, Tseng Y-h, Ding R, and Di Lorenzo E. Initiating Tropical Pacific Decadal Variability from off-equatorial subsurface temperature anomalies. *npj Climate and Atmospheric Science*.

Preface

We demonstrate the key role of off-equatorial subsurface temperature anomalies in the phase reversal of the Tropical Pacific Decadal Variability (TPDV) using the observation and model experiments. Specifically, during the mature warm phase of the TPDV, the positive sea surface temperature (SST) anomalies in the equatorial central Pacific induce anomalous cyclonic circulation in the off-equatorial northwestern (southwestern) Pacific with positive (negative) wind stress curl anomalies between 2-15°N (2-15°S). The resulting positive Ekman pumping induces surface divergence, leading to the formation of negative isopycnal temperature anomalies. These subsurface signals which have the center of action in the northwest then slowly migrate toward the central Pacific via the North Equatorial Countercurrent (NECC), outcropping eastward along the equator. They further initiate a central equatorial cooling around three years later. In addition, the TPDV-forced extratropical atmospheric anomalies during the warm phase potentially induce the change of the Kuroshio Extension (KE) that subsequently projects its atmospheric forcing on the Pacific Meridional Mode (PMM) to further strengthen the subsurface-produced equatorial disturbance 0-12 months before the peak phase. The combined contribution of off-equatorial subsurface signal and PMM eventually turns the tropical system into the cold phase after five years. The center of negative equatorial SST anomalies then forces anomalous atmospheric circulation to form positive subsurface temperature anomalies in the off-equatorial western area and in turn may further reverse the state of KE. Therefore, a periodic oscillation of around 10 years is achieved via the above off-equatorial subsurface temperature anomalies and extratropical-tropical ocean-atmosphere interaction.

3.1 Introduction

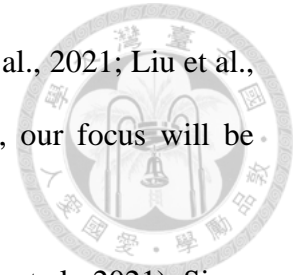
Internal decadal-scale sea surface temperature (SST) variability in the tropical Pacific has long been recognized as an important component of the global climate system (Capotondi et al., 2023; Di Lorenzo et al., 2023; Knutson and Manabe, 1998; Liu, 2012; Power et al., 2021; Tourre et al., 2001; Zhang et al., 1997), triggering tremendous extreme weather events globally such as droughts (Okumura et al., 2017a) and flooding (Zhang et al., 2016). Tropical Pacific Decadal Variability (TPDV) is generally defined as variability longer than the dominant 2-7-year time scales of El Niño-Southern Oscillation (ENSO) (Timmermann et al., 2018), obtained by an 8-year lowpass filtering (Liu and Di Lorenzo, 2018; Zhao and Di Lorenzo, 2020) or 8-40 year bandpass filtering (Power et al., 2021) SST in the tropical Pacific. The spatial pattern of TPDV (derived by the regression map) is characterized by anomalies of one sign covering the equator and extending northeastward and southeastward toward extra-tropics, combined with anomalies of the opposite sign in the central extra-tropics of both hemispheres (Liu and Di Lorenzo, 2018; Power et al., 2021), resembling the pattern associated with the Interdecadal Pacific Oscillation (IPO) (Power et al., 1999) as well as ENSO (Sullivan et al., 2016). However, TPDV exhibits a wider meridional extent (Newman et al., 2016; Power and Colman, 2006; Zhang et al., 1997) and shows stronger variability in the tropics than in extra-tropics (Kleeman et al., 1999; Liu et al., 2022; Newman et al., 2016; Power et al., 2021; Tourre et al., 2001). Recent studies have also identified that TPDV manifests the largest loadings in the equatorial central and northeastern Pacific (Chunhan et al., 2021; Kleeman et al., 1999; Liu et al., 2022), bearing resemblance to the Central Pacific El Niño (Ashok et al., 2007; Capotondi et al., 2022) and the Pacific Meridional Mode (PMM) (Chiang and Vimont, 2004; Stuecker, 2018) patterns. In addition, some studies suggested that

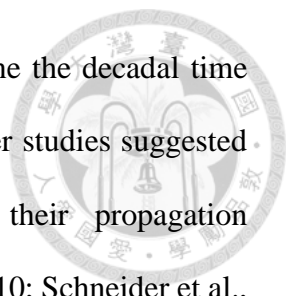


TPDV exhibits a prominent periodicity of around 11 years (Chunhan et al., 2021; Liu et al., 2022) mainly observed after 1950 (Chunhan et al., 2021). Therefore, our focus will be specifically on the TPDV at this time scale range.

The origin of the TPDV, however, remains unclear (Liu, 2012; Power et al., 2021). Since the TPDV and ENSO share a similar spatial structure and major episodes of decadal climate variability are well captured by the relative number of El Niño and La Niña events (Power et al., 2021), TPDV is therefore merely regarded as the long-term linear average of the ENSO cycle (Vimont, 2005) or the residual signal modulated by the nonlinearity of ENSO (Cibot et al., 2005; Kim and Kug, 2020; Rodgers et al., 2004). This implies that TPDV may largely originate largely in the tropical Pacific (Liu et al., 2022; Liu et al., 2002; Wu et al., 2003). In contrast, the wintertime stochastic forcings in the extratropical North and South Pacific have been proposed as the primary driver of TPDV (Di Lorenzo et al., 2015; Joh and Di Lorenzo, 2019; Zhao and Di Lorenzo, 2020). Specifically, the tropical ocean slowly integrates the seasonal progression of these remote forcings (Zhao and Di Lorenzo, 2020) in combination with positive feedbacks (zonal advective and thermocline feedback) in the tropics (Di Lorenzo et al., 2015), giving rise to TPDV. This perspective suggests that the origin of TPDV might be rooted in the extra-tropics. Although the proposed null hypothesis can explain the variance of decadal variability to a certain extent, it cannot account for the preferred time scale of the oscillating system and the phase transition.

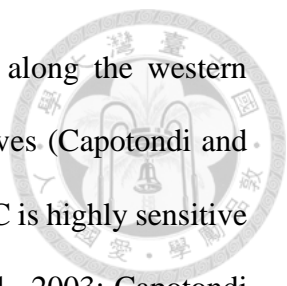
Due to the large oceanic heat capacity, ocean dynamics have been proposed to provide the key memory for TPDV (Liu, 2012). The subduction of SST anomalies in the subtropical northeastern Pacific (Schneider et al., 1999a) and their subsequent equatorward propagation toward the equatorial region via the so-called subtropical cell (STC) (Capotondi et al., 2005;





Liu, 1994; McCreary and Lu, 1994) has been hypothesized to determine the decadal time scale of the oscillation (Gu and Philander, 1997). However, some earlier studies suggested that these subtropical thermal anomalies decay rapidly during their propagation (Kolodziejczyk and Gaillard, 2012; Liu and Shin, 1999; Sasaki et al., 2010; Schneider et al., 1999b) and it is unlikely that the anomalies can reach the equator with sizeable amplitude (Hazeleger et al., 2001; Schneider et al., 1999a). In contrast, other studies indicated that compensating temperature and salinity anomalies (spiciness anomalies) can potentially reach the tropics, albeit with much-reduced amplitude (Li et al., 2012; Yeager and Large, 2004). Recently, a study has identified a decadal subsurface spiciness mode in the North Pacific associated with the Aleutian Low and Pacific Decadal Oscillation (PDO) that can propagate toward the equatorial region. However, the degree of impact that the decadal spiciness mode has on TPDV remains largely uncertain due to the negligible amplitude observed in the tropics and the relatively short observational record (San and Tseng, 2023). In the South Pacific, it is generally agreed that extratropical subsurface temperature/salinity anomalies can effectively propagate to the tropics on a timescale of 5-7 years and potentially contribute to equatorial climate variability (Giese et al., 2002; Imada et al., 2016; Luo et al., 2003; Luo and Yamagata, 2001; Luo et al., 2005; O'Kane et al., 2014; Tatebe et al., 2013; Zeller et al., 2021).

Another potential driver for TPDV is the variability in the strength of the STC which can modulate the amount of water transported to the equator and consequently determine the decadal variability of equatorial SST anomalies (Kleiman et al., 1999; McPhaden and Zhang, 2004; Nonaka et al., 2002; Solomon et al., 2003; Zhang and McPhaden, 2006). The preferred oscillation time scale of the system is accomplished via the westward propagation of wind-



forced oceanic Rossby waves, followed by equatorward propagation along the western boundary as coastal-trapped waves and along the equator as Kelvin waves (Capotondi and Alexander, 2001; Meehl and Hu, 2006). However, the strength of the STC is highly sensitive to both the location and magnitude of the wind forcing (Capotondi et al., 2003; Capotondi and Qiu, 2022; Graffino et al., 2019). In addition, TPDV can contribute to extratropical wind variability through the atmospheric bridge (Alexander, 1990). Therefore, unambiguously determining the origin and preferred time scale of STC-related mechanisms remains challenging.

Here, we demonstrate that the subsurface temperature anomalies originating in the off-equatorial northwestern Pacific can account for the phase transition of the TPDV using available observational and reanalysis datasets, along with numerical experiments. Furthermore, a preferred oscillation timescale, specifically 10-20 years, can be established through the combined contribution of subsurface temperature anomalies and extratropical-tropical ocean-atmosphere interaction.

3.2 Data and methodology

Observational and reanalysis datasets: For subsurface temperature and salinity, we use the latest EN.4.2.2 (EN422) from the Met Office Hadley Centre (Good et al., 2013). The EN422 has four ensemble members which are different in the scheme used to adjust bias in Mechanical Bathythermograph and Expendable Bathythermographs data. These ensembles are distributed on a 1° horizontal resolution over 42 irregularly spaced depth levels spanning from 1900 to present at monthly intervals. The ensemble of EN.4.2.2.analyses.g10 from 1950 to 2021 is employed here. Similar results are obtained in the other three ensembles. For the SSH data, the Estimating the Circulation and Climate of the Ocean project, version 3

(GECCO3) (Köhl, 2020) is utilized. This data set has 1° horizontal resolutions and 40 vertical levels from 1948 to 2018. For the ocean currents, the Global Ocean Data Assimilation System (GODAS) with 0.33° latitude \times 1° longitude during 1980-2021 (Behringer et al., 1998; Behringer and Xue, 2004) is used.

For atmospheric variables, monthly SLP and 10-m winds are from the National Centers for Environmental Prediction-National Center for Atmospheric Research Reanalysis 1 dataset (Kalnay et al., 1996). These data are distributed on a $2.5^\circ \times 2.5^\circ$ latitude-longitude grid, covering the period from 1948 to the present. In addition, the global 1° gridded monthly SST from the Hadley Centre Global Sea Ice and Sea Surface Temperature (HadISST) dataset (Rayner et al., 2003) is used.

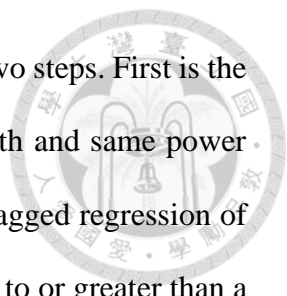
Subsurface temperature coordinate transformation and NECC pathway: All data are linearly detrended before conducting analyses and anomalies are defined as deviations from the climatology of the whole period of the respective dataset. As the focus of the study is on the decadal time scale, an 8-20-year Lanczos bandpass filter is used (Duchon, 1979). For subsurface data, the temperature on pressure coordinates is converted to time-mean sigma coordinates with an increment of 0.02 kg m^{-3} by linear interpolation (the resulting isopycnal temperature is not necessarily salinity compensated). We then define two isopycnal ranges of the 22-24.5 σ_θ and 24.5-26 σ_θ to identify the origin of the TPDV. This separation aims to quantify the former as the tropical origin and the latter as the extratropical origin (Figure S3.2) (Zeller, 2020). Our result is similar regardless of the chosen upper isopycnal ranges (22.4-24.5 σ_θ , 22.5-24.5 σ_θ or 23-24.5 σ_θ) as well as lower isopycnals (24.5-25.5 σ_θ , 25-25.5 σ_θ or 25-26 σ_θ). The ocean pathway is represented by the mean acceleration potential

(McDougall and Klocker, 2010) referenced to 1000 dbar and mean currents evaluated on the isopycnal surface.

Wavelet analysis. As the widely used Morlet wavelet analysis (Torrence and Compo, 1998) exhibits bias in the estimate of wavelet power spectra of geophysical time series, we use the bias-rectified wavelet approach from Liu et al. (2007). We also perform wavelet coherence analysis with the software package from Grinsted et al. (2004) to detect the phase relationship between surface and subsurface variability in the Niño4 region.

Multitaper Frequency-Domain Singular Value Decomposition (MTM-SVD): We employ the MTM-SVD which is a powerful multivariate signal processing method ideal for extracting narrowband spatial-temporal variability in a red noise background (Mann and Park, 1994, 1999). The feature of decadal variability is then explored by performing MTM-SVD analysis of joint normalized raw detrended oceanic and atmospheric fields in the domain of 40°S-40°N and 120°E-80°W. Our result is not sensitive to the domain or combined fields used for the analysis. The MTM-SVD analysis was performed using K=3 data tapers (windowing functions) and a time-frequency bandwidth product of $NW=2$. The significant level of the resulting LFV spectrum is estimated by 300 synthetic time series of the original dataset obtained by temporal shuffling. The 95% confidence level is used to distinguish the LFV peak from the “locally white” noise background.

Random phase test: To identify the causal relationship between the fields, lagged correlation and regression are used. Because bandpass filtering strongly reduces the effective sample size of the time series and the degree of reduction is hard to estimate accurately, we use a non-parameter method (random-phase) (Ebisuzaki, 1997) to test the significance of our statistical analysis. Supposedly, $r(A, B)$ is the regression between two time series A and B at



a certain lag. The statistical significance of regression can be tested via two steps. First is the generation of 8000 synthetic time series from A that has the same length and same power spectrum but differences in temporal phases. Second, we calculate the lagged regression of the reconstructed time series with B. If the magnitude of $r(A, B)$ is equal to or greater than a certain percentage (at least 90% in this study) of the regressions from the random-phase time series, we assume that $r(A, B)$ passes the confidence level.

Numerical experiment: The dynamical processes involved in our analysis are further confirmed using the numerical experiments based on the Community Earth System Model (CESM) version 1.2.2. To verify the role of TPDV-induced anomalous atmospheric circulation, we conduct the specified SST experiments with the Community Atmospheric Model version 5 (CAM5). The prescribed heat source is confined to the region 5°S - 5°N , 160°E - 160°W while outside this domain climatological SST is applied (Meehl et al., 2016; Meehl et al., 2021). We add 2°C SST to the climatological value within the defined region. The experiment is run for 30 years. The anomalies are then defined as deviations from a 30-year control run with specified climatological SST.

We also perform a 10-member ensemble run of the prescribed 2°C SST value in the region mentioned above. Each ensemble member is slightly different in the initial condition by randomly imposing small perturbations to the initial temperature fields. Specifically, we set the CESM1.2.2 namelist variable “pertlim” ranging from 1×10^{-14} to 10×10^{-14} . All ensemble members are then run for 10 years and anomalies are defined as deviations from a 30-year control run with specified climatological SST.

To demonstrate the role of TPDV-induced off-equatorial subsurface temperature anomalies, the Pacific anomalous wind field associated with the positive phase of TPDV

(Figure 3.3a) is superimposed to force the Parallel Ocean Program version 2 (POP2) (Smith et al., 2010). We perform a 15-member ensemble run which is different slightly in the perturbation in addition to the added TPDV anomalous wind field. The imposed wind field is as follows,

$$\text{Imposed wind field} = \text{Climatological wind} + \text{TPDV associated wind} + \text{Perturbed wind}$$

where the perturbed wind is generated by a random matrix of predefined coefficients (ranging from 0.0001 to 0.0005). We choose to perturb the 10-m wind field in the zonal, meridional, and both directions concerning the defined coefficients. Each ensemble member is run for 30 years and anomalies are defined as departures from the 100-year control run with normal year forcing. All the statistical significance of the modeling results is based on a Student's t test.

3.3 Results

3.3.1 Observed Pacific decadal climate variability

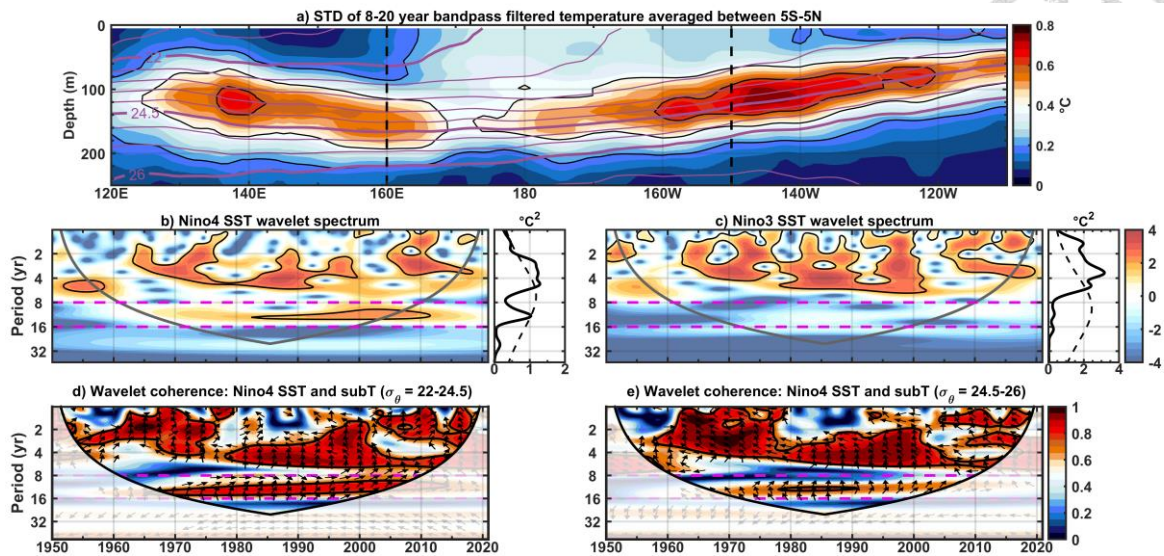
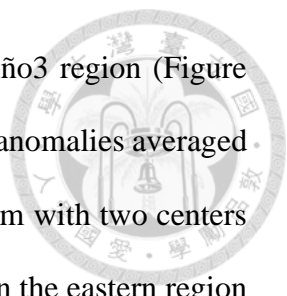


Figure 3.1 (a) Standard deviation of 8-20-year bandpass filtered temperature anomalies (shading and thin black contours) averaged between 5°S-5°N. The contour interval is 0.2°C and zero contours are omitted. Violet lines denote the mean climatological potential density with 0.5 kg m⁻³ contour intervals. The vertical dashed black lines denote the longitude of 160°E and 150°W. (b) Bias-rectified wavelet power spectrum (shading) and corresponding global wavelet power spectrum of raw detrended Niño4 SST index. Thin black contours in the wavelet power spectrum and dashed black lines in the global power spectrum indicate statistical significance at the 90% confidence level when tested against a red-noise AR(1) process with lag-1 of 0.91. The parabola regions indicate the “cone of influence” where edge effects become important. The horizontal dashed pink lines indicate the 8 and 16 year periods. (c) same as (b) but for Niño3 SST index. Wavelet coherence between Niño4 SST index and Niño4 subsurface temperature anomalies averaged between (d) 22-24.5 σ_θ and (e) 24.5-26 σ_θ . The 95% significance level against red noise is shown as thick black contours. The vectors designate the relative phase relationship (pointing right indicates in phase, pointing left indicates out of phase and pointing vertically upward means the Niño4 SST index lags subsurface temperature by 90°). The horizontal dashed magenta lines are the same as (b).

Prominent low-frequency variability is identified by performing bias-rectified wavelet analysis (Liu et al., 2007) of raw detrended SST anomalies averaged in the Niño4 (5°S-5°N, 160°E-150°W) and Niño3 (5°S-5°N, 150°-90°W) regions (Figure 3.1b, c). Consistent with previous findings (Chunhan et al., 2021; Liu et al., 2022; Power et al., 2021), pronounced decadal variability is found in the Niño4 region characterized by a distinct spectral peak within 8 and 16 year periods (Figure 3.1b). This feature is also observed in the local fractional variance (LFV) spectrum for the combined oceanic and atmospheric fields (Figure S3.1). In



contrast, there is no significant peak within the decadal band in the Niño3 region (Figure 3.1c). The standard deviation of 8-20 year bandpass filtered temperature anomalies averaged between 5°S-5°N shows significant decadal variance at depth below 50 m with two centers of action: one in the western region from 130°E to 165°E and the other in the eastern region from 160°W to 120°W (Figure 3.1a), similar to Figure 1a in Luo and Yamagata (2001). These maximum variabilities are mainly confined to the isopycnals 22.5-25 σ_θ . An important feature here is that the isopycnals shoal eastward and upward (Figure S3.2a), allowing the temperature on the 22-24.5 σ_θ surfaces (thick violet lines in Figure 3.1a) to effectively affect Niño4 mixed layer temperature (Figure S3.3). Figure 3.1d shows the wavelet coherence and phase relation between Niño4 SST and Niño4 subsurface temperature averaged between 22-24.5 σ_θ . The arrows point from left to right at around 45°, suggesting that the surface and upper oceanic variability are in phase at periods greater than eight years. The deeper isopycnal temperature anomalies also exhibit a noticeable in phase relationship with surface temperature (Figure 3.1e) but the coherence is not statistically significant compared to the upper layer (Figure 3.1d).

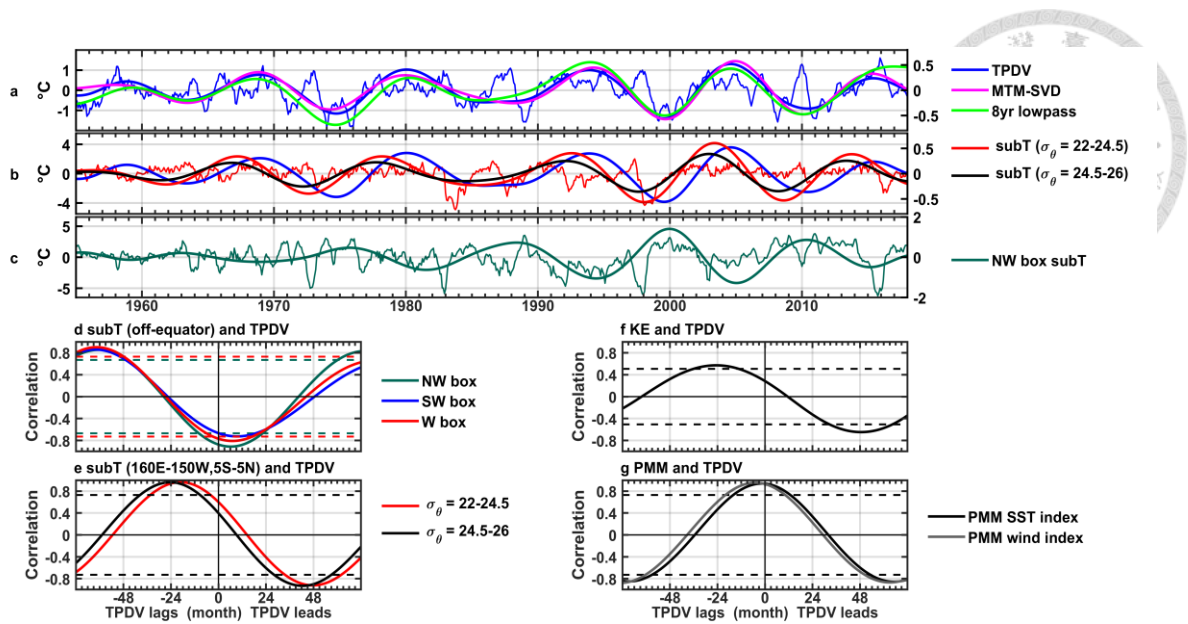


Figure 3.2 (a) Temporal evolution of raw detrended Niño4 SST index (left axis, thin blue) and its 8-20-year bandpass filtered component (TPDV index, right axis, thick blue) and 8-year lowpass filtered component (right axis, green). The reconstructed Niño4 SST index using the MTM-SVD method on a decadal timescale (period ~ 10.3 year) is shown in magenta (right axis). (b) Temporal evolution of raw detrended Niño4 subsurface temperature anomalies averaged between 22-24.5 σ_θ (left axis, thin red) and its reconstruction using MTM-SVD on a decadal timescale (right axis, thick red). Similarly, the reconstruction of Niño4 subsurface temperature anomalies averaged between 24.5-26 σ_θ is shown in black (right axis). The blue line is the same as (a). (c) Temporal evolution of raw detrended subsurface temperature anomalies averaged between 22-24.5 σ_θ in 6°-11°N, 140°-160°E (NW box in **Figure 3.4**) (left axis, thin green) and its 8-20-year bandpass filtered component (right axis, thick green). Lead-lag correlation coefficients between TPDV index and (d) 8-20-year bandpass filtered temperature anomalies averaged between 22-24.5 σ_θ in (green) NW box, (blue) 6°-11°S, 150°-170°E (SW box) and (red) 5°S-5°N, 150°-160°E (W box), (e) reconstructed Niño4 subsurface temperature anomalies averaged between (red) 22-24.5 σ_θ and (black) 24.5-26 σ_θ using the MTM-SVD, (f) 8-20-year bandpass filtered Kuroshio Extension (KE) index defined as area-averaged SSH anomalies in 31°S-36°N, 140°-165°E and (g) 8-20-year bandpass filtered PMM SST (black) and wind (gray) index. Horizontal dashed lines in (d-g) show the 95% confidence level based on the non-parameter random-phase test.

As decadal variability centering in the equatorial central Pacific, here we define a TPDV index using an 8-20 year bandpass filtered Niño4 SST anomalies to describe the physical processes responsible for the variation (similar results are obtained if an 8-year lowpass filtering or MTM-SVD is used, Figure 3.2a). The temporal evolution of the Niño4 22-24.5 σ_θ temperature anomalies extracted by the MTM-SVD shows the pronounced feature of

decadal variability (Figure 3.2b), in line with the global spectral peak (Figure 3.1c). Its variation exhibits a larger magnitude compared to the lower isopycnal level (thick red and black lines in Figure 3.2b), consistent with the wavelet coherence analysis in Figure 3.1. Moreover, the maximum values of the temperature anomalies between $22-24.5 \sigma_\theta$ lead the peaks of the TPDV index by months (correlation reaches 0.96 by 19 months in Figure 3.2e), in agreement with the relative phase relationship in Figure 3.1d. Therefore, upper oceanic variability emerges as a potential driver of TPDV, which will be examined further in the next section. The temperature between $24.5-26 \sigma_\theta$ also shows a strong correlation with TPDV, confirming the key role of subsurface temperature on TPDV. For simplicity, we focus entirely on the $22-24.5 \sigma_\theta$ in the following analysis unless otherwise noted.

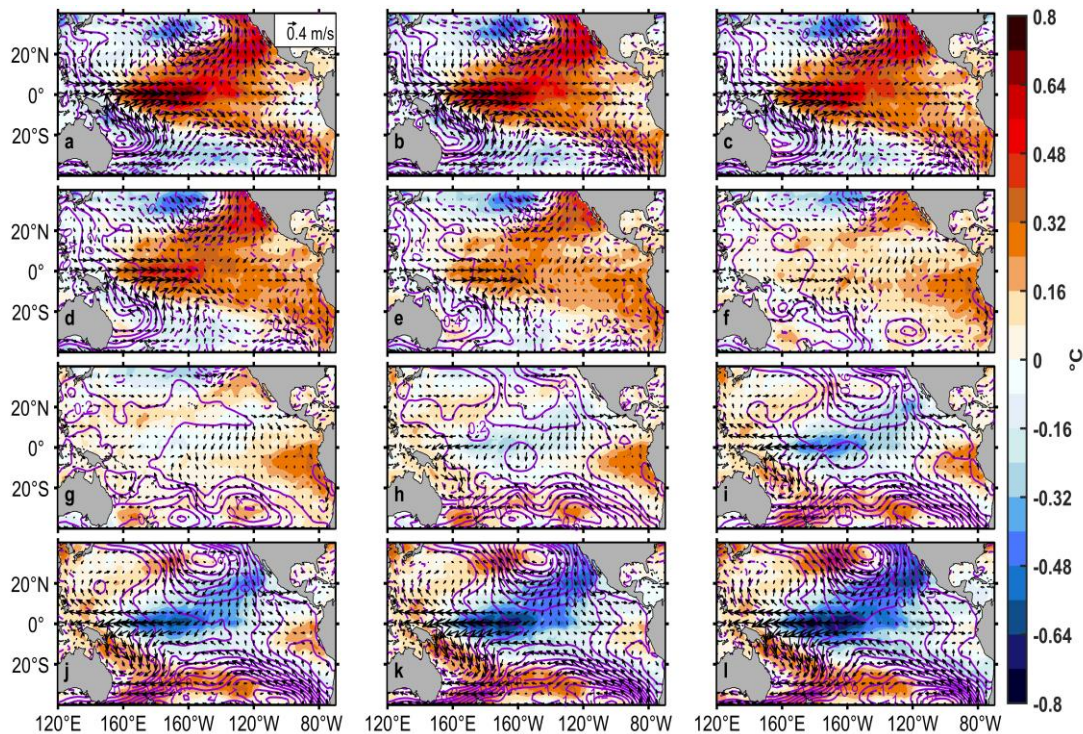
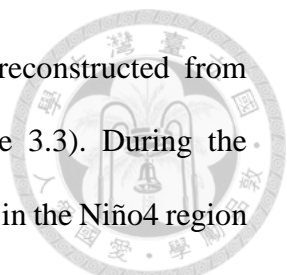


Figure 3.3 Phase evolution of Pacific SST (shading), SLP (contours, hPa), and 10-m wind vector anomalies on decadal timescales (period ~ 10.3 years in the MTM-SVD analysis). The contour interval is 0.1 hPa (positive/negative is solid/dashed). Each panel corresponds roughly to six months.



The decadal evolution of surface oceanic and atmospheric fields reconstructed from MTM-SVD illustrates a completed phase transition of TPDV (Figure 3.3). During the positive phase of TPDV (Figure 3.3a), the largest SST loadings are found in the Niño4 region and northeastern Pacific. This characteristic is consistent with previous studies based on MTM-SVD analysis of combined SST, sea surface height (SSH), and the 5°S-5°N average of subsurface temperature anomalies above 350 m (Liu et al., 2022) and the regression pattern of filtered SST anomalies on the first principal component of the leading EOF of the 8 to 40 year band SST anomalies (Power et al., 2021). The decadal sea level pressure (SLP) pattern is characterized by a band of anomalous high SLP anomalies confined to the western side of the basin while anomalous low pressure dominates in the east, especially in the extratropics. The latter structure resembles the Aleutian Low, suggesting possible atmospheric teleconnections excited by TPDV (Lyu et al., 2017; Stuecker, 2018; Zhang et al., 2022). The circulation patterns in the extratropical Northern and Southern Hemispheres are similar to those associated with the North (Stuecker, 2018) and South (Zhang et al., 2014) PMM, respectively. In addition, associated with the equatorial warm SST anomalies, strong westerly winds are observed west of 150°W while northwesterly and southeasterly winds dominate in the off-equatorial northwestern and southwestern Pacific, respectively. In general, these observed characteristics are consistent with many studies showing that the strong positive SST anomalies in the equatorial central Pacific (Figure 3.3a) can induce a typical Gill-type response, leading to a cyclonic circulation in the off-equatorial northwestern and southwestern Pacific (Meehl et al., 2021). The corresponding positive (negative) wind stress curl anomalies in the 2-15°N (2-15°S) latitude band (Figure S3.4a) then induce positive Ekman pumping (Figure S3.4b) which in turn can lead to the formation of subsurface

temperature anomalies in the two regions (Figure 3.4a). This will be further examined in the next section.

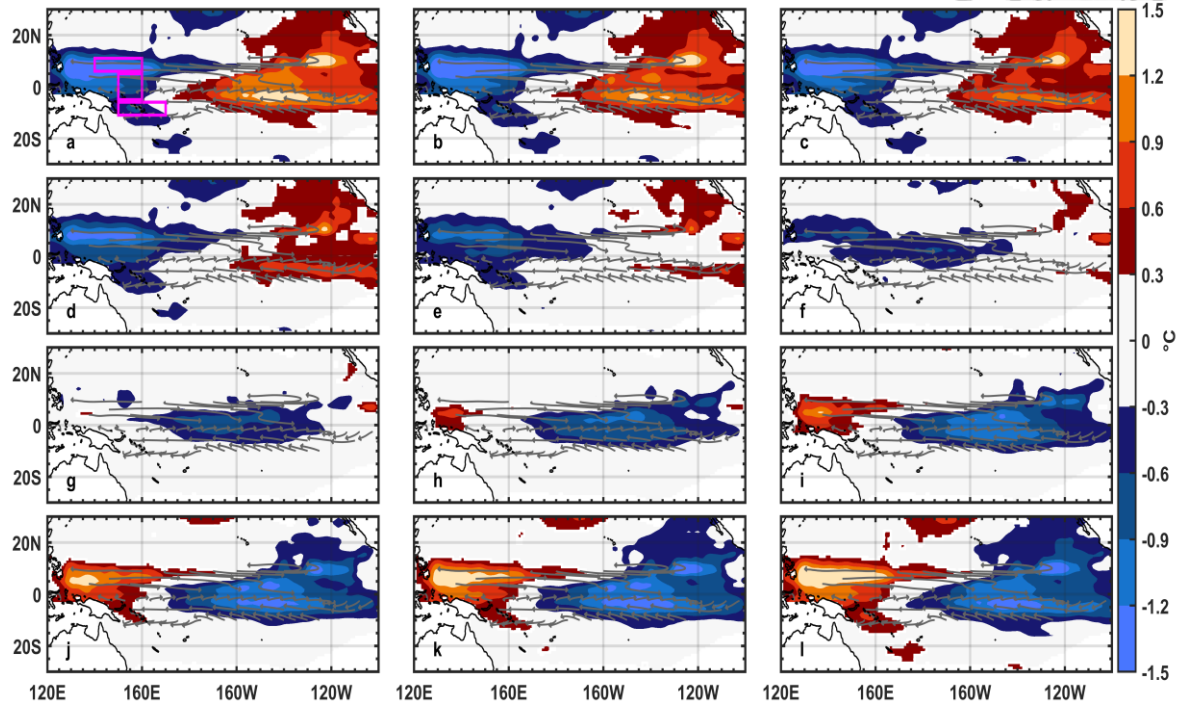


Figure 3.4 Same as **Figure 3.3** but for subsurface temperature anomalies averaged between $22\text{-}24.5 \sigma_\theta$. For clarity, positive (negative) temperature anomalies greater (smaller) than $0.3(-0.3)^\circ\text{C}$ have been colored in red (blue). Vectors denote the mean current on $23.5 \sigma_\theta$ derived from GODAS during 1980-2021. Only some representative current vectors are shown. The magenta rectangles in (a) are the region defined in **Figure 3.2**.

Before evolving into the mature cold phase (Figure 3.3l), negative PMM-like patterns occur in the extratropics concurrent with the strengthening of negative SST in the equatorial central and northeast Pacific (Figure 3.3i-k). Previous studies indicated that these meridional modes, also described as seasonal footprinting mechanism (Alexander et al., 2010; Vimont et al., 2001; Vimont et al., 2003), can contribute to equatorial low-frequency variability around 0-12 months before the mature state (Figure 3.2g) (Di Lorenzo et al., 2015; Zhao and Di Lorenzo, 2020). The regression of 8-20-year bandpass filtered SST anomalies upon the filtered PMM SST index (similar result obtained for the filtered PMM wind index) when the

later leads further confirm the role of PMM in enhancing SST variance around one year before the peak phase of TPDV (Figures 3.3j-k and S3.5g-h).

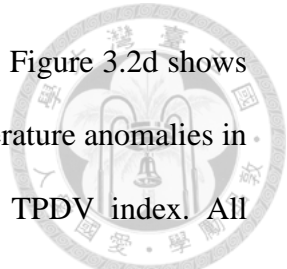
But how can the PMM be formed during the transition state to contribute to the growth of the TPDV? Apart from the contribution from internal stochastic forcing in the midlatitude, previous studies suggested that atmospheric teleconnection during the peak phase of the TPDV can drive change in the Aleutian Low or NPO on a time scale of 1-3 months (Alexander et al., 2002; Liu and Alexander, 2007; Trenberth et al., 1998). The resulting atmospheric anomalies associated with Aleutian Low/NPO then excite westward propagating oceanic Rossby waves to affect the KE system after 2.5-3 years (Andres et al., 2009; Ceballos et al., 2009; Taguchi et al., 2007). The change in the KE state then induces a persistent downstream atmospheric response that subsequently projects onto the forcing pattern of the PMM (around 0-12 months) and drives some fraction of equatorial low-frequency variability (Joh and Di Lorenzo, 2019). Consistent with previous finding (Joh and Di Lorenzo, 2019), the lead-lag correlation between the filtered KE index (defined as area-averaged SSH anomalies in the 31°S-36°N, 140°-165°E as in Qiu et al. 2014) and TPDV index exhibits a sinusoidal pattern in which the former leads the later by two years while the later can also provide feedback to the former after three to four years (Figure 3.2f). The regression of 8-20-year bandpass filtered SST anomalies upon the filtered KE index when the later leads further demonstrates that the KE can induce a weak but still significant fraction of low-frequency SST variability in the tropics (Figure S3.5a-d). In addition, the atmospheric structure associated with the KE can explain a certain degree of the PMM pattern (Figure S3.5). As a result, the KE state change partially excites the PMM (Frankignoul et al., 2011;

Kwon et al., 2010; Na et al., 2018; Qiu et al., 2014; Qiu et al., 2007; Taguchi et al., 2012) to further strengthen the low-frequency SST variance (Figures 3.3i-k and S3.5).

The above observed Pacific variability is consistent with the established decadal framework so far (Joh and Di Lorenzo, 2019) but the KE as well as the North and South PMM cannot fully account for the phase transition of TPDV (compare Figures 3.4f and S3.5a). In the next section, we will demonstrate that the equatorial emergence of subsurface temperature anomalies originating in the off-equatorial northwestern Pacific can trigger the phase transition of TPDV. Specifically, by combining these off-equatorial subsurface temperature anomalies with the previously established extratropical-tropical ocean-atmosphere interaction framework, we can establish the preferred decadal time scale oscillation in the Pacific.

3.3.2 Origin and preferred time scale of TPDV

The significant warming observed in the equatorial central Pacific during the positive phase of TPDV suggests a Gill-type response in the tropical Pacific, leading to the formation of subsurface temperature anomalies in the off-equatorial western Pacific (Meehl et al., 2021). Could the underlying water in the off-equatorial western Pacific potentially cause the phase reversal of TPDV? Figure 3.4 shows the phase evolution of upper ocean temperature anomalies reconstructed from MTM-SVD, which generally bears resemblance to those associated with surface variability. One important feature is the occurrence of a strong negative signal in the off-equatorial western Pacific centers around 6-11°N (Figure 3.2c) that has the opposite sign to the Niño4 SST anomalies during the positive TPDV mature phase (Figures 3.3a and 3.4a). In addition, subsurface anomalies precede surface variability in the western-central equatorial region during the transition state around three years later (Figures



3.3f-g and 3.4f-g), consistent with the correlation analysis in Figure 3.2. Figure 3.2d shows the lead-lag correlation between filtered area-averaged subsurface temperature anomalies in the western Pacific (three rectangle boxes in Figure 3.4a) with the TPDV index. All correlation exhibits a sinusoidal shape with extremely high crest and trough, suggesting the strong coupling between the western subsurface temperature anomalies and equatorial SST variability at the decadal time scale. Specifically, the correlation between subsurface temperature anomalies averaged over the off-equatorial northwest region (NW box) and TPDV reaches as high as 0.84 by 60 months when the former leads (Figure 3.2d). Additionally, the TPDV shows a much stronger correlation with NW subsurface temperature anomalies by about six months. This can establish a preferred decadal oscillation identified so far.

We further quantify the subsurface contribution to TPDV by regressing the filtered area-averaged temperature anomalies between $22\text{-}24.5\ \sigma_{\theta}$ in the NW box (the largest loading in Figure 3.4a) upon the 8-20-year bandpass filtered SST anomalies (Figure 3.5a). As expected, the strong negative subsurface temperature anomalies originating in the NW region can induce significant low-frequency variance in the Niño4 region five years later (Figures 3.3l and 3.5a). Note that the contribution from the subsurface is of greater magnitude than that from the KE during the transition phase (compare Figures 3.4f-g and S3.5a-b). Therefore, off-equatorial subsurface temperature anomalies are the primary contributor to the phase reversal of TPDV.

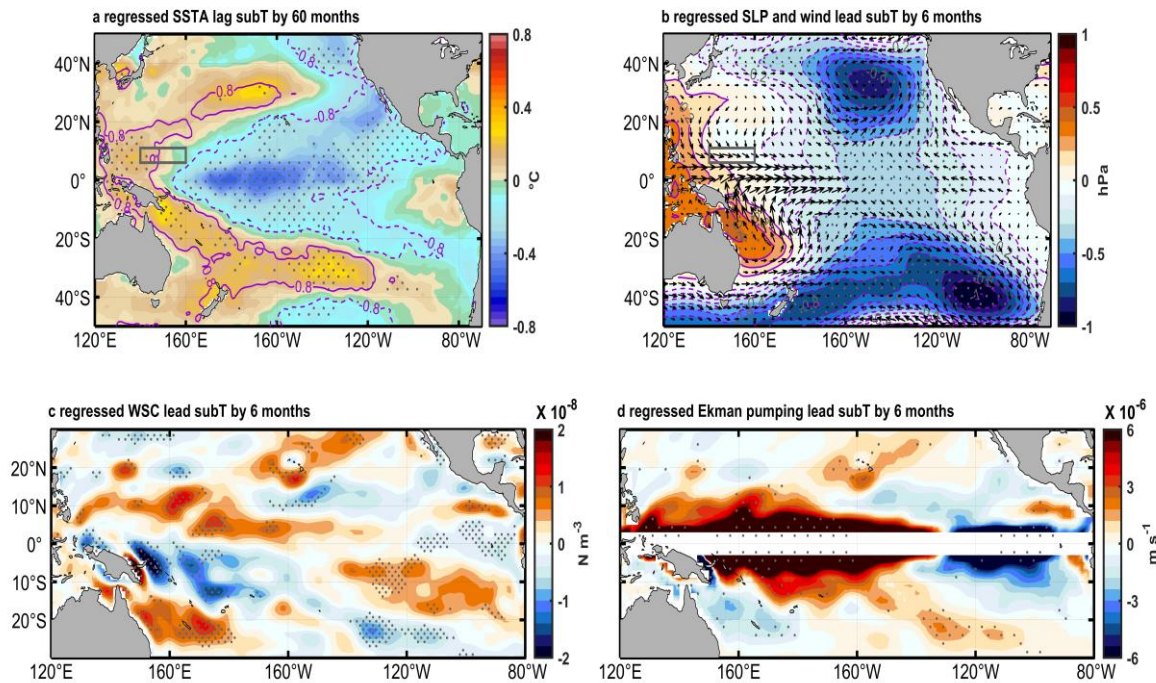
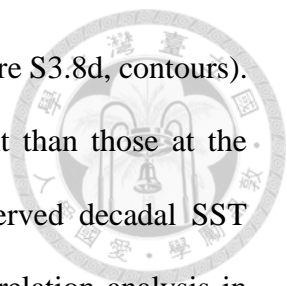


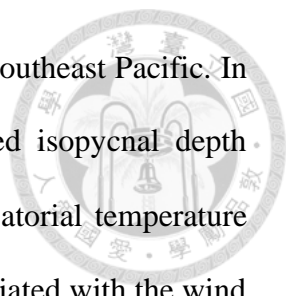
Figure 3.5 8-20-year bandpass filtered temperature anomalies averaged between $22-24.5 \sigma_\theta$ in NW box (gray rectangle) regressed with 8-20-year bandpass filtered (a) SST, (b) SLP (shading, contour, and stipple) and 10-m wind anomalies, (c) wind stress curl and (d) Ekman pumping. In (a), contours are the correlation coefficients between 8-20 year bandpass filtered NW box subsurface temperature anomalies and 8-20 year bandpass filtered SST anomalies. The contour interval is 0.2 and only correlation coefficients greater than 0.8 are shown. The contour interval in (b) is 0.1 hPa (positive/negative is solid/dashed). Regressed wind vectors are shown as a whole for clarity. Stipples indicate the region exceeding 95% confidence level with the random-phase test.

But how can the strong negative temperature anomalies approach the central basin and trigger the phase reversal of TPDV? The evolution in Figure 3.4 suggests the negative temperature anomalies in the NW box progress gradually eastward and equatorward following the mean current (gray vectors) toward the central basin. This process aligns with the shallow North Equatorial Countercurrent (NECC) pathway which can be defined by the acceleration potential evaluated on isopycnal surfaces (Figures S3.6 and S3.7). The reconstructed temperature anomalies using MTM-SVD averaged along 6°N further illustrate this propagation from around 140°E to 160°W (Figure S3.8d, shading) while the



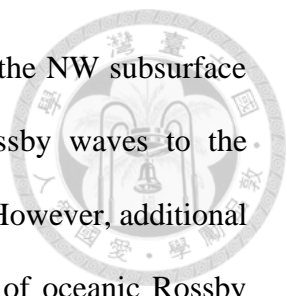
reconstructed signals on the equator can only reach as far as 170°E (Figure S3.8d, contours). In addition, the signal along 6°N is much stronger and more coherent than those at the equator. The NW subsurface temperature anomalies lead to the observed decadal SST variability in the Niño4 region (Figure S3.8e), consistent with the correlation analysis in Figure 3.2. As a result, the gradual migration of NW subsurface temperature anomalies toward the dateline via the NECC can effectively determine the preferred time scale and the phase transition of TPDV (Figure S3.8f). This is facilitated by the eastward shoaling of the examined isopycnal range (Figure S3.2) which allows the outcropped subsurface temperature anomalies to directly affect surface temperature variability (Figure S3.3), thus triggering the phase transition (Figure 3.3g) and inducing significant low-frequency variance in the Niño4 region (Figure 3.5a). This propagation pathway and time scale from the NW region to the equatorial Pacific are consistent with previous studies based on a shallower isopycnal level (Zhang and Rothstein, 2000) or depth-averaged temperature anomalies (Zhang et al., 1999).

We then examine how the subsurface temperature anomalies are formed in the off-equatorial western Pacific at the decadal time scale. The mean advection of spiciness anomalies (Schneider, 2000) or wind-forced thermocline displacement has been proposed (Capotondi and Alexander, 2001; Capotondi et al., 2003). To quantify the role of spiciness advection, we show the standard deviation of filtered subsurface temperature anomalies averaged between 22-24.5 σ_θ (temperature interpolated to time-varying isopycnals 22-24.5 σ_θ) in Figure S3.9a. The results indicate the decadal variability due to anomalous spiciness advection is weak in the off-equatorial western Pacific. There is only one noticeable center of action in the equatorial western Pacific around 140°E that cannot fully account for the observed large subsurface variability (Figure 3.4a). However, spiciness does contribute



significantly to decadal variability in the central-eastern equatorial and southeast Pacific. In contrast, the spatial structure of the standard deviation of the filtered isopycnal depth anomalies between $22-24.5 \sigma_\theta$ indicates that a large portion of off-equatorial temperature anomalies result from the vertical displacement of the thermocline associated with the wind forcing (Figure S3.9b). This suggests that wind-forced thermocline displacement plays a central role in forming the subsurface temperature anomalies in the off-equatorial western Pacific at the decadal time scale.

We further investigate the role of TPDV-related wind forcing in driving off-equatorial thermocline variability. Figure 3.5b shows the regression of 8-20-year bandpass filtered area-average temperature anomalies between $22-24.5 \sigma_\theta$ in the NW box upon the filtered SLP and 10-m wind anomalies. Similar to Figure 3.3a, the strong positive SST anomalies in the central equatorial Pacific induce a band of positive (negative) SLP anomalies in the west (east). The resulting cyclonic circulation in the northwest (southwest) produces strong northwesterly (southeasterly) equatorward of 15°N (15°S) (Figures 3.3a and 3.5b) with associated positive (negative) wind stress curl anomalies in the north (south) western Pacific (Figures S3.4a and 3.5c). Consequently, the positive Ekman pumping (Figures S3.4b and 3.5d) induces surface divergence and generates negative subsurface temperature anomalies in the off-equatorial western Pacific (Figure 3.4a). In addition, thermocline depth variabilities induced subsurface temperature changes can result from westward propagating oceanic Rossby waves excited by Ekman pumping anomalies originating in the off-equatorial eastern basin (Capotondi and Alexander, 2001; Meehl and Hu, 2006; Meehl et al., 2021). Figure S3.10 shows Hovmöller diagrams of SSH anomalies along different latitudinal bands in the North Pacific. Most of the prominent SSH signals that can propagate to the western boundary are observed west of



160°W. Further analysis of the lead regression of SSH anomalies onto the NW subsurface temperature anomalies shows the weak contribution of oceanic Rossby waves to the formation of western subsurface temperature anomalies (Figure S3.11). However, additional comprehensive analysis is needed to explore the extent of the impact of oceanic Rossby waves on off-equatorial northwestern subsurface temperature changes.

The negative temperature anomalies in the off-equatorial southwestern Pacific are relatively weaker compared to the northern counterpart (Figure 3.4a). While previous modeling studies (Cibot et al., 2005; Luo et al., 2003; Moon et al., 2007; Tatebe et al., 2013) and observational analysis (Luo and Yamagata, 2001) have suggested the critical role of the South Pacific in driving the phase transition of the TPDV, we highlight the larger contribution from the northern hemisphere than the southern part. This difference can be attributed to two main causes. Firstly, the use of shallower isopycnal levels in our analysis effectively captures the direct impact of subsurface anomalies on Niño4 surface temperature variability. This contrasts with previous studies based on deeper isopycnal levels (Cibot et al., 2005; Luo and Yamagata, 2001; Moon et al., 2007). Consequently, our framework aligns with the observed decadal time scale oscillation (Figure 3.2) rather than the approximately 14-year periods found in previous observational study (Luo and Yamagata, 2001). Secondly, our analysis is consistent with recent findings that the off-equatorial northwestern Pacific plays a more substantial role in the equatorial heat budget at the decadal time scale (Meehl et al., 2016; Meehl et al., 2021). Furthermore, the weaker signal in the southwestern Pacific might relate to the structure of the wind forcing. Specifically, the zonal coherency of the Ekman pumping has been proposed as the primary factor determining the low-frequency variability while local maxima of the forcing only affect the sharpness of the variability (Capotondi et al.,

2003). In Figure 3.5d, the northern off-equatorial Ekman pumping is elongated from around 130°W to the western boundary while the southern off-equatorial Ekman pumping is only extended from around 140°W to 150°E with the occurrence of a band of negative Ekman pumping centered around 10°S and 150°E. Therefore, the specific structure of the forcing might be a significant factor explaining the weaker signal from the South Pacific in the TPDV.

3.3.3 Overall TPDV framework

The decadal oscillation framework in the tropical Pacific can be summarized as follows:

a) Positive phase: strongest positive temperature anomalies in the Niño4 region (Figures 3.3a and 3.6a). Ensemble atmospheric modeling experiments with prescribed 2°C SST forcing further confirm that surface warming in the Niño4 region can induce cyclonic circulation in the northwestern and southwestern Pacific (Figure S3.12), respectively, leading to the corresponding positive and negative wind stress curl anomalies in the 2-15°N and 2-15°S latitudinal bands (Figures S3.4a and 3.5c). The resulting positive Ekman pumping (Figures S3.4b and 3.5d) drives negative subsurface temperature anomalies with the strongest signals in the off-equatorial northwestern Pacific (Figures 3.4a). This is also confirmed by the ensemble oceanic modeling experiments when TPDV-associated wind fields were prescribed (Figure S3.13).

b) Transition phase: Off-equatorial northwestern subsurface temperature anomalies gradually migrate toward the central basin along the NECC pathway (Figures S3.6 and S3.7). As the isopycnals shoal toward the east, negative subsurface temperature anomalies accumulated in the Niño4 region around three years later (Figures 3.3g, 3.4g, and 3.6b).

c) **Strengthening phase:** During the positive phase, in addition to the local ocean impacts, the Gill-type response of TPDV can further force extratropical atmospheric anomalies (around 3 months), driving the westward propagating oceanic Rossby waves that affect the KE system (around 2.5-3 years) (Andres et al., 2009; Ceballos et al., 2009; Taguchi et al., 2007). The change of the KE state then induces a downstream atmospheric response that projects onto the forcing pattern of the PMM (Gan et al., 2023) (Figures S3.5 and 3.6). The PMM further strengthens the subsurface anomalies in the central equatorial Pacific 0-12 months before the peak of the cold phase (Figures 3.3j-l and 3.6c).

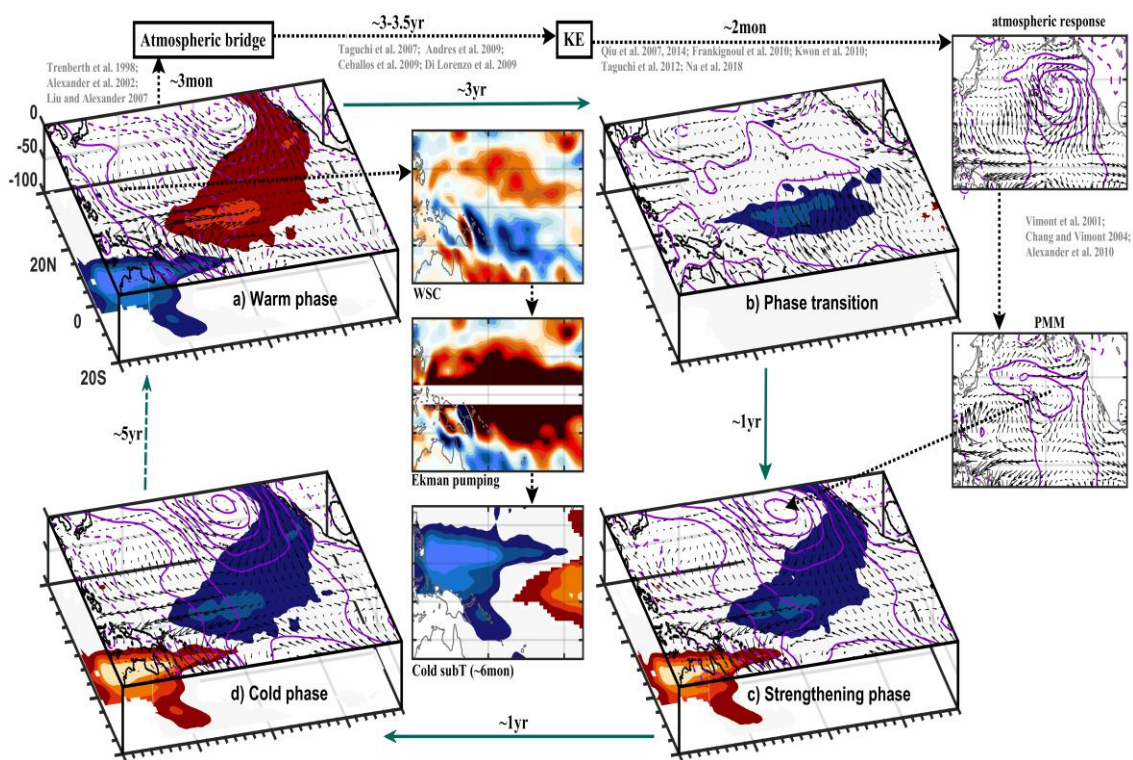
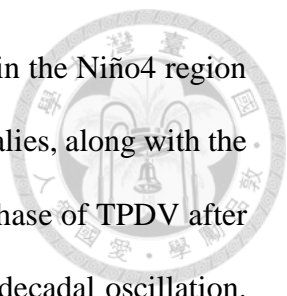


Figure 3.6 Framework for TPDV. (a) Warm phase of TPDV is characterized by the strongest surface warming in the Niño4 region, off-equatorial western Pacific Gill-response, strong subsurface cooling, and extratropical cyclonic circulation. (b) Surfacing of off-equatorial northwestern subsurface temperature anomalies in the Niño4 region. (c) PMM (with contributions from KE) enhances the subsurface-produced equatorial disturbance in the Niño4 region. (d) Similar to the warm phase but with the sign reversed.



d) Cold phase: The accumulation of subsurface temperature anomalies in the Niño4 region originated from the off-equatorial northwestern Pacific subsurface anomalies, along with the enhancement of the KE and thus PMM contribution, result in the cold phase of TPDV after around 5-6 years (Figures 3.3l and 3.6d), setting up a half cycle of the decadal oscillation. The remaining opposite cycle is simply the reverse of the processes mentioned above (Figure 3.6).

3.4 Summary and discussion

Based on available observational and reanalysis products and ensemble model experiments, this study presents a modified framework of TPDV involving off-equatorial subsurface temperature anomalies and extratropical-tropical ocean-atmosphere interaction. The combined contribution of off-equatorial subsurface temperature propagation and PMM eventually leads to the mature cold phase after five years. The center of equatorial negative SST anomalies then forces anomalous atmospheric circulation, resulting in positive subsurface temperature anomalies in the off-equatorial western area and potentially reversing the state of TPDV. Thus, a periodic oscillation of around 10 years is achieved.

TPDV-associated SST anomalies can induce extratropical anomalous wind fields, generating off-equatorial Rossby waves in both the North and South Pacific. These waves then propagate westward and may potentially contribute to the phase transition of TPDV (Meehl and Hu, 2006; Meehl et al., 2021). We show the temporal evolution of SSH anomalies along a specific circuit, westward along 13°N (Figure S3.8a), then equatorward along the western boundary at 130°E (Figure S3.8b), and eastward along the equator (Figure S3.8c). Most of the SSH anomalies originating west of 160°W appear to reach the western boundary at 13°N after 2-3 years (Figure S3.8a), then follow the western boundary to reach the

equatorial western Pacific (Figure S3.8b), and propagate eastward to the central basin along the equator at much-reduced amplitude (Figure S3.8c). Along the equator, we also observe the propagating SSH signals disconnect abruptly around 160°E, suggesting that off-equatorial Rossby waves might not be the primary contributor to the phase reversal of TPDV. Furthermore, a recent study postulated that robust ENSO events could potentially influence the phase transition of TPDV (Meehl et al., 2021). However, we have identified only two distinct ENSO events that could play a role in the phase transition of TPDV within the scope of our analysis: the 1965/66 El Niño and 2007/08 La Niña (Figure S3.8). The former may contribute to the transition from a negative to a positive phase, while the latter may contribute to the transition from a positive to a negative phase of TPDV. Nonetheless, a more comprehensive analysis is necessary to accurately quantify the degree to which ENSO events contribute to the phase transition of TPDV.

3.5 Supporting information

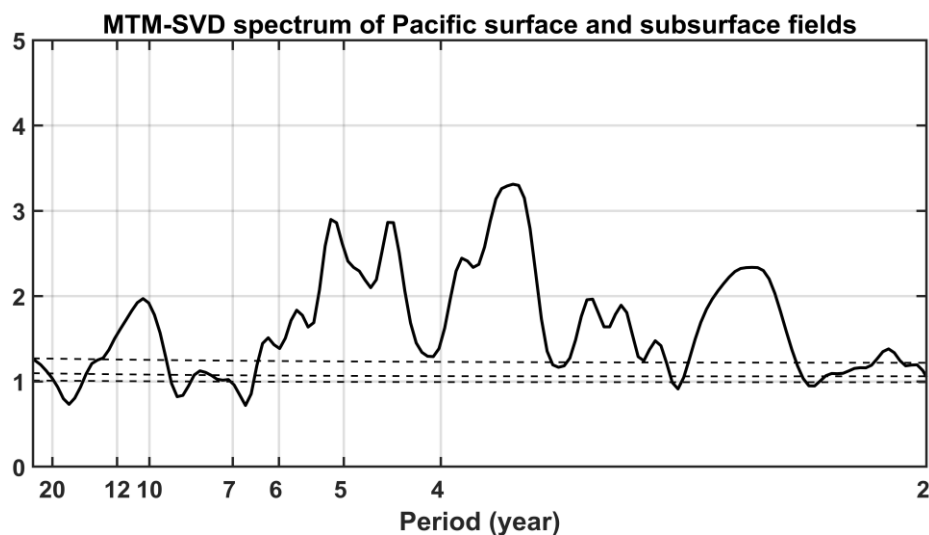


Figure S3.1 LFV spectrum for the combined raw detrended SST, SLP, 10-m wind, and subsurface temperature anomalies averaged between $22-24.5 \sigma_{\theta}$ and $24.5-26 \sigma_{\theta}$. The horizontal dashed lines are the 90%, 95% and 99% confidence levels based on the bootstrap method.

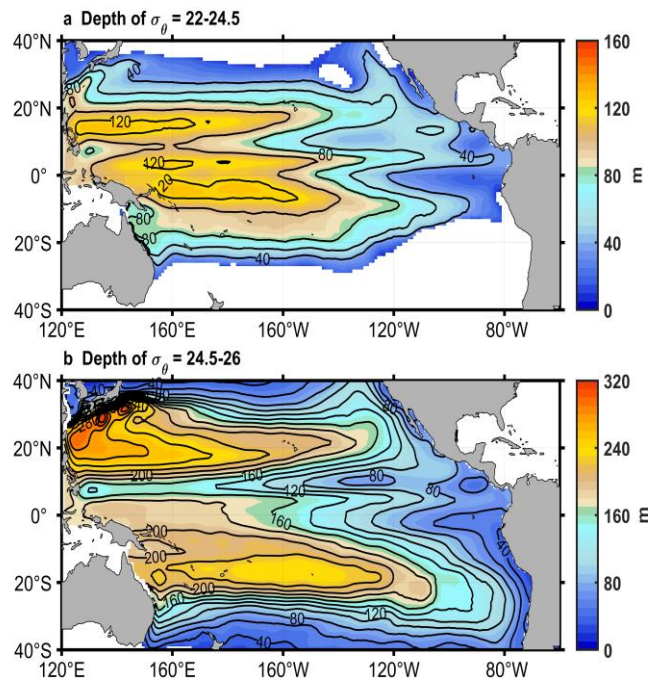


Figure S3.2 Mean depth of (a) 22-24.5 σ_θ and (b) 24.5-26 σ_θ from 1950 to 2021. The contour interval is 20 m.

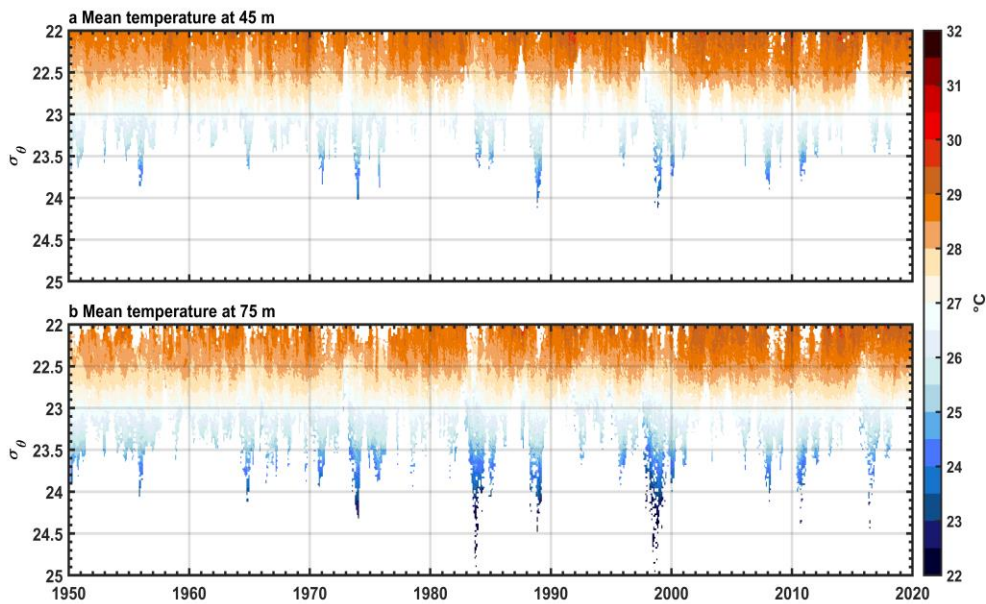


Figure S3.3 Mean temperature at (a) 45 m and (b) 75 m level averaged in the Niño4 region. Shown are all isopycnals between 22-25 σ_θ that intersect with these depth levels.

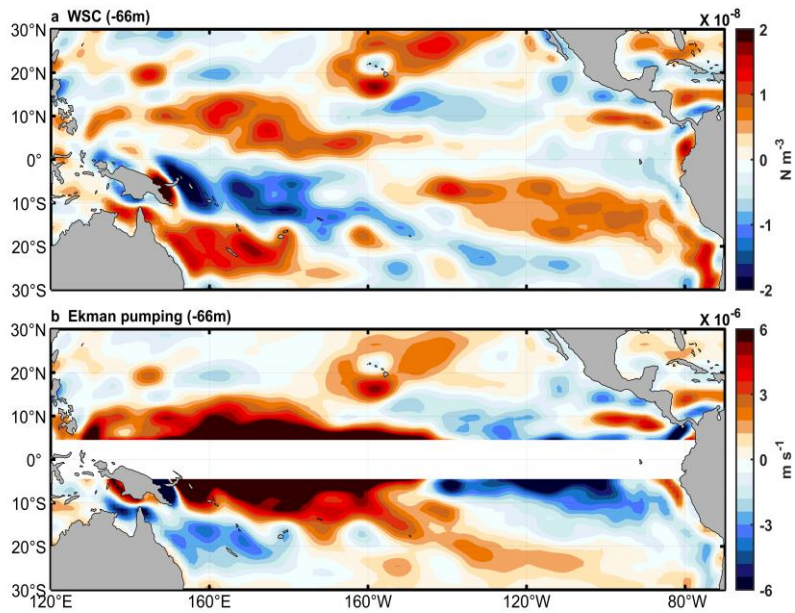


Figure S3.4 Same as **Figure 3.3a** but for (a) wind stress curl anomalies and (b) Ekman pumping.

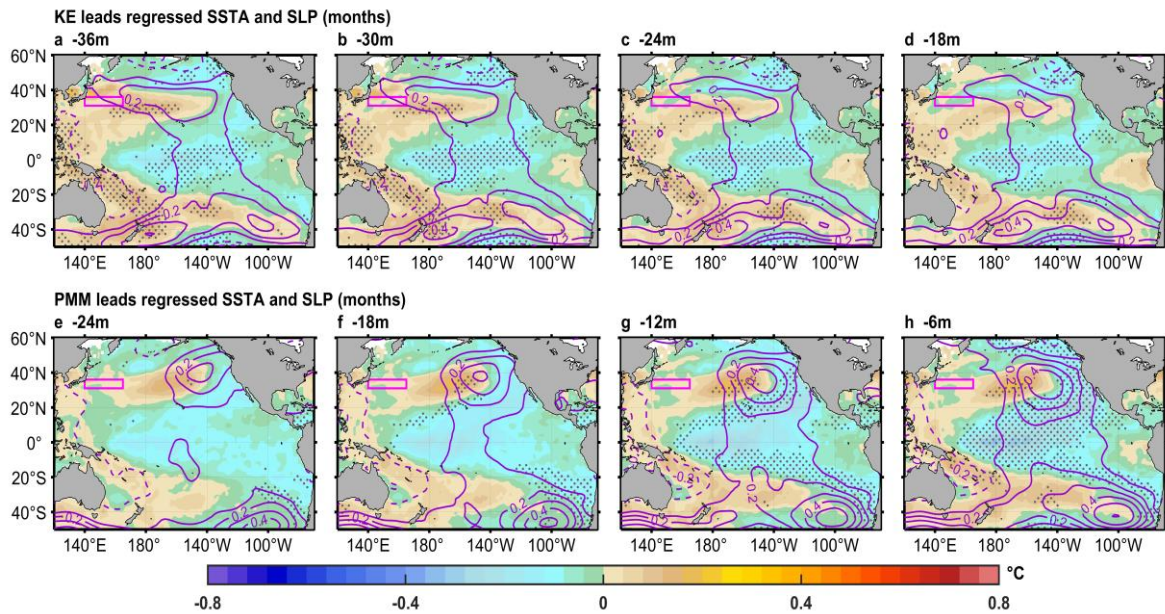


Figure S3.5 8-20-year bandpass filtered SST (shading) and SLP (contours, hPa) anomalies regressed with the 8-20-year bandpass filtered (a-d) KE index and (e-h) PMM SST index. The contour interval is 0.1 hPa (positive/negative is solid/dashed). Stipples indicate the regressed SST exceeding 95% confidence level with the random-phase test. Regressed SLP are shown as a whole for clarity. In all panels, the magenta rectangle indicates the KE region. The numbers indicate the KE and PMM index lead SST anomalies by months.

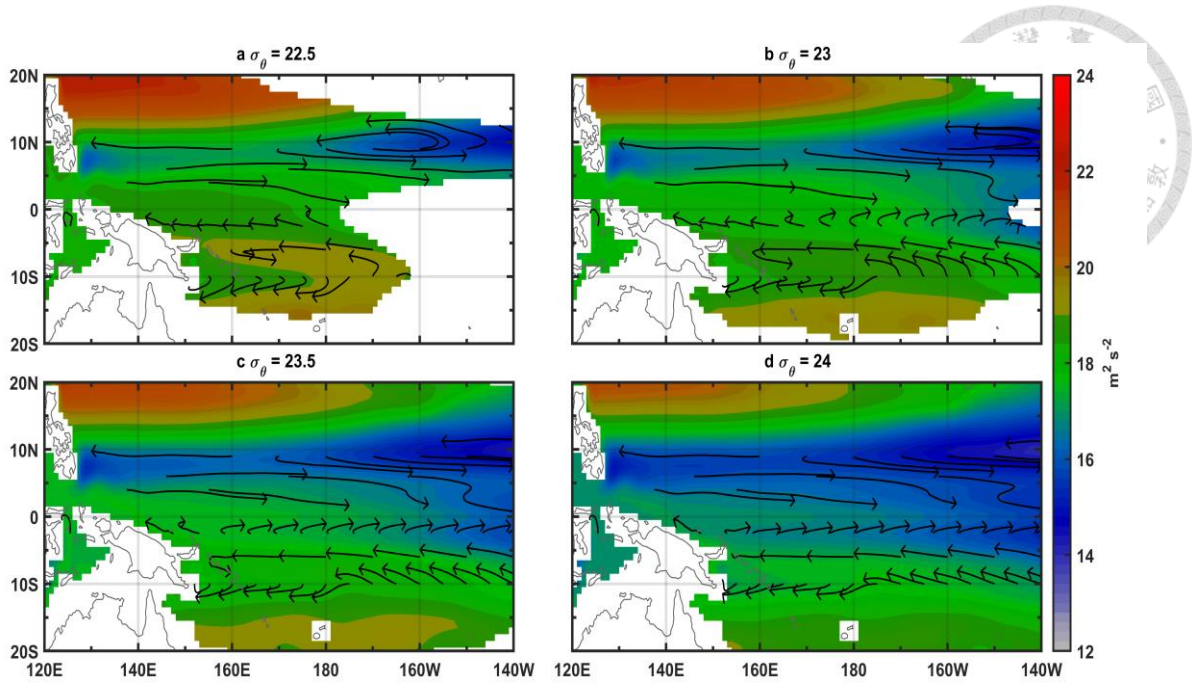


Figure S3.6 Mean acceleration potential (shading) referenced to 1000 dbar and mean current vectors evaluated on (a) $22.5 \sigma_\theta$, (b) $23 \sigma_\theta$, (c) $23.5 \sigma_\theta$ and (d) $24 \sigma_\theta$. Only some representative current vectors are shown. Current data is from GODAS during 1980-2021.

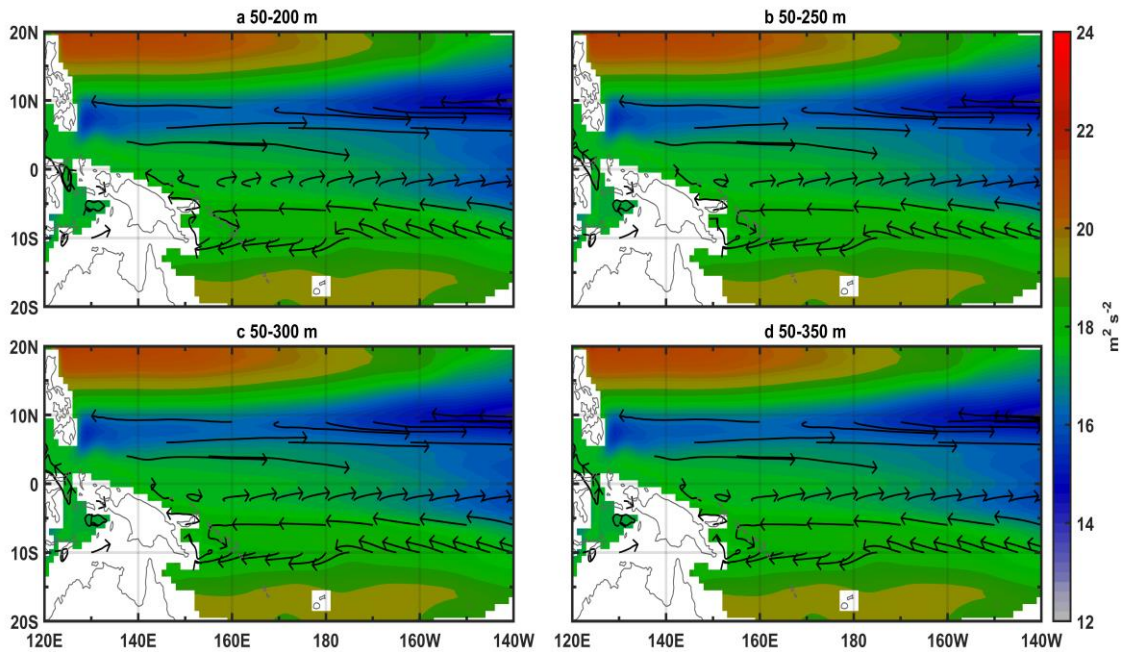


Figure S3.7 Mean acceleration potential (shading) referenced to 1000 dbar evaluated on $23.5 \sigma_\theta$ and mean depth-integrated current vectors. Only some representative current vectors are shown. Current data is from GODAS during 1980-2021.

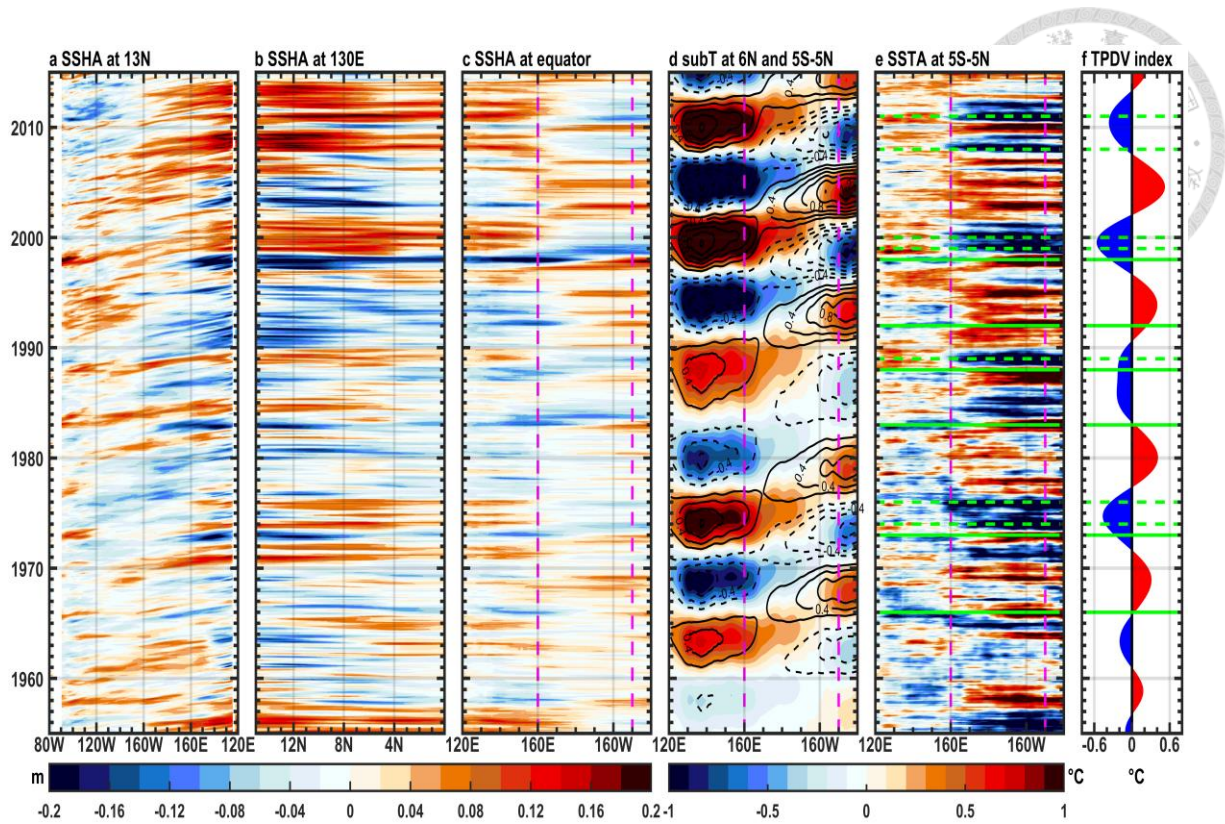


Figure S3.8 Hovmöller diagram of SSH anomalies along (a) 13°N (plotted from east to west), (b) 130°E (plotted north to south), and (c) equator (plotted from west to east). (d) Reconstructed subsurface temperature anomalies between 22-24.5 σ_θ using MTM-SVD averaged along 6°N (shading) and 5°S-5°N (contour). The contour interval is 0.2°C (positive/negative is solid/dashed). (e) SST anomalies averaged between 5°S-5°N. (f) TPDV index. The vertical dashed magenta lines indicate the longitude of 160°E and 150°W. The horizontal solid (dashed) green lines indicate strong and very strong El Niño (La Niña) events that peak in December based on the Oceanic Niño Index (ONI). All the data (a-c, e) are detrended and removed seasonal cycle only before plotting. SSH data is from GECCO3 (1948-2018).

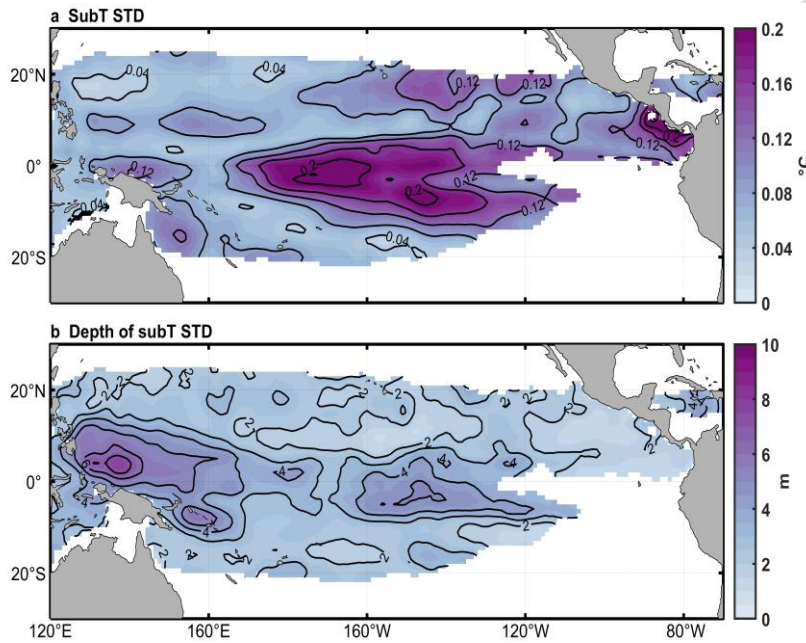


Figure S3.9 Standard deviation of the 8-20-year bandpass filtered (a) temperature and (b) depth anomalies averaged between 22-24.5 σ_θ .

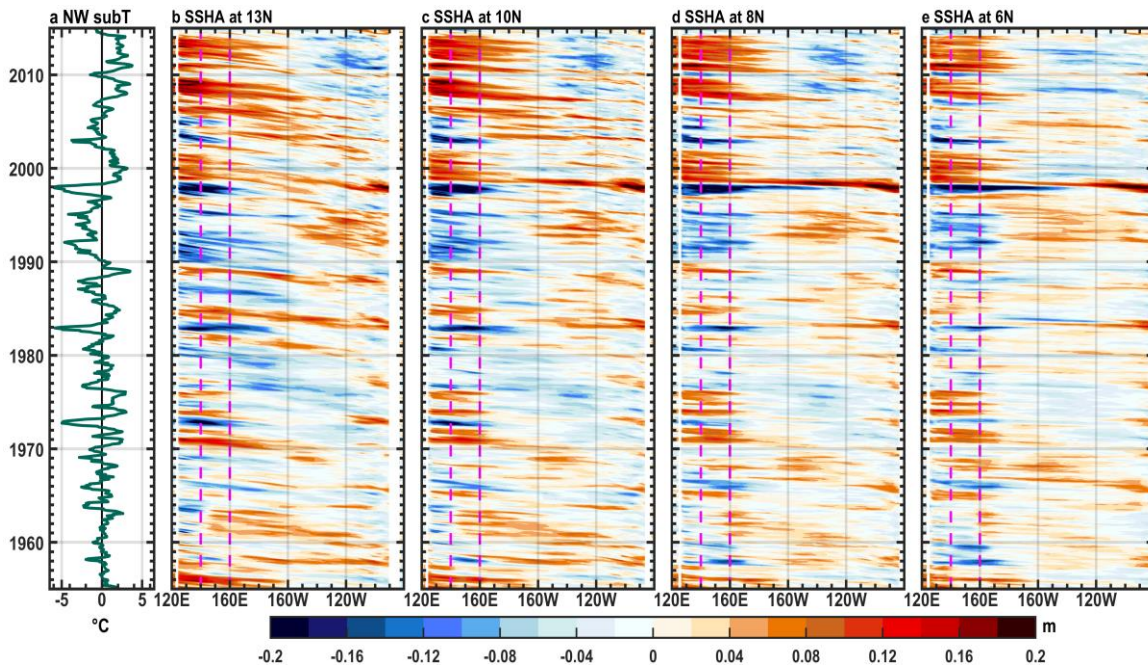


Figure S3.10 (a) Time series of subsurface temperature anomalies averaged in the NW box between 22-24.5 σ_θ . Hovmöller diagram of SSH anomalies along (b) 13°N, (c) 10°N, (d) 8°N and (e) 6°N. The vertical dashed magenta lines show the longitude of 140°E and 160°E. All the data are detrended and removed seasonal cycle only before plotting. SSH data is from GECCO3 (1948-2018).

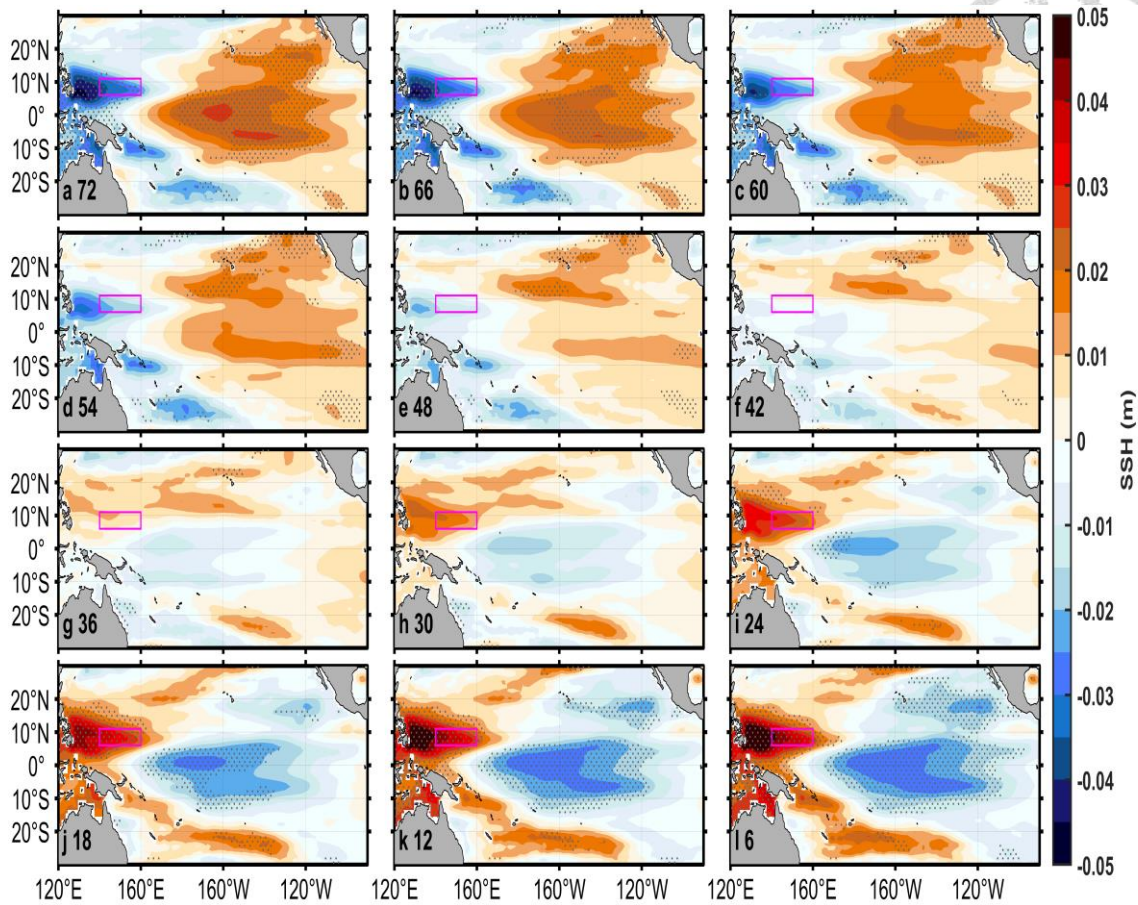


Figure S3.11 8-20 year bandpass filtered SSH anomalies regressed with the 8-20 year bandpass filtered temperature anomalies averaged between $22-24.5 \sigma_\theta$ in NW box (magenta rectangle). Numbers in each panel indicate SSH anomalies lead subsurface temperature by months. Stipples indicate the region exceeding 95% confidence level with the random-phase test.

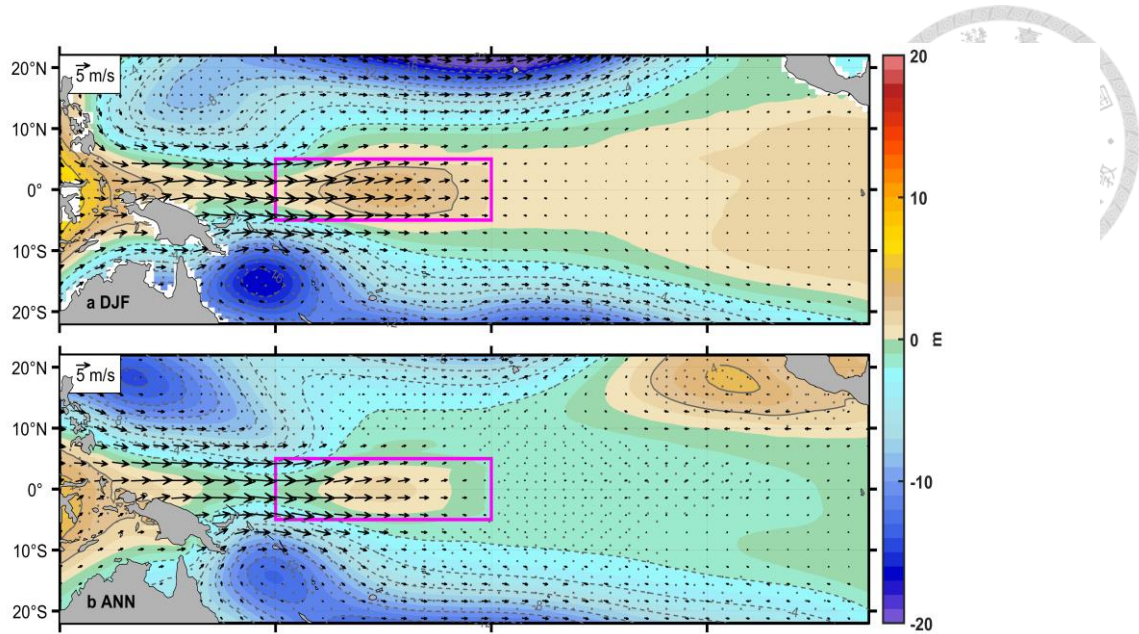


Figure S3.12 (a) Wintertime (December-February) and (b) annual response of 850 hPa geopotential height (shading and contour) and 850 hPa winds with specified 2°C SST anomalies imposed in the magenta rectangle region shown in (a). Stipple indicates 95% significance level based on a Student's t-test.

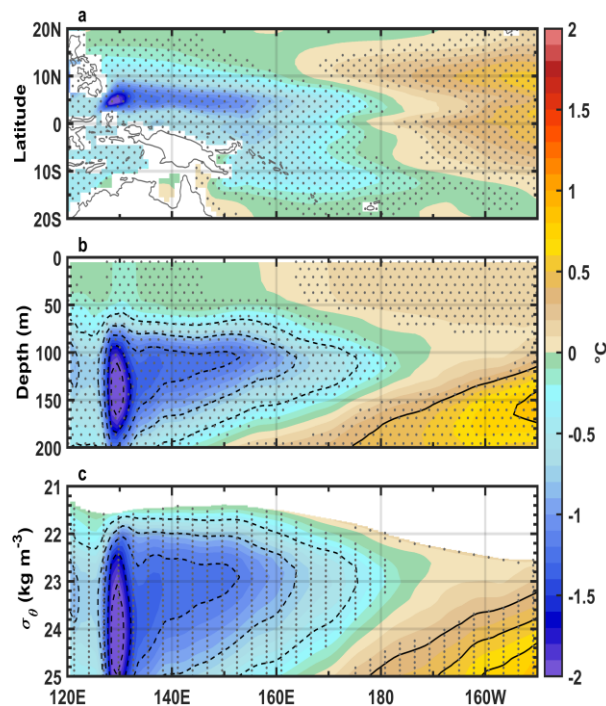


Figure S3.13 (a) Annual horizontal response structure of temperature averaged between 22-24.5 σ_θ to the superimposed anomalous wind fields associated with the positive phase of the TPDV. Same as (a) but for (b) longitude-depth and (c) longitude- σ_θ plot of the response of temperature at 6°N. Stipple indicates 95% significance level based on a Student's t-test.



Chapter 4

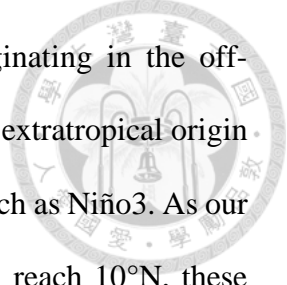
Discussion and conclusions

4.1 Summary

In Chapter 2, employing CEOF analysis of observational and reanalysis datasets, we demonstrate the existence of a decadal subsurface spiciness propagating mode in the North Pacific. This mode is characterized by a dipole pattern with opposite signs in the midlatitude and subtropics, driven by net surface heat flux changes and anomalous subsurface currents associated with Aleutian Low/PDO. We then show the propagation characteristics of this spiciness mode: the anomaly of midlatitude origin can be traced to 14°N while the anomaly originating in the subtropics can extend as far as 10°N. Moreover, tropical SST forcing is also found to contribute to the formation of the spiciness mode.

In Chapter 3, we utilized MTM-SVD analysis of joint atmospheric and oceanic fields, along with model experiments, to demonstrate the pivotal role of tropical subsurface temperature anomalies in TPDV. Specifically, the propagation of off-equatorial northwestern Pacific temperature anomalies along the NECC pathway toward the Niño4 region serves as the most critical water source for the phase reversal of TPDV. We also show that KE can only explain a small fraction of decadal variance while PMM contributes significantly to the growth of the equatorial disturbance 0-12 months before the TPDV peak phase, consistent with previous studies (Di Lorenzo et al., 2015; Zhao and Di Lorenzo, 2020). Finally, by combining off-equatorial subsurface temperature anomalies, KE, and PMM, we provide a comprehensive framework for TPDV.

4.2 Discussion

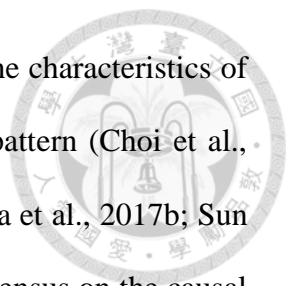


Although we have identified the key water source for TPDV originating in the off-equatorial northwestern Pacific, it remains an open question whether the extratropical origin of subsurface spiciness anomalies can impact other equatorial regions, such as Niño3. As our findings indicate that the subtropical origin of spiciness anomalies can reach 10°N, these anomalies may approach the Niño3 region as the isopycnal shallows toward the eastern basin. Additionally, previous studies have suggested that spiciness anomalies from the Southern Hemisphere can propagate toward the tropics more effectively than their northern counterpart. While our study focuses on the North Pacific, it is plausible that the South Pacific may have a significant impact on the equatorial eastern basin.

Given the pivotal role of off-equatorial subsurface temperature anomalies in the phase reversal of TPDV, well-initialized oceanic conditions (Meehl et al., 2016) could significantly enhance TPDV predictability. Furthermore, the study suggests the need for a more robust observational system, particularly in the off-equatorial northwestern Pacific. Such a system could furnish valuable information about the phase transition of TPDV.

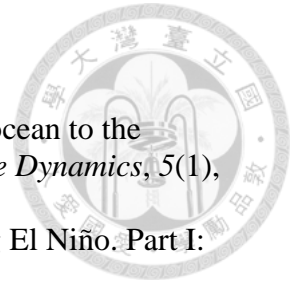
4.3 Future work

The tropical Pacific is dominated not only by ENSO at interannual time scales but also by TPDV at decadal time scales. This raises the question of whether connections exist between TPDV and ENSO or if they operate independently. Previous studies have suggested possible interactive feedback between ENSO and TPDV (Choi and An, 2013; Choi et al., 2009; Choi et al., 2012; Choi et al., 2013; Imada and Kimoto, 2009; Kiem et al., 2003; Ogata et al., 2013; Okumura et al., 2017b; Sun and Yu, 2009; Yeh and Kirtman, 2004). Specifically, some investigations proposed that decadal variability in ENSO activities and associated mean state changes can contribute to TPDV (Choi et al., 2009; Choi et al., 2012; Rodgers et al., 2004).



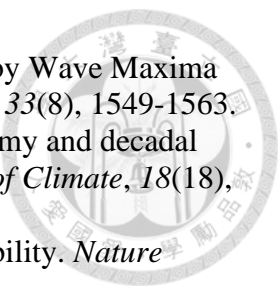
On the other hand, studies have demonstrated that TPDV may impact the characteristics of ENSO events in terms of amplitude, frequency, duration, and spatial pattern (Choi et al., 2011; Hasegawa and Hanawa, 2006; Imada and Kimoto, 2009; Okumura et al., 2017b; Sun and Okumura, 2020; Zhong et al., 2017). However, there is still no consensus on the causal relationship and the underlying mechanisms of the relationship, if it exists, between ENSO and TPDV. Moreover, ENSO is projected to undergo substantial changes in response to global warming (Cai et al., 2021; Geng et al., 2022), while TPDV is suggested to play a significant role in shaping low-frequency global climate variability (Kosaka and Xie, 2013; Watanabe et al., 2014). Therefore, gaining a better understanding of the relationship between TPDV and ENSO, and how the relationship may change under a warming scenario is crucial for both short-term and long-term climate prediction.

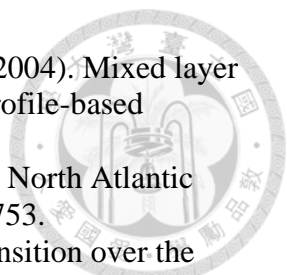
Another issue that warrants attention pertains to the formation of PMM during the TPDV transition stage. While KE can partially explain the forcing of PMM, it remains uncertain whether PMM is further influenced by factors within and/or outside the Pacific. Zhang et al. (2021) demonstrated that the decadal PMM is primarily driven by a tripole mode pattern of SLP anomalies extending from northeastern Asia to the northeastern Pacific. In contrast, Sun et al. (2017) suggested that the positive phase of the Atlantic Multidecadal Oscillation can weaken the Aleutian Low via atmospheric teleconnection, thereby contributing to PMM. Further investigations are needed to discern the fraction of decadal variability of PMM driven by intra-basin factors versus inter-basin factors. Moreover, a critical aspect to explore is how these physical processes activate the preferred decadal time-scale variability of PMM.

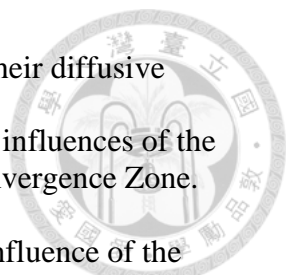


References

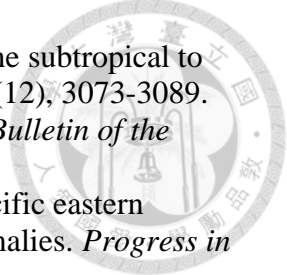
- Alexander MA (1990). Simulation of the response of the North Pacific ocean to the anomalous atmospheric circulation associated with El Niño. *Climate Dynamics*, 5(1), 53-65.
- Alexander MA (1992). Midlatitude atmosphere-ocean interaction during El Niño. Part I: The North Pacific ocean. *Journal of Climate*, 5(9), 944-958.
- Alexander MA, Bladé I, Newman M, Lanzante JR, Lau N-C, and Scott JD (2002). The Atmospheric Bridge: The Influence of ENSO Teleconnections on Air–Sea Interaction over the Global Oceans. *Journal of Climate*, 15(16), 2205-2231.
- Alexander MA, and Deser C (1995). A mechanism for the recurrence of wintertime midlatitude SST anomalies. *Journal of Physical Oceanography*, 25(1), 122-137.
- Alexander MA, Vimont DJ, Chang P, and Scott JD (2010). The Impact of Extratropical Atmospheric Variability on ENSO: Testing the Seasonal Footprinting Mechanism Using Coupled Model Experiments. *Journal of Climate*, 23(11), 2885-2901.
- Amaya DJ, Miller AJ, Xie S-P, and Kosaka Y (2020). Physical drivers of the summer 2019 North Pacific marine heatwave. *Nature Communications*, 11(1), 1903.
- Andres M, Park J-H, Wimbush M, Zhu X-H, Nakamura H, Kim K, and Chang K-I (2009). Manifestation of the Pacific Decadal Oscillation in the Kuroshio. *Geophysical Research Letters*, 36(16).
- Ashok K, Behera SK, Rao SA, Weng H, and Yamagata T (2007). El Niño Modoki and its possible teleconnection. *Journal of Geophysical Research: Oceans*, 112(C11).
- Barnett TP (1983). Interaction of the monsoon and Pacific trade wind system at interannual time scales Part I: The equatorial zone. *Monthly Weather Review*, 111(4), 756-773.
- Barnett TP, Pierce DW, Latif M, Dommenges D, and Saravanan R (1999). Interdecadal interactions between the tropics and midlatitudes in the Pacific Basin. *Geophysical Research Letters*, 26(5), 615-618.
- Behringer DW, Ji M, and Leetmaa A (1998). An Improved Coupled Model for ENSO Prediction and Implications for Ocean Initialization. Part I: The Ocean Data Assimilation System. *Monthly Weather Review*, 126(4), 1013-1021.
- Behringer DW, and Xue Y (2004). Evaluation of the Global Ocean Data Assimilation System at NCEP: The Pacific Ocean, edited.
- Bjerknes J (1964). Atlantic Air-Sea Interaction, in *Advances in Geophysics*, edited by H. E. Landsberg and J. Van Mieghem, pp. 1-82, Elsevier.
- Bond NA, Cronin MF, Freeland H, and Mantua N (2015). Causes and impacts of the 2014 warm anomaly in the NE Pacific. *Geophysical Research Letters*, 42(9), 3414-3420.
- Bond NA, Overland JE, Spillane M, and Stabeno P (2003). Recent shifts in the state of the North Pacific. *Geophysical Research Letters*, 30(23).
- Byrne MP, Pendergrass AG, Rapp AD, and Wodzicki KR (2018). Response of the Intertropical Convergence Zone to Climate Change: Location, Width, and Strength. *Current Climate Change Reports*, 4(4), 355-370.
- Cai W, et al. (2021). Changing El Niño–Southern Oscillation in a warming climate. *Nature Reviews Earth & Environment*, 2(9), 628-644.
- Cai W, et al. (2019). Pantropical climate interactions. *Science*, 363(6430), eaav4236.
- Capotondi A, and Alexander MA (2001). Rossby Waves in the Tropical North Pacific and Their Role in Decadal Thermocline Variability. *Journal of Physical Oceanography*, 31(12), 3496-3515.

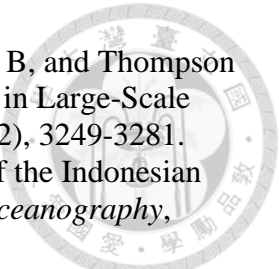
- 
- Capotondi A, Alexander MA, and Deser C (2003). Why Are There Rossby Wave Maxima in the Pacific at 10°S and 13°N? *Journal of Physical Oceanography*, 33(8), 1549-1563.
- Capotondi A, Alexander MA, Deser C, and McPhaden MJ (2005). Anatomy and decadal evolution of the Pacific Subtropical-Tropical Cells (STCs). *Journal of Climate*, 18(18), 3739-3758.
- Capotondi A, et al. (2023). Mechanisms of tropical Pacific decadal variability. *Nature Reviews Earth & Environment*, 4(11), 754-769.
- Capotondi A, Newman M, Xu T, and Di Lorenzo E (2022). An Optimal Precursor of Northeast Pacific Marine Heatwaves and Central Pacific El Niño Events. *Geophysical Research Letters*, 49(5), e2021GL097350.
- Capotondi A, and Qiu B (2022). Decadal Variability of the Pacific Shallow Overturning Circulation and the Role of Local Wind Forcing. *Journal of Climate*, 1-34.
- Capotondi A, Wittenberg AT, Kug J-S, Takahashi K, and McPhaden MJ (2020), ENSO Diversity, in *El Niño Southern Oscillation in a Changing Climate*, edited, pp. 65-86.
- Ceballos LI, Di Lorenzo E, Hoyos CD, Schneider N, and Taguchi B (2009). North Pacific Gyre Oscillation Synchronizes Climate Fluctuations in the Eastern and Western Boundary Systems. *Journal of Climate*, 22(19), 5163-5174.
- Chen H-C, Sui C-H, Tseng Y-H, and Huang B (2015). An analysis of the linkage of Pacific subtropical cells with the recharge-discharge processes in ENSO evolution. *Journal of Climate*, 28(9), 3786-3805.
- Chen X, and Wallace JM (2015). ENSO-Like Variability: 1900–2013. *Journal of Climate*, 28(24), 9623-9641.
- Cheng W, McPhaden MJ, Zhang D, and Metzger EJ (2007). Recent Changes in the Pacific Subtropical Cells Inferred from an Eddy-Resolving Ocean Circulation Model. *Journal of Physical Oceanography*, 37(5), 1340-1356.
- Chiang JCH, and Vimont DJ (2004). Analogous Pacific and Atlantic Meridional Modes of Tropical Atmosphere–Ocean Variability. *Journal of Climate*, 17(21), 4143-4158.
- Choi J, and An S-I (2013). Quantifying the residual effects of ENSO on low-frequency variability in the tropical Pacific. *International Journal of Climatology*, 33(4), 1047-1052.
- Choi J, An S-I, Dewitte B, and Hsieh WW (2009). Interactive Feedback between the Tropical Pacific Decadal Oscillation and ENSO in a Coupled General Circulation Model. *Journal of Climate*, 22(24), 6597-6611.
- Choi J, An S-I, Kug J-S, and Yeh S-W (2011). The role of mean state on changes in El Niño's flavor. *Climate Dynamics*, 37(5), 1205-1215.
- Choi J, An S-I, and Yeh S-W (2012). Decadal amplitude modulation of two types of ENSO and its relationship with the mean state. *Climate Dynamics*, 38(11), 2631-2644.
- Choi J, An S-I, Yeh S-W, and Yu J-Y (2013). ENSO-Like and ENSO-Induced Tropical Pacific Decadal Variability in CGCMs. *Journal of Climate*, 26(5), 1485-1501.
- Chunhan J, Bin W, and Jian L (2021). Emerging Pacific Quasi-Decadal Oscillation Over the Past 70 Years. *Geophysical Research Letters*, 48(2), e2020GL090851.
- Cibot C, Maisonnave E, Terray L, and Dewitte B (2005). Mechanisms of tropical Pacific interannual-to-decadal variability in the ARPEGE/ORCA global coupled model. *Climate Dynamics*, 24(7), 823-842.
- Collins M, et al. (2010). The impact of global warming on the tropical Pacific Ocean and El Niño. *Nature Geoscience*, 3(6), 391-397.

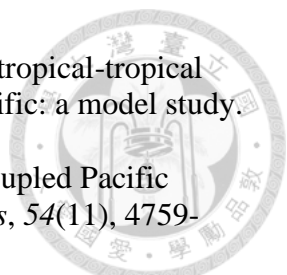
- 
- de Boyer Montégut C, Madec G, Fischer AS, Lazar A, and Iudicone D (2004). Mixed layer depth over the global ocean: An examination of profile data and a profile-based climatology. *Journal of Geophysical Research: Oceans*, 109(C12).
- Deser C, and Blackmon ML (1993). Surface Climate Variations over the North Atlantic Ocean during Winter: 1900–1989. *Journal of Climate*, 6(9), 1743-1753.
- Deser C, and Phillips AS (2006). Simulation of the 1976/77 Climate Transition over the North Pacific: Sensitivity to Tropical Forcing. *Journal of Climate*, 19(23), 6170-6180.
- Di Lorenzo E, Liguori G, Schneider N, Furtado JC, Anderson BT, and Alexander MA (2015). ENSO and meridional modes: A null hypothesis for Pacific climate variability. *Geophysical Research Letters*, 42(21), 9440-9448.
- Di Lorenzo E, and Mantua N (2016). Multi-year persistence of the 2014/15 North Pacific marine heatwave. *Nature Climate Change*, 6(11), 1042-1047.
- Di Lorenzo E, et al. (2008). North Pacific Gyre Oscillation links ocean climate and ecosystem change. *Geophysical Research Letters*, 35(8).
- Di Lorenzo E, et al. (2023). Modes and Mechanisms of Pacific Decadal-Scale Variability. *Annual Review of Marine Science*, 15(1), 249-275.
- Ding R, Li J, Tseng Y-h, and Ruan C (2015a). Influence of the North Pacific Victoria mode on the Pacific ITCZ summer precipitation. *Journal of Geophysical Research: Atmospheres*, 120(3), 964-979.
- Ding R, Li J, Tseng Y-h, Sun C, and Guo Y (2015b). The Victoria mode in the North Pacific linking extratropical sea level pressure variations to ENSO. *Journal of Geophysical Research: Atmospheres*, 120(1), 27-45.
- Dong L, and McPhaden MJ (2017). Why Has the Relationship between Indian and Pacific Ocean Decadal Variability Changed in Recent Decades? *Journal of Climate*, 30(6), 1971-1983.
- Duchon CE (1979). Lanczos Filtering in One and Two Dimensions. *Journal of Applied Meteorology and Climatology*, 18(8), 1016-1022.
- Ebisuzaki W (1997). A Method to Estimate the Statistical Significance of a Correlation When the Data Are Serially Correlated. *Journal of Climate*, 10(9), 2147-2153.
- England MH, McGregor S, Spence P, Meehl GA, Timmermann A, Cai W, Gupta AS, McPhaden MJ, Purich A, and Santoso A (2014). Recent intensification of wind-driven circulation in the Pacific and the ongoing warming hiatus. *Nature Climate Change*, 4(3), 222-227.
- Fang J, and Yang X-Q (2016). Structure and dynamics of decadal anomalies in the wintertime midlatitude North Pacific ocean–atmosphere system. *Climate Dynamics*, 47(5), 1989-2007.
- Farneti R, Dwivedi S, Kucharski F, Molteni F, and Griffies SM (2014a). On Pacific Subtropical Cell Variability over the Second Half of the Twentieth Century. *Journal of Climate*, 27(18), 7102-7112.
- Farneti R, Molteni F, and Kucharski F (2014b). Pacific interdecadal variability driven by tropical–extratropical interactions. *Climate Dynamics*, 42(11), 3337-3355.
- Fedorov AV, and Philander SG (2000). Is El Niño Changing? *Science*, 288(5473), 1997-2002.
- Fine RA, Peterson WH, and Ostlund HG (1987). The penetration of tritium into the tropical Pacific. *Journal of Physical Oceanography*, 17(5), 553-564.

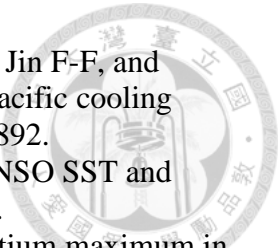
- 
- Flament P (2002). A state variable for characterizing water masses and their diffusive stability: spiciness. *Progress in Oceanography*, 54(1), 493-501.
- Folland CK, Renwick JA, Salinger MJ, and Mullan AB (2002). Relative influences of the Interdecadal Pacific Oscillation and ENSO on the South Pacific Convergence Zone. *Geophysical Research Letters*, 29(13), 21-21-21-24.
- Frankignoul C, Sennéchal N, Kwon Y-O, and Alexander MA (2011). Influence of the Meridional Shifts of the Kuroshio and the Oyashio Extensions on the Atmospheric Circulation. *Journal of Climate*, 24(3), 762-777.
- Frölicher TL, Fischer EM, and Gruber N (2018). Marine heatwaves under global warming. *Nature*, 560(7718), 360-364.
- Fukumori I, Lee T, Cheng B, and Menemenlis D (2004). The origin, pathway, and destination of Niño-3 water estimated by a simulated passive tracer and its adjoint. *Journal of Physical Oceanography*, 34(3), 582-604.
- Furue R, et al. (2015). Impacts of regional mixing on the temperature structure of the equatorial Pacific ocean. Part 1: Vertically uniform vertical diffusion. *Ocean Modelling*, 91, 91-111.
- Galanti E, and Tziperman E (2003). A Midlatitude–ENSO Teleconnection Mechanism via Baroclinically Unstable Long Rossby Waves. *Journal of Physical Oceanography*, 33(9), 1877-1888.
- Gan B, Wang T, Wu L, Li J, Qiu B, Yang H, and Zhang L (2023). A Mesoscale Ocean–Atmosphere Coupled Pathway for Decadal Variability of the Kuroshio Extension System. *Journal of Climate*, 36(2), 485-510.
- Geng T, et al. (2022). Emergence of changing Central-Pacific and Eastern-Pacific El Niño–Southern Oscillation in a warming climate. *Nature Communications*, 13(1), 6616.
- Giamalaki K, Beaulieu C, Henson SA, Martin AP, Kassem H, and Faranda D (2021). Future intensification of extreme Aleutian low events and their climate impacts. *Scientific Reports*, 11(1), 18395.
- Giese BS, Urizar SC, and Fučkar NS (2002). Southern Hemisphere origins of the 1976 climate shift. *Geophysical Research Letters*, 29(2), 1-1-1-4.
- Good SA, Martin MJ, and Rayner NA (2013). EN4: Quality controlled ocean temperature and salinity profiles and monthly objective analyses with uncertainty estimates. *Journal of Geophysical Research: Oceans*, 118(12), 6704-6716.
- Goodman PJ, Hazeleger W, de Vries P, and Cane M (2005). Pathways into the Pacific equatorial undercurrent: A trajectory analysis. *Journal of Physical Oceanography*, 35(11), 2134-2151.
- Graffino G, Farneti R, Kucharski F, and Molteni F (2019). The Effect of Wind Stress Anomalies and Location in Driving Pacific Subtropical Cells and Tropical Climate. *Journal of Climate*, 32(5), 1641-1660.
- Graham NE (1994). Decadal-scale climate variability in the tropical and North Pacific during the 1970s and 1980s: observations and model results. *Climate Dynamics*, 10(3), 135-162.
- Grinsted A, Moore JC, and Jevrejeva S (2004). Application of the cross wavelet transform and wavelet coherence to geophysical time series. *Nonlin. Processes Geophys.*, 11(5/6), 561-566.
- Gu D, and Philander SGH (1997). Interdecadal climate fluctuations that depend on exchanges between the tropics and extratropics. *Science*, 275(5301), 805-807.

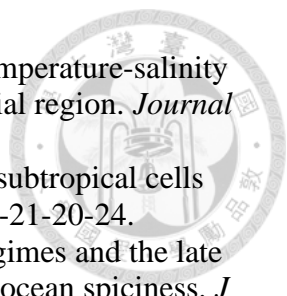
- 
- Han W, et al. (2014). Intensification of decadal and multi-decadal sea level variability in the western tropical Pacific during recent decades. *Climate Dynamics*, 43(5), 1357-1379.
- Hare SR, and Mantua NJ (2000). Empirical evidence for North Pacific regime shifts in 1977 and 1989. *Progress in Oceanography*, 47(2), 103-145.
- Hasegawa T, and Hanawa K (2006). Impact of quasi-decadal variability in the tropical Pacific on ENSO modulations. *Journal of Oceanography*, 62(2), 227-234.
- Hasselmann K (1976). Stochastic climate models Part I. Theory. *Tellus*, 28(6), 473-485.
- Hazeleger W, Visbeck M, Cane M, Karspeck A, and Naik N (2001). Decadal upper ocean temperature variability in the tropical Pacific. *Journal of Geophysical Research: Oceans*, 106(C5), 8971-8988.
- Hersbach H, et al. (2020). The ERA5 global reanalysis. *Quarterly Journal of the Royal Meteorological Society*, 146(730), 1999-2049.
- Horel JD (1984). Complex principal component analysis: Theory and examples. *Journal of Applied Meteorology and Climatology*, 23(12), 1660-1673.
- Hosoda S, Ohira T, and Nakamura T (2008). A monthly mean dataset of global oceanic temperature and salinity derived from Argo float observations. *JAMSTEC Report of Research and Development*, 8, 47-59.
- Hsu H-H, and Chen Y-L (2011). Decadal to bi-decadal rainfall variation in the western Pacific: A footprint of South Pacific decadal variability? *Geophysical Research Letters*, 38(3).
- Hu Z-Z, Kumar A, Jha B, Zhu J, and Huang B (2017). Persistence and predictions of the remarkable warm anomaly in the northeastern Pacific ocean during 2014-16. *Journal of Climate*, 30(2), 689-702.
- Huang RX (2011). Defining the spicity. *Journal of Marine Research*, 69(4-6), 545-559.
- Huang RX, Yu LS, and Zhou SQ (2018). New definition of potential spicity by the least square method. *Journal of Geophysical Research: Oceans*, 123(10), 7351-7365.
- Huang RX, Yu LS, and Zhou SQ (2021). Quantifying climate signals: Spicity, orthogonality, and distance. *Journal of Geophysical Research: Oceans*, 126(2).
- Imada Y, and Kimoto M (2009). ENSO amplitude modulation related to Pacific decadal variability. *Geophysical Research Letters*, 36(3).
- Imada Y, Tatebe H, Watanabe M, Ishii M, and Kimoto M (2016). South Pacific influence on the termination of El Niño in 2014. *Scientific Reports*, 6(1), 30341.
- Jackett DR, and Mcdougall TJ (1985). An oceanographic variable for the characterization of intrusions and water masses. *Deep Sea Research Part A. Oceanographic Research Papers*, 32(10), 1195-1207.
- Jin F-F (1997). An Equatorial Ocean Recharge Paradigm for ENSO. Part I: Conceptual Model. *Journal of the Atmospheric Sciences*, 54(7), 811-829.
- Jin F-F, Kimoto M, and Wang X (2001). A model of decadal ocean-atmosphere interaction in the North Pacific Basin. *Geophysical Research Letters*, 28(8), 1531-1534.
- Joh Y, and Di Lorenzo E (2017). Increasing coupling between NPGO and PDO leads to prolonged marine heatwaves in the northeast Pacific. *Geophysical Research Letters*, 44(22), 11,663-611,671.
- Joh Y, and Di Lorenzo E (2019). Interactions between Kuroshio Extension and Central Tropical Pacific lead to preferred decadal-timescale oscillations in Pacific climate. *Scientific Reports*, 9(1), 13558.

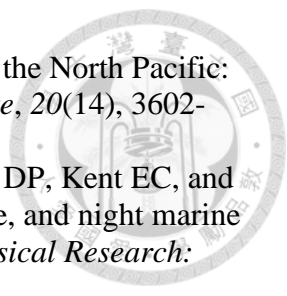
- 
- Johnson GC, and McPhaden MJ (1999). Interior pycnocline flow from the subtropical to the equatorial Pacific ocean. *Journal of Physical Oceanography*, 29(12), 3073-3089.
- Kalnay E, et al. (1996). The NCEP/NCAR 40-Year Reanalysis Project. *Bulletin of the American Meteorological Society*, 77(3), 437-472.
- Katsura S (2018). Properties, formation, and dissipation of the North Pacific eastern subtropical mode water and its impact on interannual spiciness anomalies. *Progress in Oceanography*, 162, 120-131.
- Kiem AS, Franks SW, and Kuczera G (2003). Multi-decadal variability of flood risk. *Geophysical Research Letters*, 30(2).
- Kilpatrick T, Schneider N, and Di Lorenzo E (2011). Generation of low-frequency spiciness variability in the thermocline. *Journal of Physical Oceanography*, 41(2), 365-377.
- Kim G-I, and Kug J-S (2020). Tropical Pacific Decadal Variability Induced by Nonlinear Rectification of El Niño–Southern Oscillation. *Journal of Climate*, 33(17), 7289-7302.
- Kleeman R, McCreary Jr. JP, and Klinger BA (1999). A mechanism for generating ENSO decadal variability. *Geophysical Research Letters*, 26(12), 1743-1746.
- Klinger BA, McCreary JP, and Kleeman R (2002). The Relationship between Oscillating Subtropical Wind Stress and Equatorial Temperature. *Journal of Physical Oceanography*, 32(5), 1507-1521.
- Knutson TR, and Manabe S (1998). Model Assessment of Decadal Variability and Trends in the Tropical Pacific Ocean. *Journal of Climate*, 11(9), 2273-2296.
- Köhl A (2020). Evaluating the GECCO3 1948–2018 ocean synthesis – a configuration for initializing the MPI-ESM climate model. *Quarterly Journal of the Royal Meteorological Society*, 146(730), 2250-2273.
- Kolodziejczyk N, and Gaillard F (2012). Observation of spiciness interannual variability in the Pacific pycnocline. *Journal of Geophysical Research: Oceans*, 117.
- Kolodziejczyk N, and Gaillard F (2013). Variability of the Heat and Salt Budget in the Subtropical Southeastern Pacific Mixed Layer between 2004 and 2010: Spice Injection Mechanism. *Journal of Physical Oceanography*, 43(9), 1880-1898.
- Kosaka Y, and Xie S-P (2013). Recent global-warming hiatus tied to equatorial Pacific surface cooling. *Nature*, 501(7467), 403-407.
- Kosaka Y, and Xie S-P (2016). The tropical Pacific as a key pacemaker of the variable rates of global warming. *Nature Geoscience*, 9(9), 669-673.
- Kucharski F, Ikram F, Molteni F, Farneti R, Kang I-S, No H-H, King MP, Giuliani G, and Mogensen K (2016). Atlantic forcing of Pacific decadal variability. *Climate Dynamics*, 46(7), 2337-2351.
- Kucharski F, Kang I-S, Farneti R, and Feudale L (2011). Tropical Pacific response to 20th century Atlantic warming. *Geophysical Research Letters*, 38(3).
- Kug J-S, and Kang I-S (2006). Interactive Feedback between ENSO and the Indian Ocean. *Journal of Climate*, 19(9), 1784-1801.
- Kuntz LB, and Schrag DP (2018). Hemispheric asymmetry in the ventilated thermocline of the tropical Pacific. *Journal of Climate*, 31(3), 1281-1288.
- Kushnir Y (1994). Interdecadal Variations in North Atlantic Sea Surface Temperature and Associated Atmospheric Conditions. *Journal of Climate*, 7(1), 141-157.

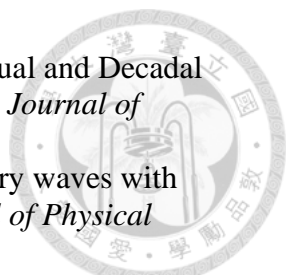
- 
- Kwon Y-O, Alexander MA, Bond NA, Frankignoul C, Nakamura H, Qiu B, and Thompson LA (2010). Role of the Gulf Stream and Kuroshio–Oyashio Systems in Large-Scale Atmosphere–Ocean Interaction: A Review. *Journal of Climate*, 23(12), 3249-3281.
- Lee T, Fukumori I, Menemenlis D, Xing Z, and Fu L-L (2002). Effects of the Indonesian throughflow on the Pacific and Indian oceans. *Journal of Physical Oceanography*, 32(5), 1404-1429.
- Lee T, and McPhaden MJ (2010). Increasing intensity of El Niño in the central-equatorial Pacific. *Geophysical Research Letters*, 37(14).
- Li X, Xie S-P, Gille ST, and Yoo C (2016). Atlantic-induced pan-tropical climate change over the past three decades. *Nature Climate Change*, 6(3), 275-279.
- Li YL, Wang F, and Sun Y (2012). Low-frequency spiciness variations in the tropical Pacific ocean observed during 2003-2012. *Geophysical Research Letters*, 39.
- Lin J, and Qian T (2019). A New Picture of the Global Impacts of El Niño-Southern Oscillation. *Scientific Reports*, 9(1), 17543.
- Liu C, Zhang W, Jin F-F, Stuecker MF, and Geng L (2022). Equatorial Origin of the Observed Tropical Pacific Quasi-Decadal Variability From ENSO Nonlinearity. *Geophysical Research Letters*, 49(10), e2022GL097903.
- Liu Y, San Liang X, and Weisberg RH (2007). Rectification of the Bias in the Wavelet Power Spectrum. *Journal of Atmospheric and Oceanic Technology*, 24(12), 2093-2102.
- Liu Z (1994). A simple model of the mass exchange between the subtropical and tropical ocean. *Journal of Physical Oceanography*, 24(6), 1153-1165.
- Liu Z (2012). Dynamics of Interdecadal Climate Variability: A Historical Perspective. *Journal of Climate*, 25(6), 1963-1995.
- Liu Z, and Alexander M (2007). Atmospheric bridge, oceanic tunnel, and global climatic teleconnections. *Reviews of Geophysics*, 45(2).
- Liu Z, and Di Lorenzo E (2018). Mechanisms and Predictability of Pacific Decadal Variability. *Current Climate Change Reports*, 4(2), 128-144.
- Liu Z, and Huang B (1998). Why is there a tritium maximum in the central equatorial Pacific thermocline? *Journal of Physical Oceanography*, 28(7), 1527-1533.
- Liu Z, Philander SGH, and Pacanowski RC (1994). A GCM study of tropical-subtropical upper-ocean water exchange. *Journal of Physical Oceanography*, 24(12), 2606-2623.
- Liu Z, and Shin S-I (1999). On thermocline ventilation of active and passive tracers. *Geophysical Research Letters*, 26(3), 357-360.
- Liu Z, Wu L, Gallimore R, and Jacob R (2002). Search for the origins of Pacific decadal climate variability. *Geophysical Research Letters*, 29(10), 42-41-42-44.
- Lou J, Holbrook NJ, and O’Kane TJ (2019). South Pacific Decadal Climate Variability and Potential Predictability. *Journal of Climate*, 32(18), 6051-6069.
- Lu P, and McCreary JP (1995). Influence of the ITCZ on the flow of thermocline water from the subtropical to the equatorial Pacific ocean. *Journal of Physical Oceanography*, 25(12), 3076-3088.
- Lu P, McCreary JP, and Klinger BA (1998). Meridional circulation cells and the source waters of the Pacific equatorial undercurrent. *Journal of Physical Oceanography*, 28(1), 62-84.

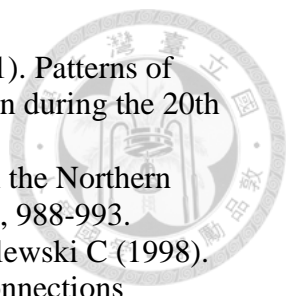
- 
- Lübbecke JF, Böning CW, and Biastoch A (2008). Variability in the subtropical-tropical cells and its effect on near-surface temperature of the equatorial Pacific: a model study. *Ocean Sci.*, 4(1), 73-88.
- Luo H, Zheng F, Keenlyside N, and Zhu J (2020). Ocean–atmosphere coupled Pacific Decadal variability simulated by a climate model. *Climate Dynamics*, 54(11), 4759-4773.
- Luo J-J, Masson S, Behera S, Delecluse P, Gualdi S, Navarra A, and Yamagata T (2003). South Pacific origin of the decadal ENSO-like variation as simulated by a coupled GCM. *Geophysical Research Letters*, 30(24).
- Luo J-J, Sasaki W, and Masumoto Y (2012). Indian Ocean warming modulates Pacific climate change. *Proceedings of the National Academy of Sciences*, 109(46), 18701-18706.
- Luo J-J, and Yamagata T (2001). Long-term El Niño-Southern Oscillation (ENSO)-like variation with special emphasis on the South Pacific. *Journal of Geophysical Research: Oceans*, 106(C10), 22211-22227.
- Luo Y, Rothstein LM, Zhang RH, and Busalacchi AJ (2005). On the connection between South Pacific subtropical spiciness anomalies and decadal equatorial variability in an ocean general circulation model. *Journal of Geophysical Research: Oceans*, 110(C10).
- Lyon B, Barnston AG, and DeWitt DG (2014). Tropical Pacific forcing of a 1998-1999 climate shift: observational analysis and climate model results for the boreal spring season. *Climate Dynamics*, 43(3), 893-909.
- Lysne J, Chang P, and Giese B (1997). Impact of the extratropical Pacific on equatorial variability. *Geophysical Research Letters*, 24(21), 2589-2592.
- Lyu K, Zhang X, Church JA, Hu J, and Yu J-Y (2017). Distinguishing the Quasi-Decadal and Multidecadal Sea Level and Climate Variations in the Pacific: Implications for the ENSO-Like Low-Frequency Variability. *Journal of Climate*, 30(13), 5097-5117.
- Mann ME, and Park J (1994). Global-scale modes of surface temperature variability on interannual to century timescales. *Journal of Geophysical Research: Atmospheres*, 99(D12), 25819-25833.
- Mann ME, and Park J (1999). Oscillatory Spatiotemporal Signal Detection in Climate Studies: A Multiple-Taper Spectral Domain Approach, in *Advances in Geophysics*, edited by R. Dmowska and B. Saltzman, pp. 1-131, Elsevier.
- Mantua NJ, Hare SR, Zhang Y, Wallace JM, and Francis RC (1997). A Pacific interdecadal climate oscillation with impacts on salmon production. *Bulletin of the American Meteorological Society*, 78(6), 1069-1080.
- McCreary JP, and Lu P (1994). Interaction between the subtropical and equatorial ocean circulations: The subtropical cell. *Journal of Physical Oceanography*, 24(2), 466-497.
- McDougall TJ, and Barker PM (2011). Getting started with TEOS-10 and the Gibbs Seawater (GSW) oceanographic toolbox. *Scor/lapso WG*, 127, 1-28.
- McDougall TJ, Barker PM, and Stanley GJ (2021). Spice variables and their use in physical oceanography. *Journal of Geophysical Research: Oceans*, 126(2), e2019JC015936.
- McDougall TJ, and Klocker A (2010). An approximate geostrophic streamfunction for use in density surfaces. *Ocean Modelling*, 32(3), 105-117.
- McDougall TJ, and Krzysik OA (2015). Spiciness. *Journal of Marine Research*, 73(5), 141-152.

- 
- McGregor S, Timmermann A, Stuecker MF, England MH, Merrifield M, Jin F-F, and Chikamoto Y (2014). Recent Walker circulation strengthening and Pacific cooling amplified by Atlantic warming. *Nature Climate Change*, 4(10), 888-892.
- McPhaden MJ (2012). A 21st century shift in the relationship between ENSO SST and warm water volume anomalies. *Geophysical Research Letters*, 39(9).
- McPhaden MJ, and Fine RA (1988). A dynamical interpretation of the tritium maximum in the central equatorial Pacific. *Journal of Physical Oceanography*, 18(10), 1454-1457.
- McPhaden MJ, Lee T, and McClurg D (2011). El Niño and its relationship to changing background conditions in the tropical Pacific Ocean. *Geophysical Research Letters*, 38(15).
- McPhaden MJ, and Zhang D (2002). Slowdown of the meridional overturning circulation in the upper Pacific Ocean. *Nature*, 415(6872), 603-608.
- McPhaden MJ, and Zhang D (2004). Pacific Ocean circulation rebounds. *Geophysical Research Letters*, 31(18).
- Meehl GA, and Hu A (2006). Megadroughts in the Indian Monsoon Region and Southwest North America and a Mechanism for Associated Multidecadal Pacific Sea Surface Temperature Anomalies. *Journal of Climate*, 19(9), 1605-1623.
- Meehl GA, Hu A, and Teng H (2016). Initialized decadal prediction for transition to positive phase of the Interdecadal Pacific Oscillation. *Nature Communications*, 7(1), 11718.
- Meehl GA, and Teng H (2007). Multi-model changes in El Niño teleconnections over North America in a future warmer climate. *Climate Dynamics*, 29(7), 779-790.
- Meehl GA, Teng H, Capotondi A, and Hu A (2021). The role of interannual ENSO events in decadal timescale transitions of the Interdecadal Pacific Oscillation. *Climate Dynamics*, 57(7), 1933-1951.
- Minobe S (1997). A 50–70 year climatic oscillation over the North Pacific and North America. *Geophysical Research Letters*, 24(6), 683-686.
- Moon B-K, Yeh S-W, Dewitte B, Jhun J-G, and Kang I-S (2007). Source of low frequency modulation of ENSO amplitude in a CGCM. *Climate Dynamics*, 29(1), 101-111.
- Müller P, and Willebrand J (1986). Compressibility effects in the thermohaline circulation: a manifestation of the temperature-salinity mode. *Deep Sea Research Part A. Oceanographic Research Papers*, 33(5), 559-571.
- Munk W (1981), Internal waves and small-scale processes, edited.
- Murata K, Kido S, and Tozuka T (2020). Role of Reemergence in the Central North Pacific Revealed by a Mixed Layer Heat Budget Analysis. *Geophysical Research Letters*, 47(13), e2020GL088194.
- Na H, Kim K-Y, Minobe S, and Sasaki YN (2018). Interannual to Decadal Variability of the Upper-Ocean Heat Content in the Western North Pacific and Its Relationship to Oceanic and Atmospheric Variability. *Journal of Climate*, 31(13), 5107-5125.
- Newman M, et al. (2016). The Pacific Decadal Oscillation, Revisited. *Journal of Climate*, 29(12), 4399-4427.
- Nie X, Gao S, Wang F, and Qu T (2016). Subduction of North Pacific tropical water and its equatorward pathways as shown by a simulated passive tracer. *Journal of Geophysical Research: Oceans*, 121(12), 8770-8786.

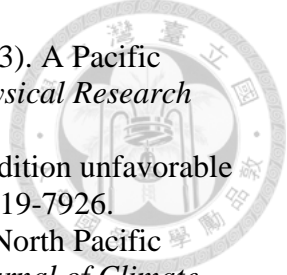
- 
- Nonaka M, and Sasaki H (2007). Formation mechanism for isopycnal temperature-salinity anomalies propagating from the eastern South Pacific to the equatorial region. *Journal of Climate*, 20(7), 1305-1315.
- Nonaka M, Xie S-P, and McCreary JP (2002). Decadal variations in the subtropical cells and equatorial Pacific SST. *Geophysical Research Letters*, 29(7), 2021-2024.
- O'Kane TJ, Matear RJ, Chamberlain MA, and Oke PR (2014). ENSO regimes and the late 1970's climate shift: The role of synoptic weather and South Pacific ocean spiciness. *J Comput Phys*, 271, 19-38.
- Ogata T, Xie S-P, Wittenberg A, and Sun D-Z (2013). Interdecadal Amplitude Modulation of El Niño–Southern Oscillation and Its Impact on Tropical Pacific Decadal Variability. *Journal of Climate*, 26(18), 7280-7297.
- Ohba M, and Ueda H (2007). An Impact of SST Anomalies in the Indian Ocean in Acceleration of the El Niño to La Niña Transition. *Journal of the Meteorological Society of Japan. Ser. II*, 85(3), 335-348.
- Okumura YM (2013). Origins of Tropical Pacific Decadal Variability: Role of Stochastic Atmospheric Forcing from the South Pacific. *Journal of Climate*, 26(24), 9791-9796.
- Okumura YM, DiNezio P, and Deser C (2017a). Evolving Impacts of Multiyear La Niña Events on Atmospheric Circulation and U.S. Drought. *Geophysical Research Letters*, 44(22), 6114-6116.
- Okumura YM, Sun T, and Wu X (2017b). Asymmetric Modulation of El Niño and La Niña and the Linkage to Tropical Pacific Decadal Variability. *Journal of Climate*, 30(12), 4705-4733.
- Oliver ECJ, et al. (2018). Longer and more frequent marine heatwaves over the past century. *Nature Communications*, 9(1), 1324.
- Pierce DW (2001). Distinguishing coupled ocean–atmosphere interactions from background noise in the North Pacific. *Progress in Oceanography*, 49(1), 331-352.
- Pierce DW, Barnett TP, and Latif M (2000). Connections between the Pacific ocean tropics and midlatitudes on decadal timescales. *Journal of Climate*, 13(6), 1173-1194.
- Power S, Casey T, Folland C, Colman A, and Mehta V (1999). Inter-decadal modulation of the impact of ENSO on Australia. *Climate Dynamics*, 15(5), 319-324.
- Power S, and Colman R (2006). Multi-year predictability in a coupled general circulation model. *Climate Dynamics*, 26(2), 247-272.
- Power S, et al. (2021). Decadal climate variability in the tropical Pacific: Characteristics, causes, predictability, and prospects. *Science*, 374(6563), eaay9165.
- Pozo Buil M, and Di Lorenzo E (2015). Decadal changes in Gulf of Alaska upwelling source waters. *Geophysical Research Letters*, 42(5), 1488-1495.
- Pu X, Chen Q, Zhong Q, Ding R, and Liu T (2019). Influence of the North Pacific Victoria mode on western North Pacific tropical cyclone genesis. *Climate Dynamics*, 52(1), 245-256.
- Qiu B (2003). Kuroshio Extension Variability and Forcing of the Pacific Decadal Oscillations: Responses and Potential Feedback. *Journal of Physical Oceanography*, 33(12), 2465-2482.
- Qiu B, Chen S, Schneider N, and Taguchi B (2014). A Coupled Decadal Prediction of the Dynamic State of the Kuroshio Extension System. *Journal of Climate*, 27(4), 1751-1764.

- 
- Qiu B, Schneider N, and Chen S (2007). Coupled Decadal Variability in the North Pacific: An Observationally Constrained Idealized Model. *Journal of Climate*, 20(14), 3602-3620.
- Rayner NA, Parker DE, Horton EB, Folland CK, Alexander LV, Rowell DP, Kent EC, and Kaplan A (2003). Global analyses of sea surface temperature, sea ice, and night marine air temperature since the late nineteenth century. *Journal of Geophysical Research: Atmospheres*, 108(D14).
- Rodgers KB, Cane MA, Naik NH, and Schrag DP (1999). The role of the Indonesian throughflow in equatorial Pacific thermocline ventilation. *Journal of Geophysical Research: Oceans*, 104(C9), 20551-20570.
- Rodgers KB, Friederichs P, and Latif M (2004). Tropical Pacific Decadal Variability and Its Relation to Decadal Modulations of ENSO. *Journal of Climate*, 17(19), 3761-3774.
- Rothstein LM, Zhang R-H, Busalacchi AJ, and Chen D (1998). A numerical simulation of the mean water pathways in the subtropical and tropical Pacific ocean. *Journal of Physical Oceanography*, 28(2), 322-343.
- Ruprich-Robert Y, Msadek R, Castruccio F, Yeager S, Delworth T, and Danabasoglu G (2017). Assessing the Climate Impacts of the Observed Atlantic Multidecadal Variability Using the GFDL CM2.1 and NCAR CESM1 Global Coupled Models. *Journal of Climate*, 30(8), 2785-2810.
- San S-C, and Tseng Y-h (2023). Aleutian low/PDO forces a decadal subsurface spiciness propagating mode in the North Pacific. *Climate Dynamics*.
- Sasaki YN, Schneider N, Maximenko N, and Lebedev K (2010). Observational evidence for propagation of decadal spiciness anomalies in the North Pacific. *Geophysical Research Letters*, 37.
- Schneider N (2000). A decadal spiciness mode in the tropics. *Geophysical Research Letters*, 27(2), 257-260.
- Schneider N (2004). The response of tropical climate to the equatorial emergence of spiciness anomalies. *Journal of Climate*, 17(5), 1083-1095.
- Schneider N, and Cornuelle BD (2005). The forcing of the Pacific Decadal Oscillation. *Journal of Climate*, 18(21), 4355-4373.
- Schneider N, Miller AJ, Alexander MA, and Deser C (1999a). Subduction of decadal North Pacific temperature anomalies: Observations and dynamics. *Journal of Physical Oceanography*, 29(5), 1056-1070.
- Schneider N, Venzke S, Miller AJ, Pierce DW, Barnett TP, Deser C, and Latif M (1999b). Pacific thermocline bridge revisited. *Geophysical Research Letters*, 26(9), 1329-1332.
- Schott FA, McCreary Jr. JP, and Johnson GC (2004). Shallow overturning circulations of the tropical-subtropical oceans, in *Earth's Climate*, edited, pp. 261-304.
- Shakun JD, and Shaman J (2009). Tropical origins of North and South Pacific decadal variability. *Geophysical Research Letters*, 36(19).
- Smale DA, et al. (2019). Marine heatwaves threaten global biodiversity and the provision of ecosystem services. *Nature Climate Change*, 9(4), 306-312.
- Smith R, Jones P, Briegleb B, Bryan F, Danabasoglu G, Dennis J, Dukowicz J, Eden C, Fox-Kemper B, and Gent P (2010). The parallel ocean program (POP) reference manual ocean component of the community climate system model (CCSM) and community earth system model (CESM). *LAUR-01853*, 141, 1-140.

- 
- Solomon A, McCreary JP, Kleeman R, and Klinger BA (2003). Interannual and Decadal Variability in an Intermediate Coupled Model of the Pacific Region. *Journal of Climate*, 16(3), 383-405.
- Stephens M, Liu Z, and Yang H (2001). Evolution of subduction planetary waves with application to North Pacific decadal thermocline variability. *Journal of Physical Oceanography*, 31(7), 1733-1746.
- Stevenson S, Fox-Kemper B, Jochum M, Neale R, Deser C, and Meehl G (2012). Will There Be a Significant Change to El Niño in the Twenty-First Century? *Journal of Climate*, 25(6), 2129-2145.
- Stommel H (1962). On the cause of the temperature-salinity curve in the ocean. *Proceedings of the National Academy of Sciences*, 48(5), 764-766.
- Stuecker MF (2018). Revisiting the Pacific Meridional Mode. *Scientific Reports*, 8.
- Suarez MJ, and Schopf PS (1988). A Delayed Action Oscillator for ENSO. *Journal of Atmospheric Sciences*, 45(21), 3283-3287.
- Sullivan A, Luo J-J, Hirst AC, Bi D, Cai W, and He J (2016). Robust contribution of decadal anomalies to the frequency of central-Pacific El Niño. *Scientific Reports*, 6(1), 38540.
- Sun C, Kucharski F, Li J, Jin F-F, Kang I-S, and Ding R (2017). Western tropical Pacific multidecadal variability forced by the Atlantic multidecadal oscillation. *Nature Communications*, 8(1), 15998.
- Sun F, and Yu J-Y (2009). A 10–15-Yr Modulation Cycle of ENSO Intensity. *Journal of Climate*, 22(7), 1718-1735.
- Sun T, and Okumura YM (2020). Impact of ENSO-Like Tropical Pacific Decadal Variability on the Relative Frequency of El Niño and La Niña Events. *Geophysical Research Letters*, 47(3), e2019GL085832.
- Taguchi B, Nakamura H, Nonaka M, Komori N, Kuwano-Yoshida A, Takaya K, and Goto A (2012). Seasonal Evolutions of Atmospheric Response to Decadal SST Anomalies in the North Pacific Subarctic Frontal Zone: Observations and a Coupled Model Simulation. *Journal of Climate*, 25(1), 111-139.
- Taguchi B, Xie S-P, Schneider N, Nonaka M, Sasaki H, and Sasai Y (2007). Decadal Variability of the Kuroshio Extension: Observations and an Eddy-Resolving Model Hindcast. *Journal of Climate*, 20(11), 2357-2377.
- Tailleux R (2016). Generalized Patched Potential Density and Thermodynamic Neutral Density: Two New Physically Based Quasi-Neutral Density Variables for Ocean Water Masses Analyses and Circulation Studies. *Journal of Physical Oceanography*, 46(12), 3571-3584.
- Tailleux R (2021). Spiciness theory revisited, with new views on neutral density, orthogonality, and passiveness. *Ocean Sci*, 17(1), 203-219.
- Tatebe H, Imada Y, Mori M, Kimoto M, and Hasumi H (2013). Control of decadal and bidecadal climate variability in the tropical Pacific by the off-equatorial South Pacific ocean. *Journal of Climate*, 26(17), 6524-6534.
- Timmermann A, et al. (2018). El Niño–Southern Oscillation complexity. *Nature*, 559(7715), 535-545.
- Torrence C, and Compo GP (1998). A Practical Guide to Wavelet Analysis. *Bulletin of the American Meteorological Society*, 79(1), 61-78.

- 
- Tourre YM, Rajagopalan B, Kushnir Y, Barlow M, and White WB (2001). Patterns of coherent decadal and interdecadal climate signals in the Pacific Basin during the 20th century. *Geophysical Research Letters*, 28(10), 2069-2072.
- Trenberth KE (1990). Recent Observed Interdecadal Climate Changes in the Northern Hemisphere. *Bulletin of the American Meteorological Society*, 71(7), 988-993.
- Trenberth KE, Branstator GW, Karoly D, Kumar A, Lau N-C, and Ropelewski C (1998). Progress during TOGA in understanding and modeling global teleconnections associated with tropical sea surface temperatures. *Journal of Geophysical Research: Oceans*, 103(C7), 14291-14324.
- Trenberth KE, and Hurrell JW (1994). Decadal atmosphere-ocean variations in the Pacific. *Climate Dynamics*, 9(6), 303-319.
- Vecchi GA, and Wittenberg AT (2010). El Niño and our future climate: where do we stand? *WIREs Climate Change*, 1(2), 260-270.
- Veronis G (1972). On properties of seawater defined by temperature, salinity, and pressure. *Journal of Marine Research*.
- Vimont DJ (2005). The Contribution of the Interannual ENSO Cycle to the Spatial Pattern of Decadal ENSO-Like Variability. *Journal of Climate*, 18(12), 2080-2092.
- Vimont DJ, Battisti DS, and Hirst AC (2001). Footprinting: A seasonal connection between the tropics and mid-latitudes. *Geophysical Research Letters*, 28(20), 3923-3926.
- Vimont DJ, Wallace JM, and Battisti DS (2003). The Seasonal Footprinting Mechanism in the Pacific: Implications for ENSO. *Journal of Climate*, 16(16), 2668-2675.
- Wade M, Caniaux G, and du Penhoat Y (2011). Variability of the mixed layer heat budget in the eastern equatorial Atlantic during 2005–2007 as inferred using Argo floats. *Journal of Geophysical Research: Oceans*, 116(C8).
- Wang S, Huang J, He Y, and Guan Y (2014). Combined effects of the Pacific Decadal Oscillation and El Niño–Southern Oscillation on Global Land Dry–Wet Changes. *Scientific Reports*, 4(1), 6651.
- Wang YY, and Luo YY (2020). Variability of spice injection in the upper ocean of the southeastern Pacific during 1992-2016. *Climate Dynamics*, 54(5-6), 3185-3200.
- Watanabe M, Shiogama H, Tatebe H, Hayashi M, Ishii M, and Kimoto M (2014). Contribution of natural decadal variability to global warming acceleration and hiatus. *Nature Climate Change*, 4(10), 893-897.
- Wen T, Chen Q, Li J, Ding R, Tseng Y-h, Hou Z, and Li X (2020). Influence of the North Pacific Victoria Mode on the Madden–Julian Oscillation. *Frontiers in Earth Science*, 8.
- White WB, Tourre YM, Barlow M, and Dettinger M (2003). A delayed action oscillator shared by biennial, interannual, and decadal signals in the Pacific Basin. *Journal of Geophysical Research: Oceans*, 108(C3).
- Wu L, Liu Z, Gallimore R, Jacob R, Lee D, and Zhong Y (2003). Pacific Decadal Variability: The Tropical Pacific Mode and the North Pacific Mode. *Journal of Climate*, 16(8), 1101-1120.
- Xu M, Xu H, Ma J, and Deng J (2022). Impact of Pacific Decadal Oscillation on interannual relationship between El Niño and South China Sea summer monsoon onset. *International Journal of Climatology*, 42(5), 2739-2753.
- Yang H, Jiang H, and Tan B (2005). Asymmetric impact of the North and South Pacific on the equator in a coupled climate model. *Geophysical Research Letters*, 32(5).

- 
- Yeager SG, and Large WG (2004). Late-winter generation of spiciness on subducted isopycnals. *Journal of Physical Oceanography*, 34(7), 1528-1547.
- Yeh S-W, and Kirtman BP (2004). Tropical Pacific decadal variability and ENSO amplitude modulation in a CGCM. *Journal of Geophysical Research: Oceans*, 109(C11).
- Yu J-Y, and Kim ST (2011). Relationships between extratropical sea level pressure variations and the central Pacific and eastern Pacific types of ENSO. *Journal of Climate*, 24(3), 708-720.
- Zeller M (2020). The Impact of Subtropical to Tropical Oceanic Interactions on Tropical Pacific Decadal Variability, Monash University.
- Zeller M, McGregor S, van Sebille E, Capotondi A, and Spence P (2021). Subtropical-tropical pathways of spiciness anomalies and their impact on equatorial Pacific temperature. *Climate Dynamics*, 56(3), 1131-1144.
- Zhang D, and McPhaden MJ (2006). Decadal variability of the shallow Pacific meridional overturning circulation: Relation to tropical sea surface temperatures in observations and climate change models. *Ocean Modelling*, 15(3), 250-273.
- Zhang G, Zeng G, Li C, and Yang X (2020). Impact of PDO and AMO on interdecadal variability in extreme high temperatures in North China over the most recent 40-year period. *Climate Dynamics*, 54(5), 3003-3020.
- Zhang H, Clement A, and Di Nezio P (2014). The South Pacific Meridional Mode: A Mechanism for ENSO-like Variability. *Journal of Climate*, 27(2), 769-783.
- Zhang R-H, and Rothstein LM (2000). Role of off-equatorial subsurface anomalies in initiating the 1991–1992 El Niño as revealed by the National Centers for Environmental Prediction ocean reanalysis data. *Journal of Geophysical Research: Oceans*, 105(C3), 6327-6339.
- Zhang R-H, Rothstein LM, Busalacchi AJ, and Liang X-Z (1999). The onset of the 1991–92 El Niño event in the tropical Pacific Ocean: The NECC subsurface pathway. *Geophysical Research Letters*, 26(7), 847-850.
- Zhang W, Jin F-F, Stuecker MF, Wittenberg AT, Timmermann A, Ren H-L, Kug J-S, Cai W, and Cane M (2016). Unraveling El Niño's impact on the East Asian Monsoon and Yangtze River summer flooding. *Geophysical Research Letters*, 43(21), 11,375-311,382.
- Zhang Y, Wallace JM, and Battisti DS (1997). ENSO-like Interdecadal Variability: 1900–93. *Journal of Climate*, 10(5), 1004-1020.
- Zhang Y, Yu S-Y, Amaya DJ, Kosaka Y, Stuecker MF, Yang J-C, Lin X, and Fan L (2022). Atmospheric Forcing of the Pacific Meridional Mode: Tropical Pacific-Driven Versus Internal Variability. *Geophysical Research Letters*, 49(7), e2022GL098148.
- Zhang Y, et al. (2021). Pacific Meridional Modes without Equatorial Pacific Influence. *Journal of Climate*, 34(13), 5285-5301.
- Zhao M, Hendon HH, Alves O, Liu G, and Wang G (2016). Weakened Eastern Pacific El Niño Predictability in the Early Twenty-First Century. *Journal of Climate*, 29(18), 6805-6822.
- Zhao Y, and Di Lorenzo E (2020). The impacts of Extra-tropical ENSO Precursors on Tropical Pacific Decadal-scale Variability. *Scientific Reports*, 10(1), 3031.

- 
- Zhao Y, Di Lorenzo E, Newman M, Capotondi A, and Stevenson S (2023). A Pacific Tropical Decadal Variability Challenge for Climate Models. *Geophysical Research Letters*, 50(15), e2023GL104037.
- Zhong W, Zheng X-T, and Cai W (2017). A decadal tropical Pacific condition unfavorable to central Pacific El Niño. *Geophysical Research Letters*, 44(15), 7919-7926.
- Zou Q, Ding R, Li J, Tseng Y-h, Hou Z, Wen T, and Ji K (2020). Is the North Pacific Victoria Mode a Predictor of Winter Rainfall over South China? *Journal of Climate*, 33(20), 8833-8847.